ISSN 2954-436X

Geofísica Internacional

Revista Trimestral Publicada por el Instituto de Geofísica de la Universidad Nacional Autónoma de México

México
Volume 62 Number 2
April - June

— Geofísica Internacional —

GEOFÍSICA INTERNACIONAL, Año 52, Vol. 52, Núm. 2, abril - junio de 2023 es una publicación trimestral, editada por la Universidad Nacional Autónoma de México, Ciudad Universitaria, Alcaldía Coyoacán, C.P. 04150, Ciudad de México, a través del Instituto de Geofísica, Circuito de la Investigación Científica s/n, Ciudad Universitaria, Alcaldía Coyoacán, C.P. 04150, Ciudad de México, Tel. (55)56 22 41 15. URL: http://revistagi.geofisica.unam.mx, correo electrónico: revistagi@igeofisica.unam.mx. Editora responsable: Andrea Rostan Robledo. Certificado de Reserva de Derechos al uso Exclusivo del Título: 04-2022-081610251200-102, ISSN: en trámite, otorgados por el Instituto Nacional del Derecho de Autor (INDAUTOR). Responsable de la última actualización Saúl Armendáriz Sánchez, Editor Técnico. Fecha de la última modificación: 31 de diciembre 2011, Circuito de la Investigación Científica s/n, Ciudad Universitaria, Alcaldía Coyoacán, C.P. 04150, Ciudad de México.

https://doi.org/10.22201/igeof.2954436xe.2023.62.2

Geofísica Internacional
Vol. 62, Núm. 2, abril-junio de 2023

Contents

Geofísica Internacional (2023) **62-2**: 445 - 465

A Seismological Study of the Michoacán-Colima, Mexico, Earthquake of 19 September 2022 (M_w7.6)

S. K. Singh[1], A. Iglesias[1*], D. Arroyo[2], X. Pérez-Campos[1, 8], M. Ordaz[3], C. Mendoza[4], R. D. Corona-Fernández[5], L. Rivera[6], V. H. Espíndola[1], D. González-Ávila[1], R. Martínez-López[1], O. Castro-Artola[7], M. A. Santoyo[1], and S. I. Franco[1]

Resumen

El sismo de Michoacán-Colima el 19 de septiembre de 2022 (M_s7.6, M_w7.6) rompió el límite NW de la interface entre las placas de Cocos y norteamericana, causando daño severo a muchas poblados y ciudades en los estados de Michoacán y Colima. El daño fue además agravado por una réplica de magnitud importante (M_w6.7) el 22 de septiembre. El sismo principal inició debajo de la costa a una distancia hipocentral de 22 km de la estación sísmica de Maruata (MMIG) donde las aceleraciones y velocidades máximas registradas, *PGA* y *PGV*, fueron de 1g y 28 cm/s, respectivamente. El epicentro de la réplica más grande se localizó a ~30 km al SE del sismo principal. El modelado de falla finita del sismo principal presentado por el Servicio Geológico de los Estados Unidos (USGS), revela una propagación de la ruptura a lo largo del rumbo de la falla hacia la dirección NW con una caída de esfuerzos estáticos $\Delta\sigma_s$, of 3.7 MPa. Nuestra estimación de energía radiada, E_R, es 3.44×10^{15}J, de tal manera que E_R/M_0 es de 1.27×10^{-5} valor similar al calculado para otros grandes sismos de subducción cuyas área de ruptura no se extienden hacia la trinchera.

El área que contiene las réplicas del sismo principal de 2022 se traslapa con el área de réplicas del sismo del 30 de enero de 1973 (M_w7.6). Los sismográmas Galitzin de los dos sismos registrados en la estación DeBilt (DBN) localizada en los Países Bajos son razonablemente similares de tal manera que pueden ser clasificados como eventos *quasi*-repetidos. Por otro lado, el sismograma DBN del sismo del 15 de abril de 1941 (M_S 7.7), cuya localización no se conoce bien del todo, aunque se sabe que ocurre en la misma región, difiere sustancialmente de los sismogramas de 1972 y 2022, sugiriendo que el primero rompió un área diferente de la del sismo de 1941.

Un análisis extensivo de registros regionales exhibe el efecto de directividad observada en los datos de movimientos fuertes y en los cocientes de aceleraciones del sismo principal y de las aceleraciones de la réplica mayor. La directividad explica la dependencia azimutal observada en los cocientes de *PGA* y *PGV*, los cocientes espectrales, la distribución de *PGA* y la respuesta espectral a 2s *Sa* ($T = 2\,s$). Debido a la directividad, los valores de *PGA*, *PGV* y *Sa* ($T = 2\,s$) en el Valle de México durante el sismo principal y la réplica mayor fueron muy similares a pesar de la diferencia en magnitud de 0.9. En CU (el sitio de roca firme de referencia en la Ciudad de México), *PGA* y *PGV* durante ambos eventos fueron de ~ 6 cm/s^2 and 2 cm/s, respectivamente, valores más bajos que los esperados para el sismo principal y más altos que los esperados para la réplica mayor.

Palabras Clave: Sismo de Michoacán-Colima. Sismos *Quasi*-repetidos. Directividad.

Abstract

Michoacán-Colima earthquake of 19 September 2022 (M_s 7.6, M_w7.6) ruptured the NW end of the Cocos-North American plate interface, causing severe damage to many towns and cities in the states of Michoacán and Colima. The damage was further exacerbated by a major aftershock (M_w6.7) on 22

Keywords: Michoacán-Colima Earthquake. *Quasi*-repeated events. Directivity.

Received: December 16, 2022; Accepted: February 3, 2023; Published on-line: April 1, 2023.

Editorial responsibility: Anonymous

* Corresponding author: Arturo Iglesias
[1] Instituto de Geofísica, Universidad Nacional Autónoma de México, Mexico City, Mexico
[2] Departamento de Materiales, Universidad Autónoma Metropolitana, Mexico City, Mexico
[3] Instituto de Ingeniería, Universidad Nacional Autónoma de México, Mexico City, Mexico
[4] Centro de Geociencias, Universidad Nacional Autónoma de México, Juriquilla, Mexico
[5] Posgrado en Ciencias de la Tierra, Universidad Nacional Autónoma de México, Mexico City, México.
[6] Institut Terre & Environnement Strasbourg (ITES) CNRS/Université de Strasbourg, Strasbourg, France.
[7] Instituto de Investigación en Gestión de Riesgos y Cambio Climático, Universidad de Ciencias y Artes de Chiapas, Tuxtla Gutiérrez, Mexico.
[8] Seismological Laboratory, California Institute of Technology, Pasadena, California, United States of America.

https://doi.org/10.22201/igeof.2954436xe.2023.62.2.1453

September. The mainshock initiated below the coast at a hypocentral distance of 22 km from the seismic station of Maruata (MMIG) where peak ground acceleration and velocity, *PGA* and *PGV*, of ~ 1 g and 28 cm/s were recorded. The epicenter of the major aftershock was located ~ 30 km SE of the mainshock. Finite fault modeling of the mainshock by the U.S. Geological Survey reveals a rupture propagation along the strike towards the NW and yields a static stress drop, $\Delta\sigma_s$, of 3.7 MPa. Our estimated radiated energy, E_R, is 3.44×10^{15} J, so that E_R/M_0 is 1.27×10^{-5} similar to other large Mexican thrust earthquakes whose rupture areas do not extend to the trench.

Aftershocks of the 2022 mainshock overlap that of the Colima earthquake of 30 January 1973 (M_w 7.6). Galitzin seismograms of the two earthquakes at DeBilt (DBN), The Netherlands, are reasonably similar so that they may be classified as quasi-repeated events. On the other hand, the DBN seismogram of the earthquake of 15 April 1941 (M_S 7.7), whose location is poorly known but occurred in the same region, differs greatly from those of the 1973 and 2022 earthquakes, suggesting a different source area for the 1941 event.

An analysis of the extensive regional recordings exhibits the effect of the directivity on the ground motion and on the ratio of ground motion during the mainshock to the major aftershock. The directivity explains the observed azimuthal dependence of *PGA* and *PGV* ratios, spectral ratios, and *PGA* and response spectra at 2s, *Sa* ($T = 2s$). Because of the directivity, *PGA*, *PGV*, and *Sa* ($T = 2s$) in the Valley of Mexico during the mainshock and the major aftershock were about the same in spite of the magnitude difference of 0.9. At CU (the reference, hard site in Mexico City), *PGA* and *PGV* during both events were ~ 6 cm/s^2 and 2 cm/s, respectively, lower than expected for the mainshock and higher than expected for the aftershock.

Introduction

In the current public perception, 19 September is the date when large, destructive earthquakes occur in Mexico. The Michoacán earthquake of 1985 (M_w 8.0), which caused unprecedented deaths and damage in Mexico City, occurred on this date. The Puebla-Morelos earthquake of 2017 (M_w 7.1), which may have been the deadliest intraslab event in the history of Mexico City, also occurred on the same date. So, when on 19 September 2022 a subduction thrust earthquake (M_w 7.6) broke the Cocos-North American plate interface along the coast of Michoacán-Colima, there was general consternation and disbelief. The earthquake caused severe damage to many towns and cities in the states of Michoacán and Colima (EERI Preliminary Virtual Reconnaissance Report, 2022). The largest aftershock (M_w 6.7) that occurred on 22 September caused further damage and panic. Both of these events were felt strongly in the lake-bed zone of Mexico City, about 450 km away. The Mexican Seismic Alert System (SASMEX) performed well; the lead time for the arrival of strong motion in Mexico City was about 2 minutes (**https://www.youtube.com/watch?v=NCjVeiIZADw).**

The tectonic setting of the area of where the 2022 earthquake occurred is shown in Figure 1. In the region, the oceanic Rivera (RIVE) and Cocos (COCOS) plates subduct below Mexico which forms part of the North American (NOAM) plate. The boundary between the RIVE and COCOS plates, as well as the relative convergence speed between the two plates, are controversial. Bandy *et al.* (1995) suggest that the subducted RIVE-COCOS boundary lies directly beneath the southern Colima Rift (SCR) and is parallel to it (Figure 1). The SCR extends from the city of Colima to the Middle America Trench and forms a part of the Colima rift. COCOS-NOAM relative convergence rate at 17.9°N, 104.0°W is ~ 6.0 cm/yr in the direction 32.3ºN (DeMets *et al.*, 2010).

Subduction of RIVE and COCOS plates below NOAM gives rise to large, shallow thrust earthquakes. Large earthquakes that have occurred in the region since 1910 are listed in Table 1. The aftershock areas of the events, if known, are shown in Figure 1. The locations of the 2022 mainshock and its largest M_w 6.7 aftershock are also given in the figure. We note that the epicenter of the mainshock falls within the aftershock area of the 1973 earthquake (M_w 7.6) outlined by Reyes *et al.* (1979) based on seismograms recorded on a portable network deployed in the field.

The three largest subduction thrust earthquakes in Mexico since 1900 have occurred along the Michoacán-Colima-Jalisco segment of the Mexican subduction zone. The earthquakes of 3 June 1932 (M_s 8.2) and 9 October 1995 (M_w 8.0) ruptured the RIVE-NOAM plate interface, whereas the 19 September 1985 (M_w 8.0) event broke the COCOS-NOAM interface. The earthquakes listed in Table 1 caused damage to towns and cities in the vicinity of their rupture areas but two of them were also destructive to Mexico City. The earthquake of 7 June 1911 (M_s 7.7) destroyed the town of Ciudad Guzmán in the state of Jalisco. It also caused considerable damage in Mexico City (Miranda y Marron, 1911-1912). As mentioned earlier, the 1985 Michoacán earthquake caused unprecedented damage and deaths in Mexico City.

In this paper, we present a source study of the 2022 earthquake and its major M_w 6.7 aftershock in the context of previous large earthquakes in the vicinity, and discuss the characteristics of the ground motion at regional distances.

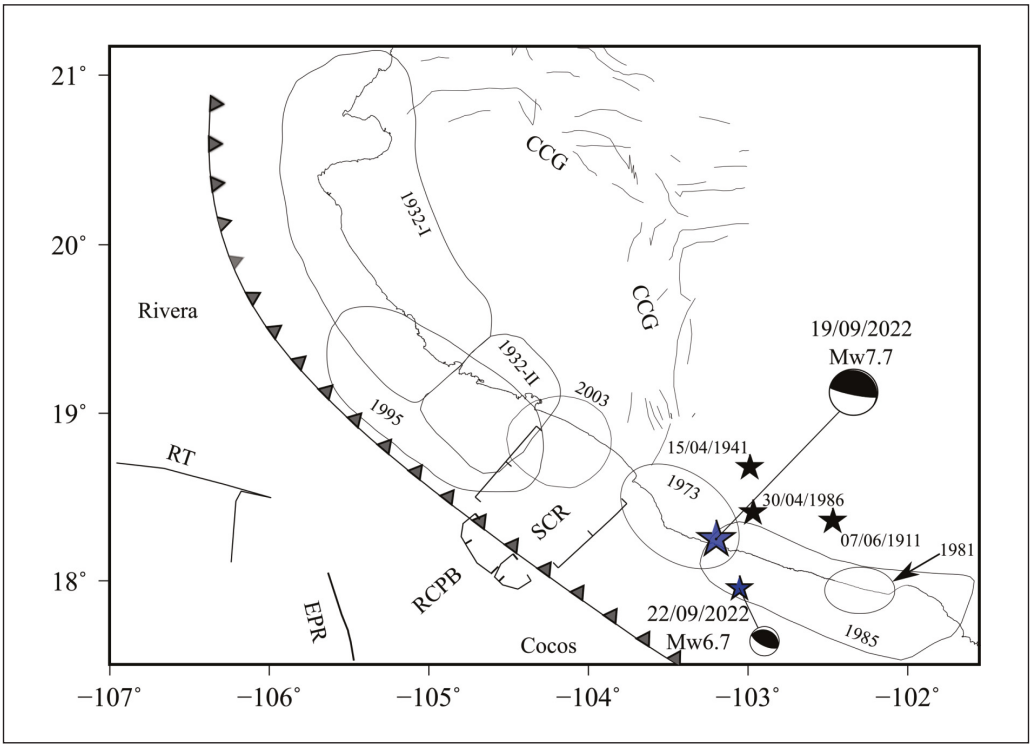

Figure 1. Tectonic map of the region (modified from Bandy *et al.*, 1995; Singh *et al.*, 2003). RT: Rivera Transform, EPR: East Pacific Rise, RCPB: Rivera Cocos Plate Boundary, SCR: Southern Colima Rift, CCG: Colima Central Graben. Ticked lines indicate areal extent of SCR rift. The contours outline aftershock areas of large and great earthquakes. Black stars depict epicenters of the earthquakes whose aftershock areas are not known. Blue stars with focal mechanism: 2022 mainshock (M_w 7.6) and the major aftershock (M_w 6.7). Note that the mainshock epicenter falls in the elliptical aftershock area of the 1973 earthquake.

Table 1. Large subduction thrust earthquakes since 1910 in the region of interest

No.	Date	Lat^{0}N	Long^{0}W	Magnitude
1	7 June 1911	18.36	102.47	7.7(M_s)
2	3 June 1932	19.80	103.93	8.2(M_s), 7.9(M_w)
3	18 June 1932	19.09	103.55	7.8(M_s), 7.8(M_w)
4	15 April 1941	18.68	102.99	7.8(M_s)
5	30 January 1973	18.49	102.89	7.5(M_s), 7.6(M_w)
6	25 October 1981	17.75	102.25	7.3(M_s), 7.2(M_w)
7	19 September 1985	18.14	102.71	8.1(M_s), 8.0(M_w)
8	30 April 1986	18.41	102.97	7.0(M_s), 6.9(M_w)
9	9 October 1995	18.85	104.50	7.3(M_s), 8.0(M_w)
10	22 January 2003	18.60	104.22	7.6(M_s), 7.5(M_w)
11	19 September 2022	18.22	103.33	7.6(M_s), 7.6(M_w)

References and notes keyed to event number in Table 1

1. Location from ISC-GEM catalog; Ms from Abe (1981)
2. Location from ISC-GEM catalog; aftershock area from Singh *et al.* (1985); M_s from Abe (1981); M_w from Wang *et al.* (1982)
3. Location from ISC-GEM catalog; aftershock area from Singh *et al.* (1985); M_s from Abe (1981); M_w from Wang *et al.* (1982)
4. Location from ISC-GEM catalog; M_s from Abe (1981). Location given by Kelleher *et al.* (1973) is: 18.85^{0}N, 102.94^{0}W
5. Location from ISC-GEM catalog; aftershock area, Ms and M_w from Reyes *et al.* (1979)
6. Location and aftershock area from Havskov *et al.* (1983); M_s and M_w from Global CMT catalog
7. Location and aftershock area from UNAM Seismology Group (1986); M_s and M_w from Global CMT catalog
8. Location from ISC-GEM catalog; M_s and M_w from Global CMT catalog
9. Location and aftershock area from Pacheco *et al.* (1997); M_s and M_w from Global CMT catalog
10. Location and aftershock area from Singh *et al.* (2003); M_s and M_w from Global CMT catalog
11. Location and M_w from this study; M_s from Global CMT catalog

Our analysis is based on local and regional data as well as teleseismic *P*-wave data. We also discuss the probability of having observed three major earthquakes on the same day.

Epicentral recording

Maruata station (MMIG), located on the coast of Michoacán and nearly above the hypocenter [(*S*-*P*) time 2.8 s], is equipped with a broadband seismograph, an accelerograph, and a GPS receiver. The broadband seismograms were saturated on the *S*-wave arrival. The acceleration traces were integrated to obtain velocity and displacement. Because of the baseline shift in the acceleration, the velocity often does not approach the expected zero level at the end of the recording; instead records often show a residual velocity. Integration of these velocity recordings without a shift correction leads to unrealistic displacements. To correct the shift, we selected a time, T_1, after the end of the intense part of motion and fit, in the least-square sense, a straight line to the velocity data between T_1 and the end of the record. The line at T_1 is then connected to time T_0 which we choose at the *P*-wave arrival. These two-line segments are used to correct the velocity record, which are then integrated to obtain the displacement (see, Singh *et al.*, 2020 for more details). We followed this procedure in the integration. The traces are shown in Figure 2. The *PGA* and *PGV* on the NS component are 1090 gal and 28.3 cm/s, respectively.

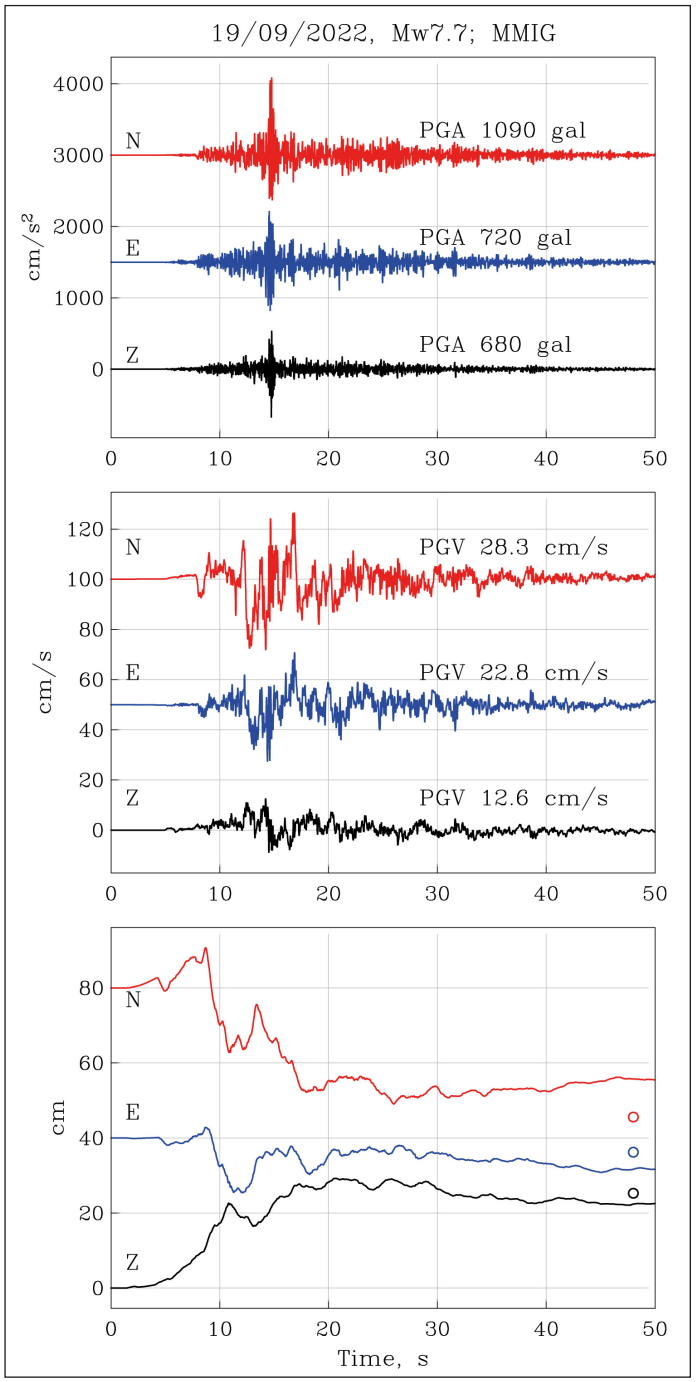

Figure 2. Acceleration, velocity, and displacement at the epicentral station of Maruata (MMIG) during the mainshock. Circles in the bottom frame show coseismic static displacement retrieved from GPS station TNMR collocated with MMIG (Z: +25.3 cm; EW: -3.8 cm; NS: -34.4 cm)

The GPS receiver at MMIG had stopped working 20 days before the mainshock due to a problem with the solar panel. The station was reestablished 4 days after the event. Successive measurements show post-seismic creep. Correcting for the lost time series before the 2022 earthquake by extrapolation and for the post-seismic creep, the estimated coseismic static NS, EW, and vertical, Z displacements from GPS are -34.4 cm, -3.8 cm, and +25.3 cm, respectively. These values are marked in the bottom frame of Figure 2, which shows the displacement seismograms. Not surprisingly, the static displacement from GPS differs from that estimated from integration. The MMIG traces are reminiscent of the epicentral recording at Caleta de Campo (CALE) during the 19 September 1985, Michoacán earthquake (M_w 8.0) (Anderson *et al.*, 1986) with some differences: *PGA* at CALE during the 1985 earthquake was much smaller (141 cm/s^2; NS and EW), *PGV* was about the same (24.7 cm/s; NS), and PGD was greater (78 cm; NS).

Basic source parameters of the mainshock and the major aftershock

Since 2014, the Servicio Sismológico Nacional (SSN, Mexican National Seismological Service) routinely calculates and publishes M_w through *W*-phase inversion (Kanamori and Rivera, 2008) using an algorithm modified by Hayes *et al.* (2011) and revised by Duputel *et al.* (2012). For $M \geq$ 5.2 earthquakes, the algorithm automatically gets triggered 10 minutes after the origin time and uses broadband data of the SSN stations (Pérez-Campos *et al.*, 2019). It starts with the preliminary, automatically obtained, SSN location and magnitude, and looks for the best half duration and then the best location. For the 19 September 2022 mainshock and its major aftershock of 22 September we revised the routine

near-realtime *W*-phase solution by checking and, if required, updating the response files and eliminating data with obvious problems. The revised solutions of the mainshock and the major aftershock are listed in Tables 2 and 3, respectively. The tables also give the source parameters reported by the United States Geological Survey (USGS) and the Global Centroid Moment Tensor (GCMT) project.

There are some differences in the focal mechanism and seismic moment (M_0) given by the three sources. For example, M_0 of the mainshock estimated in this study and by the USGS are nearly the same, 2.7x10^{20} N-m (M_w 7.55) but the value listed in the GCMT catalog is 1.7 times greater. Henceforth, we shall take M_0 of the mainshock and the major aftershock as 2.7×10^{20} N-m (M_w 7.6) and 1.6×10^{19} N-m (M_w 6.7), respectively. We note that, with respect to the SSN epicenter, the USGS epicenter is shifted by 44 km towards N53°E for the mainshock and 29 km towards N36°E for the aftershock. A consistent NE shift of the epicenters of Mex-

Table 2. Source parameters of the 19 September 2022, Michoacán-Colima earthquake

Timing	Lat °N	Long °W	Depth, km	Strike °	Dip,°	Rake °	M_0, Nm
SSN 18:05:09.0	18.220	103.290	15.0*	-	-	-	-
SSN W-phase CMT+ 18:05:29.0	18.420	103.395	15.5	293	18	83	2.71×10^{20} (M_w7.56)
USGS 18:05:08	18.455	102.956	26.9	-	-	-	-
USGS, W-phase CMT	18.267	103.185	23.5	287	18	86	2.67×10^{20} (M_w 7.55)
Global CMT 18:05:29.5	18.590	103.430	16.9	306	11	107	4.49×10^{20} (M_w 7.70)

*Depth fixed.

+ Based on an algorithm implemented at Institute of Geophysics, UNAM, which uses regional waveforms recorded on SSN broadband stations. A grid search was performed for the depth and the centroid location.

Table 3. Source parameters of the major aftershock of 22 September 2022

Timing	Lat °N	Long °W	Depth, km	ϕ	δ	λ	M_0, Nm
SSN 06:16:07.0	18.050	103.120	12.0*	-	-	-	-
SSN *W*-phase CMT+ 06:16:13.0	18.050	103.120	11.5	293	17	86	1.56×10^{19} (M_w 6.73)
USGS/NEICx	18.263	102.955	20.0	-	-	-	-
06:16:09.0							
USGS/NEIC, *W*-phase CMTx 06:16:15.6	17.821	102.978	19.5	297	17	105	1.90×10^{19} (M_w 6.79)
Global CMTX 06:16:16.2	18.270	103.080	24.0	289	25	83	1.50×10^{19} (M_w 6.72)

*Depth fixed.

+ A grid search was performed for the depth and the centroid location.

x Global CMT and USGS/NEIC source parameters last accessed on 06/12/2022.

ican subduction zone earthquakes reported by international agencies has been documented earlier (Singh and Lermo, 1985; Hjörleifsdóttir *et al.*, 2016).

Aftershock distribution

Aftershocks that occurred in the first 30 days (805 events with coda-wave magnitude Mc ≥ 3.5) are shown in Figure 3. We determined CMT solutions of seven significant aftershocks in addition to the major aftershock (Table 4). Focal mechanisms of the mainshock and the eight aftershocks (thrust: five; normal: two; strike slip: one) are displayed in Figure 3.

Several features of the aftershocks are worth noting in Figure 3. They overlap the elliptical 1973 aftershock area outlined by Reyes *et al.* (1979). Relatively few aftershocks occurred within the large coseismic slip area of the 2022 earthquake (see next section). Relative lack of aftershocks over the areas of large slip has been reported for many earthquakes (see Das and Henry, 2003 for a review). Most

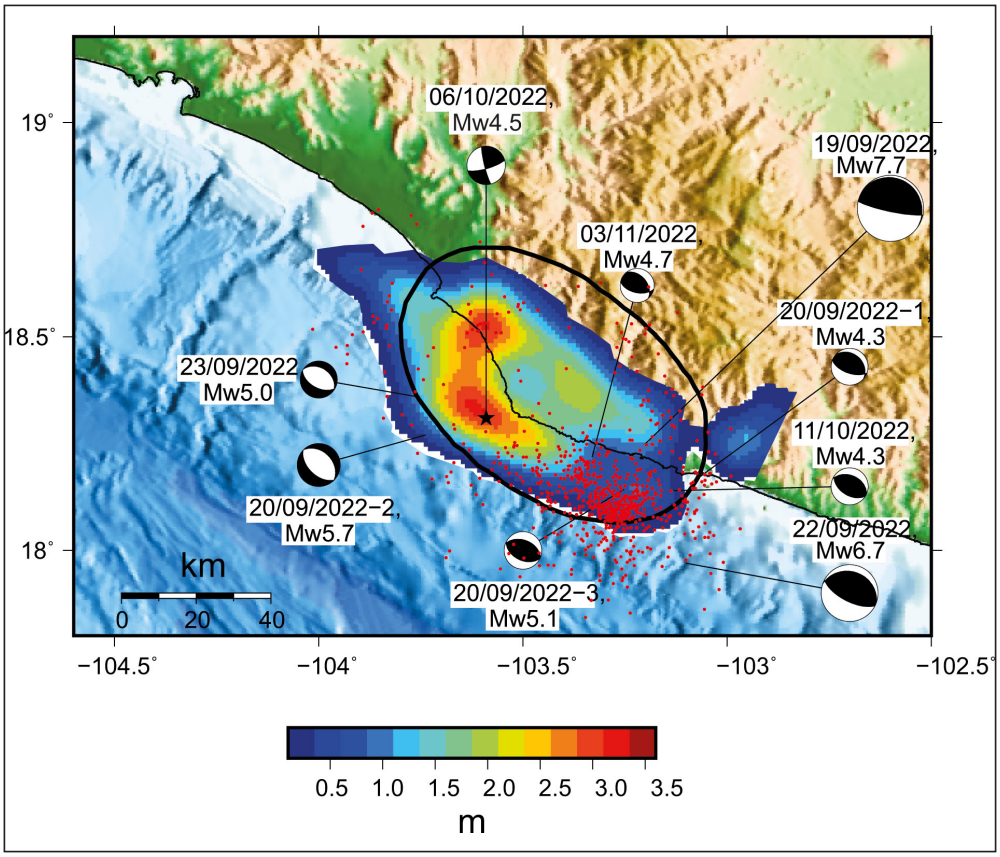

Figure 3. Coseismic slip distribution for the mainshock, taken from the U.S. Geological Survey finite fault model (**https://earthquake.usgs.gov/earthquakes/eventpage/us7000i9bw/finite-fault).** Epicenters and focal mechanisms of the mainshock and significant aftershocks are shown in the Figure. Red dots: relocated aftershocks which occurred in first 30 days. Ellipse: aftershock area of the 1973 Colima earthquake (Reyes *et al.*, 1979). Aftershocks overlap the elliptical area. Note the concentration of the aftershocks to the SW of the epicenter.

Table 4. Source parameters of seven additional, significant aftershocks

Date, Time	Lat.	Lon.	M_0, N-m	M_w	ϕ	δ	λ
20/09/2022-1, 06:19:08	18.30	-103.04	3.36×10^{15}	4.3	311	30	108
20/09/2022-2, 08:17:13	18.27	-103.74	4.30×10^{17}	5.7	315	38	-90
20/09/2022-3, 19:04:29	18.14	-103.25	4.54×10^{16}	5.1	291	44	86
23/09/2022, 18:25:56	18.36	-103.76	3.69×10^{16}	5.0	304	37	-86
06/10/2022, 07:03:42	18.31	-103.59	6.82×10^{15}	4.5	166	83	14
11/10/2022, 09:43:31	18.14	-103.13	3.74×10^{15}	4.3	294	40	83
03/11/2022, 07:44:51	18.31	-103.28	9.89×10^{15}	4.6	319	43	117

of the aftershocks of the 2022 earthquakes were concentrated to the south of the mainshock epicenter and in the SE part of the 1973 aftershock area. A similar concentration was observed in the aftershock distribution in 1973 which led Reyes *et al.* (1979) to suggest that the rupture initiated to the SE and propagated to the NW.

Finite fault model of the mainshock and the major aftershock

We determined slip models for the earthquakes of 19 and 22 September 2022 using the rapid finite-fault inversion methodology described by Mendoza and Martínez-Lopez (2022). The method automatically assigns fault parameters based on the earthquake size and derives a coseismic slip model using teleseismic P waveforms obtained in near-realtime from the Incorporated Research Institutes for Seismology Data Management Center (**https://ds.iris.edu/).**

For the 19 September M_w 7.6 earthquake, we used the hypocenter and moment-tensor source mechanism reported by the USGS following the event (Table 2; earthquake.usgs.gov/earthquakes/search/). The slip model for the shallow, northeast-dipping plane shows two separate zones of high slip: one downdip of the hypocenter with a peak slip of 1 m and a second zone about 40 km to the northwest with a maxi-

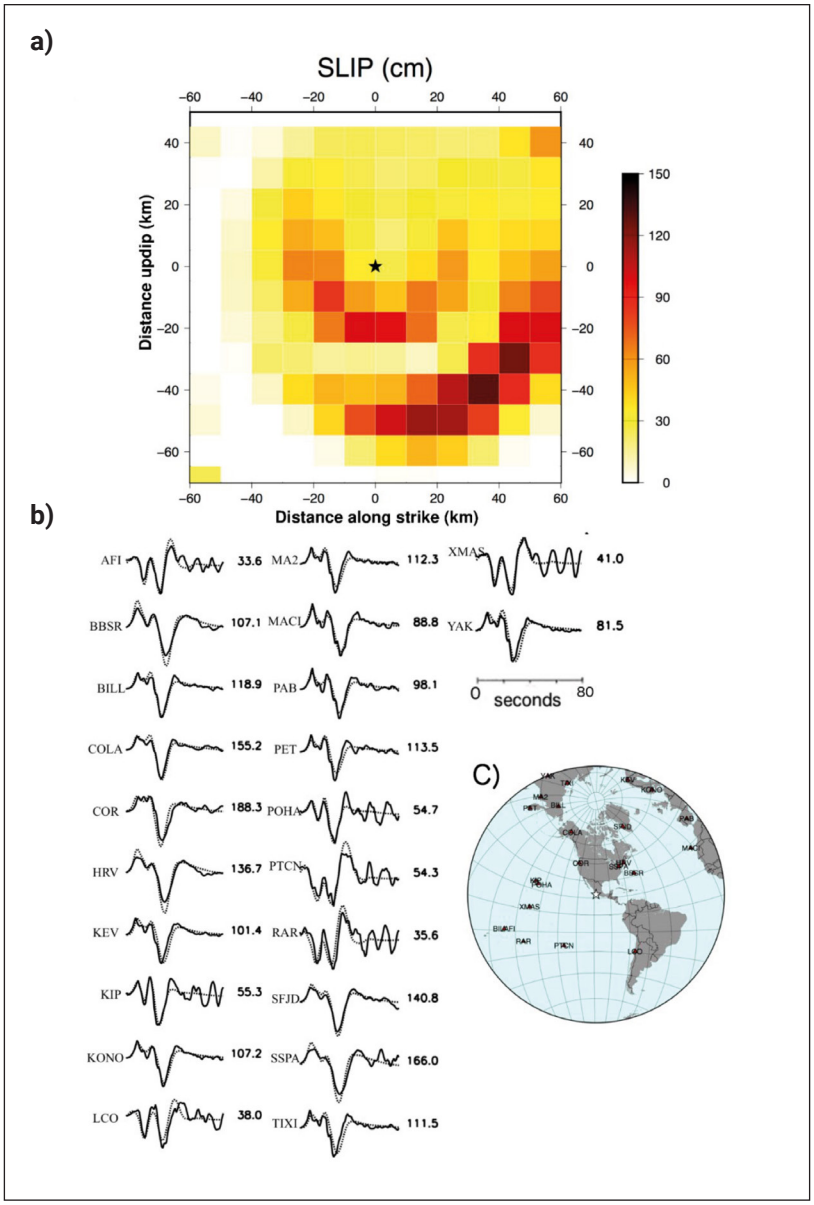

Figure 4. a) Coseismic slip (in cm) obtained for the 19 September 2022 earthquake from the rapid inversion of teleseismic *P* waves. The view is from the top of a 120-km by 120-km fault divided into 144 square subfaults. The fault strike, dip and rake are 287°, 18°, and 86°, respectively. The star shows the hypocenter location. b) Fits between observed (solid) and theoretical (dotted) *P* waveforms for an inferred seismic moment of 1.9×10^{27} dyne-cm (M_w 7.5). Numbers to the right are the peak amplitudes of the observed records (in microns). C) Azimuthal distribution of stations used in the inversion.

mum slip of 1.3 m (Figure 4). This result was obtained within three hours of the occurrence of the event. The rapid *P*-wave inversion methodology was also applied following the M_w 6.7 aftershock of 22 September. We used fault dimensions of 80 km by 80 km, the minimum size allowed in the rapid *P*-waveinversion procedure designed to analyze earthquakes of magnitude M_w 7 or greater (Mendoza and Martinez-Lopez, 2022). For this event, we used the epicenter calculated by the SSN (Table 3; **http://www2.ssn.unam.mx:8080/sismos-fuertes/)** and the focal depth obtained by the USGS. The distribution of coseismic slip for the shallow-dipping plane (Figure 5) shows a single 20 km by 20 km rupture area with a peak of 1.1 m extending primarily downdip from the hypocenter. Although the results obtained for both events are preliminary, they provide a general overview of the locations of high slip and the possible direction of coseismic rupture.

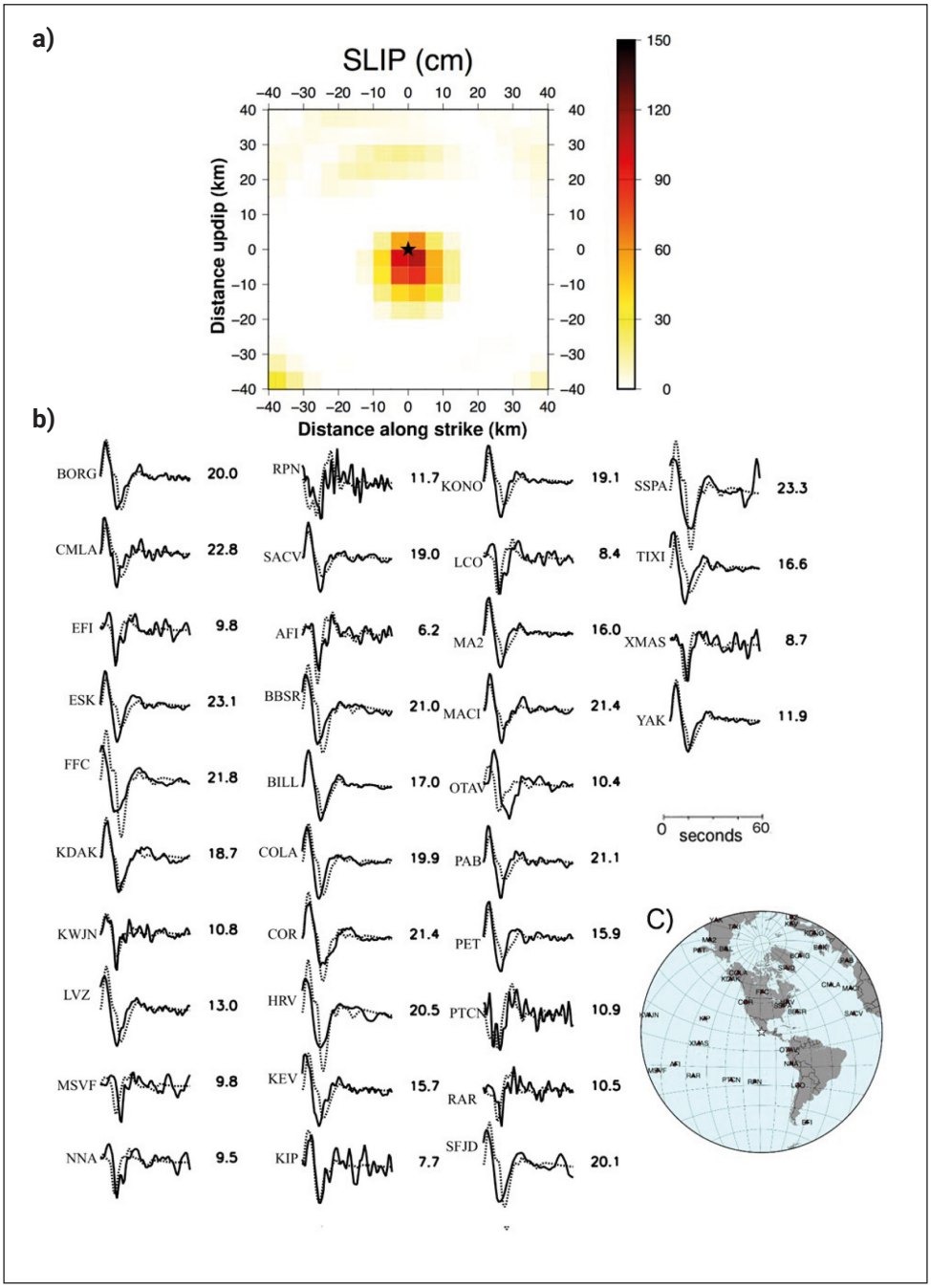

Figure 5. a) Coseismic slip (in cm) obtained for the 22 September 2022 aftershock from the rapid inversion of teleseismic *P* waves. The view is from the top of an 80-km by 80-km fault divided into 256 square subfaults. The fault strike, dip and rake are 291°, 18°, and 90°, respectively. The star shows the hypocenter location. b) Fits between observed (solid) and theoretical (dotted) *P* waveforms for an inferred seismic moment of 1.4×10^{26} dyne-cm (M_w 6.7). Numbers to the right are the peak amplitudes of the observed records (in microns). C) Azimuthal distribution of stations used in the inversion.

Both inversions use five 1 s time windows to parameterize the slip duration on the fault.

On 7 October 2022, USGS updated its previously published finite fault model of the mainshock (**http://earthquake.usgs.gov/earthquakes/eventpage/us7000i9bw/finite-fault).** The new fault model is based on the analysis of a more extensive dataset: 41 teleseismic *P* waves, 23 teleseismic SH waves and 55 long-period surface waves, and observations from 7 high-rate GNSS stations and 11 static GNSS sites. The model also uses the hypocenter reported by the SSN (Table 2) to correct for the location bias. Figure 3 reproduces the USGS finite fault model. As this model is based on a more extensive dataset, we shall use it in our further analysis. In this model, M_0 and maximum slip (D_{max}) are $2.73 \cdot 10^{20}$ Nm and 3.2 m, respectively. Following Ye *et al.* (2016) and Lay *et al.* (2016), we ignore subfaults with slip $D < 0.15D_{max}$ as the low slip areas are likely to be poorly resolved. The trimmed area, A, enclosing $D \geq 0.15D_{max}$, is 3600 km^2. M_0 released over this area is $2.52 \cdot 10^{20}$ Nm and the average slip, $<D>$, is 1.48 m. The relation $\Delta\sigma_s = (7\pi^{3/2}/16)(M_0/A^{3/2})$, where $\Delta\sigma_s$ is the static stress drop (Kanamori and Anderson, 1975), yields $\Delta\sigma_s$ of 3.7 MPa.

Moment-scaled radiated seismic energy, REEF, and number of aftershocks

Radiated seismic energy, E_R, for the mainshock, from teleseismic data, is $3.44 \pm 0.13 \cdot 10^{15}$ J (Me = 7.46). In the estimation of E_R, we followed the methodology of Boatwright and Choy (1986), and included a stronger attenuation correction for subduction earthquakes discussed by Pérez-Campos

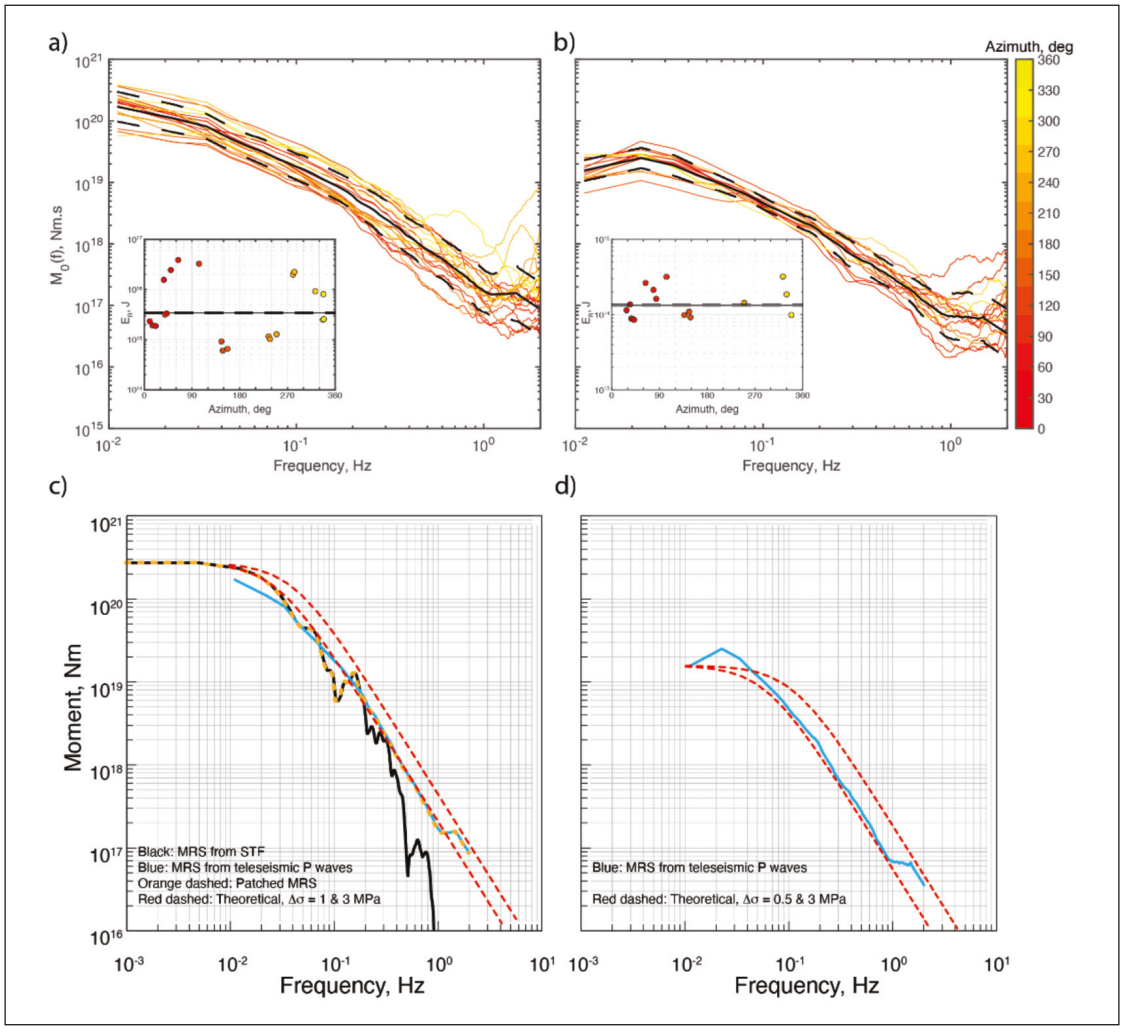

Figure 6. Radiated seismic energy and source spectra for the mainshock and the largest aftershock. a) Source spectra for the mainshock, obtained at each station, color coded by azimuth. The black solid line shows the geometric mean, and the black dashed lines, its confidence interval. The inset shows the values of radiated seismic energy estimated at each station, color coded by azimuth. b) Same as a) but for the largest aftershock. c) Source spectrum from the mainshock. The source spectrum from the source time function reported by the USGS (**https://earthquake.usgs.gov/earthquakes/eventpage/us7000i9bw/finite-fault**) is shown in black; the one obtained from teleseismic data (this study), in blue; the patched source spectrum, as an orange dashed line; and theoretical source spectra with 1 and 3 MPa, as red dashed lines. d) Source spectrum of the aftershock. The source spectrum obtained from teleseismic data (this study) is shown in blue; and theoretical source spectra with 0.5 and 3 MPa, as red dashed lines.

and Beroza (2001) and Pérez-Campos *et al.* (2003). Following Boore and Joyner (1997) we applied a correction for generic hard site. E_R estimation shows a strong azimuthal dependence that can also be appreciated from the moment rate spectrum (*MRS*) at each station (Figure 6). The larger values are obtained at stations to the north, while the smaller once occur to the south. We build the source spectrum by patching, at low frequencies (< 0.2 Hz), the moment rate function obtained from the source time function reported by the USGS (**http://earthquake.usgs.gov/earthquakes/eventpage/us7000i9bw/finite-fault),** and, at high frequencies (≥ 0.2 Hz), the source spectrum obtained from teleseismic data. The resulting *MRS* fits the theoretical spectrum from the Brune source model (Brune, 1970) with a stress drop of 1 MPa (Figure 6c). The moment-scaled radiated energy, E_R / M_0, is $1.27 \cdot 10^{-5}$, a value similar to those reported for other large Mexican thrust earthquakes, which range between 1.0 and $3.3 \cdot 10^{-5}$ with the exception of earthquakes whose rupture areas extend up to the trench, e.g., Colima-Jalisco earthquake of 9 October 1995 ($E_R / M_0 = 5.6 \cdot 10^{-6}$) (Table 5). E_R / M_0 of the 2022 mainshock is close to the world-wide average of ~ $1 \cdot 10^{-5}$ (e.g., Ye *et al.*, 2016a).

For the major M_w 6.7 aftershock of 22 September, E_R is $1.33 \pm 0.06 \cdot 10^{14}$ J ($M_e = 6.51$) so that $E_R / M_0 = 8.31 \cdot 10^{-6}$; in this case, E_R and source spectrum at individual station do not show any azimuthal dependence (Figure 6b). *MRS* of the earthquake is well fit by a Brune source model with a stress drop of 0.5 MPa (Figure 6d).

We computed radiated energy enhancement factor, REEF, for the 2022 mainshock. REEF, a measure of rupture complexity, recently introduced by Ye *et al.* (2018). It is the ratio of measured radiated energy, E_R, to the calculated minimum energy for a source of the same M_0 and duration, $E_R / E_{R\text{-min}}$. A smaller REEF value corresponds to a simpler source and vice versa. The duration, T, of the moment rate function (MRF) of the 2022 earthquake from the USGS finite-fault modeling is 32 s. $E_{R\text{-min}}$, corresponding to $M_0 = 2.73 \cdot 10^{20}$ Nm and T of 32 s, is $4.1 \cdot 10^{14}$ J (Equation 1 of Ye *et al.*, 2018), which gives a relatively low REEF value of 8.5. REEF values are consistently low for southern Mexico to Middle America subduction thrust earthquakes (Table 5; Ye *et al.*, 2018), reflecting the simplicity of the MRF of the earthquakes along this segment of the subduction zone.

The relatively small number of $m_b \geq 5$ aftershocks is also a characteristic of large Mexican subduction thrust earthquakes (Singh and Suárez, 1988). For the 2022 earthquake there were four aftershocks with $m_b \geq 5$ in 30-day period. Table 5 gives the number of aftershocks, N, in a 30-day period with $m_b \geq 5$ and log (N / Ne), where Ne is the expected number of aftershocks derived from regression analysis of

Table 5. Moment-scaled radiated seismic energy, REEF, and number of $m_b \geq 5$ aftershocks in one-month period of large Mexican subduction thrust earthquakes (Modified from Iglesias *et al.*, 2022)

Date Location	**M_0, Nm**	**M_w**	**E_R / M_0**	**REEF***	**N(mb ≥ 5)#**	**log(N/Ne)+**
14/09/1995 Copala	$1.28 \cdot 10^{20}$	7.3	$1.83 \cdot 10^{-5}$	4.5	2	-0.659
09/10/1995 Colima-Jalisco	$1.15 \cdot 10^{21}$	8.0	$5.60 \cdot 10^{-6}$	13.8	5	-0.961
25/02/1996 Offshore Pinotepa	$5.55 \cdot 10^{19}$	7.1	$3.34 \cdot 10\text{-}^{6}$	1.8	7	0.085
20/03/2012 Pinotepa	$1.88 \cdot 10^{20}$	7.5	$2.96 \cdot 10^{-5}$	4.4	14	-0.014
18/04/2014 Papanoa	$9.41 \cdot 10^{19}$	7.3	$1.03 \cdot 10^{-5}$	10.1	4	-0.358
16/02/2018 Pinotepa	$7.04 \cdot 1019$	7.2	$1.04 \cdot 10^{-5}$	25.2	7	-0.015
23/06/2020 Huatulco	$1.64 \cdot 1020$	7.4	$2.39 \cdot 10^{-5}$	6.1	4	-0.458
08/09/2021 Acapulco	$3.64 \cdot 1019$	7.0	$2.10 \cdot 10^{-5}$	5.8	1	-0.660
19/09/2022 Michoacán-Jalisco	2.73×1020	7.6	1.27×10^{-5}	8.5	5	-0.561

*REEF: Radiated energy enhancement factor (Ye et al., 2018)

#*N* count includes mainshock as one event

+log*Ne* = M_w - 6.34 (Singh and Suárez, 1988)

world-wide data: log $Ne = M_w - 6.34$ (Singh and Suárez, 1988). Log (*N/Ne*) is negative for six earthquakes including the 2022 earthquake and close to zero for the remaining three. Thus, along the Mexican subduction zone both low REEF and relative lack of aftershocks prevail. Similarly to Iglesias *et al.* (2022), we envision a plate interface that is relatively smooth, containing discrete, compact asperities. Asperities rupture smoothly, generating relatively simple moment rate functions and low values of REEF. As the rupture area and adjacent plate interface is also smooth and homogeneous, there is a relative lack of aftershocks at $m_b \geq 5$ level.

Comparison with earthquakes of 30 January 1973 (M_S 7.5, M_w 7.6) and 15 April 1941 (M_S 7.7)

From the aftershock locations, and the relative locations of the main shock and aftershocks, Reyes *et al.* (1979) suggested that the rupture during the 1973 earthquake began to the SE, near the region of high aftershock activity, and propagated to the NW. For the 2022 earthquake, the unilateral rupture propagation to the NW is, of course, well established. In as much as the aftershock areas of the 2022 and 1973 earthquakes overlap (Figure 3), and their magnitudes are similar (Table 1), it is possible that the two events broke roughly the same area, had similar gross source characteristics perhaps even with similar source directivity.

We note, however, that the finite fault model of the 1973 earthquake constructed by Santoyo *et al.* (2006) using teleseismic *P* waves does not show a NW directivity. This may be due to poorer quality and limited quantity of data (8 stations) used in the inversion for the 1973 earthquake. Even with far more data of better quality (20 stations) for the 2022 earthquake, the inversion of teleseismic *P* waves yields a solution that is only a rough approximation of the one obtained by the USGS finite fault modelling based on a more extensive dataset (compare Figures 4 and 3).

For the 1973 earthquake, Reyes *et al.* (1979) noted that M_0 increased by a factor of about 2 as the period increased from 100 to 300 s. They attributed this increase to possible slow slip before or after the main slip or to unknown errors in the estimation of M_0 at lower periods. For the 2022 earthquake, we computed M_0 from *W*-phase CMT inversion of the regional broadband seismograms with different band-pass filters and found negligible change in M_0 (M_w) with period (Table 6). Thus, either the source processes of the 1973 and 2022 earthquakes differed or else the dependence of M_0 on period for the 1973 earthquake was due to unknown errors.

Much less is known about the 1941 earthquake. Kelleher *et al.* (1973) relocated the mainshock and two of its aftershocks. This area roughly coincides with the aftershock areas of the 1973 and 2022 earthquakes.

To test whether the 1941, 1973, and 2022 earthquakes ruptured roughly the same area, we compared their Galitzin seismograms (Z component) at DBN. We note that repeating events have the same rupture area and slip and give rise to identical seismograms.

The 1941 and 1973 analog records were vectorized and the time series was sampled at an evenly time interval using TIITBA-GUI (Corona-Fernández and Santoyo, 2022). Galitzin record of the 2022 earthquake was synthesized from broadband DBN seismogram as the operation of the Galitzin seismograph was discontinued in December 1994 (Dost and Haak, 2006). We first note that the three events have complex *P* waves that bear some resemblance (Figure 7).

Table 6. Sensitivity of W-phase solution of the 2022 mainshock to the band-pass filter setting. Centroid depth and epicenter fixed to that reported by the SSN (Table 2). Dip is fixed at 15^0. Note that M_w is nearly independent of the band-pass (BP) filter setting

Band pass (mhz)	Azimuthal gap	Stations/ channels	M_w
2.0 – 4.0	213^0	11/12	7.58
2.5 – 5.0	208^0	27/45	7.58
3.0 – 6.0	208^0	27/59	7.60
3.5 – 7.0	208^0	28/64	7.59
4.0 – 8.0	208^0	29/70	7.58
4.5 – 9.0	208^0	28/70	7.58
5.0 - 10.0	208^0	29/69	7.58

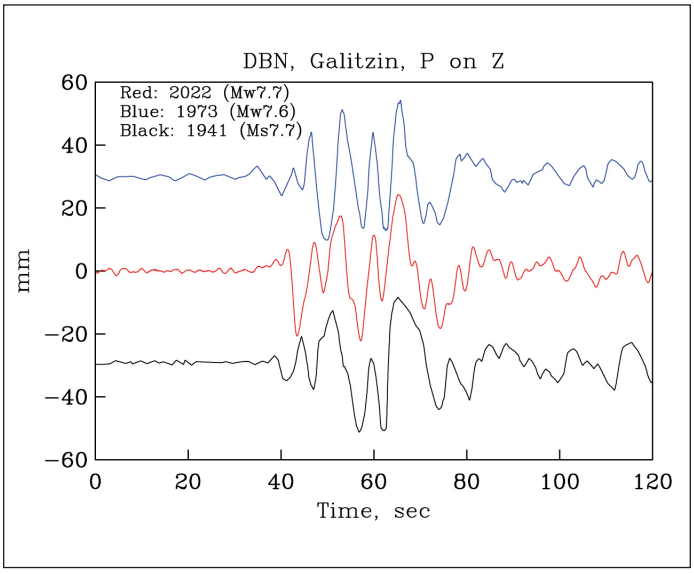

Figure 7. *P* wave on the DeBilt (DBN) Galitzin seismogram (Z-component) of the Michoacán-Colima earthquakes of 2022, 1973, and 1941. Complexity of the *P* wave is similar for the three earthquakes.

In Figure 8, the seismograms of 2022 and 1973 are compared over three different time windows. The waveforms are clearly not identical. Our tests, however, show that the surface waves on the Galitzin seismograms at DBN of events along the Mexican subduction zone which are 20 to 30 km apart greatly differ from each other (Singh *et al.*, 2022). In as much as the character of the surface waves from the 1973 and 2022 earthquakes are similar (bottom frame, Figure 8), we surmise that the rupture areas of the two events were less than 30 km apart. From the similarity of the aftershock areas, the waveforms at DBN, and the magnitudes of the 2022 and 1973 earthquakes, we conclude that they were quasi-repeated events. In other words, these two events may have ruptured roughly the same area. If so, the return period was 50 years. We recall that the finite fault modeling yields an average slip of about 1.48 m for the 2022 earthquake. As the plate convergence rate is 6.0 cm/yr (DeMets *et al.*, 2010), this gives a coupling ratio of 0.49.

The Galitzin seismograms of 2022 and 1941, shown in Figure 9, exhibit little resemblance. The difference is marked in the character of the surface waves (bottom frame). Since the waveform of the 1941 earthquake differs significantly from those of the 2022 and 1973 events, it most likely did not rupture the same area as the other two.

Directivity and azimuthal dependence of ground motion

As discussed above, a source directivity towards NW during the mainshock is clearly seen in the results of inversion of slip on the fault as well as in plots of *MRS* and E_R as a function of azimuth. A downdip directivity is also visible, albeit weakly, in the slip inversion of the M_w 6.7 aftershock. In this section, we examine, in detail, the effect of the source directivity on the ground motion at regional distances. The stations whose recordings are used in the analysis are shown in Figure 10.

(a) Visual examination of the recordings

Figure 11a compares mainshock waveforms at stations CJIG (azimuth $\phi = 308^0$) and ZIIG ($\phi = 109^0$). The stations are located at nearly the same distance but in opposite directions (Figure 10). The shorter duration and higher amplitude of the intense part of the motion at CJIG compared with ZIIG strongly suggests a rupture propagation towards the NW. The waveforms during the aftershock at the same two stations

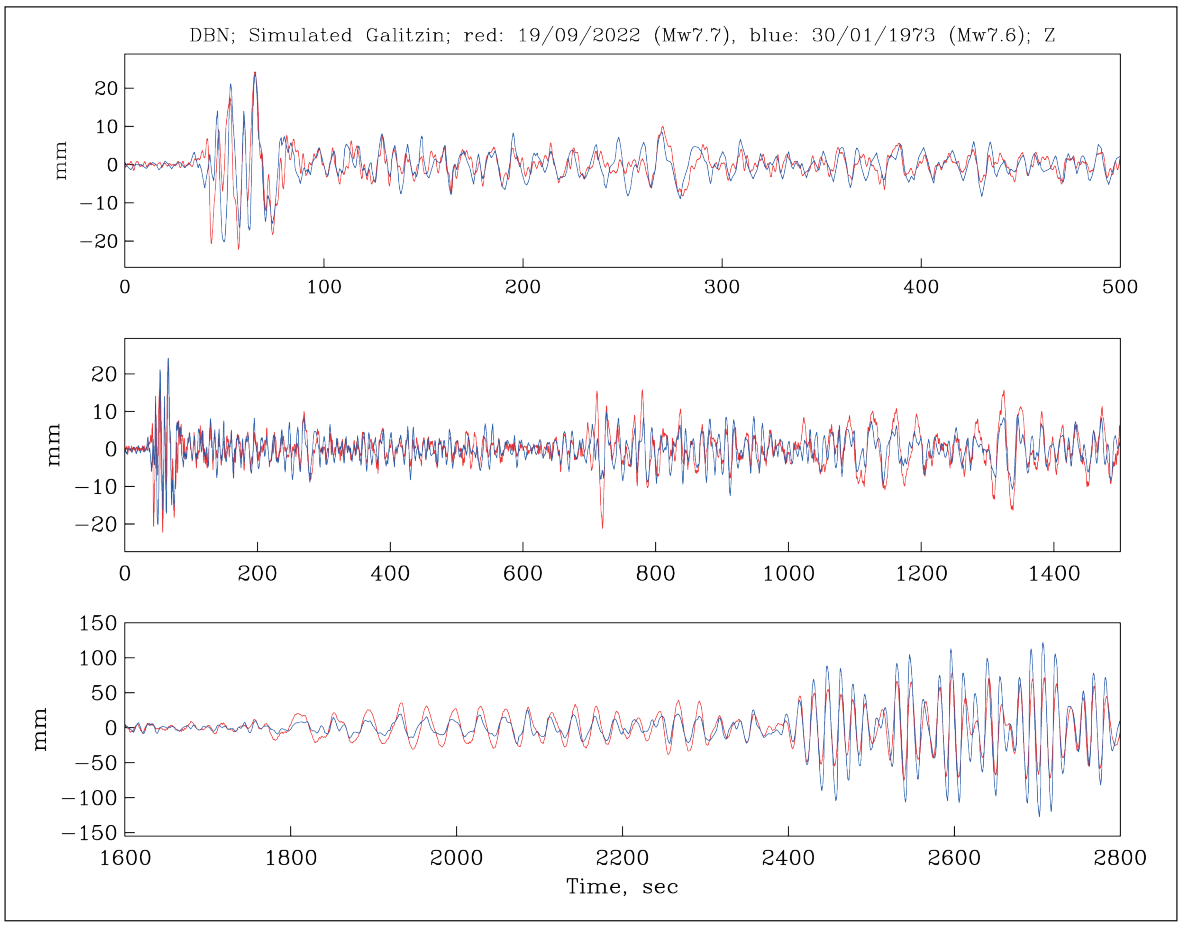

Figure 8. DBN Galitzin seismograms (Z-component) of the Michoacán-Colima earthquakes of 2022 and 1973. The seismograms, displayed in three time windows, are similar though not identical. The events may be classified as quasi-repeated earthquakes.

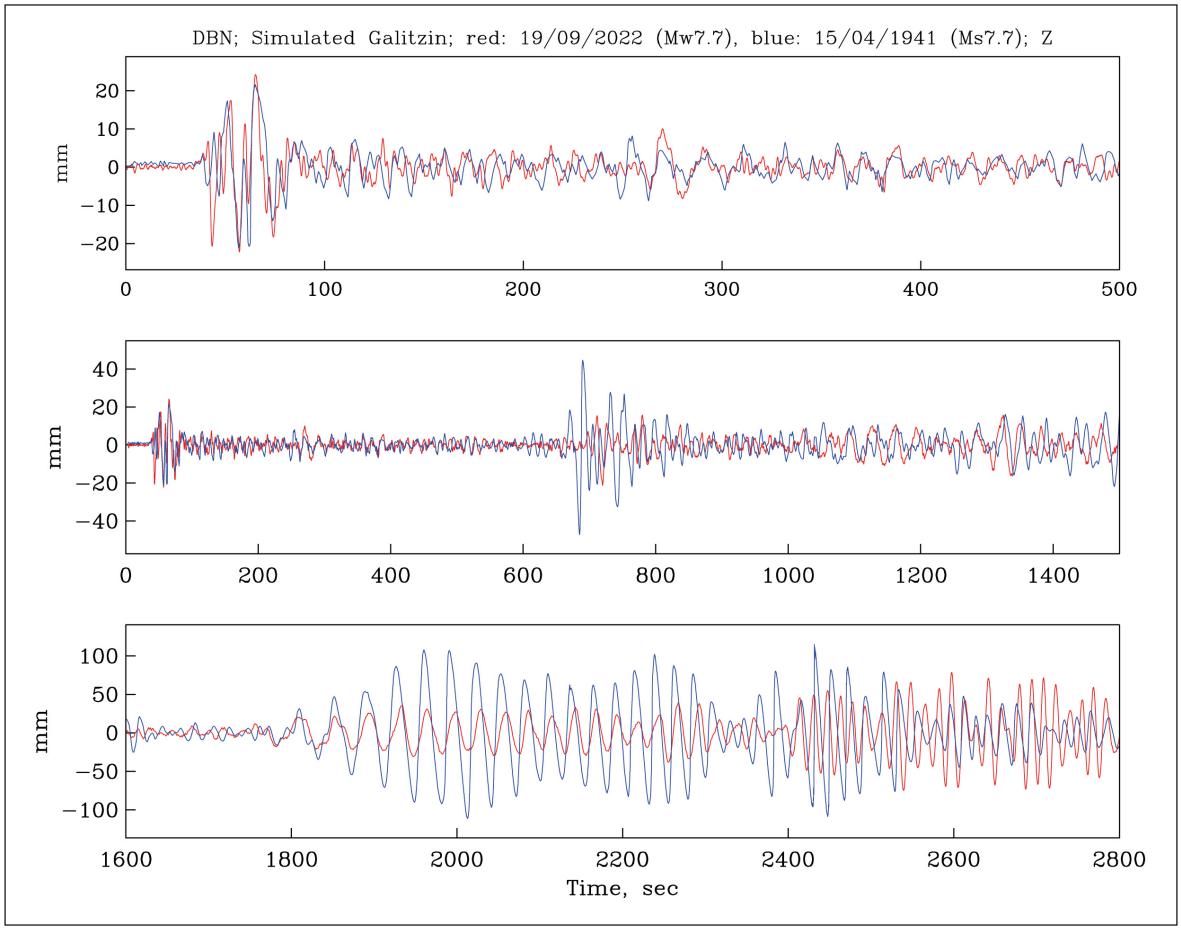

Figure 9. DBN Galitzin seismograms (Z-component) of the Michoacán-Colima earthquakes of 2022 and 1941 earthquakes. The seismograms, displayed in three time windows, are dissimilar. The events, most likely, did not share the same source area.

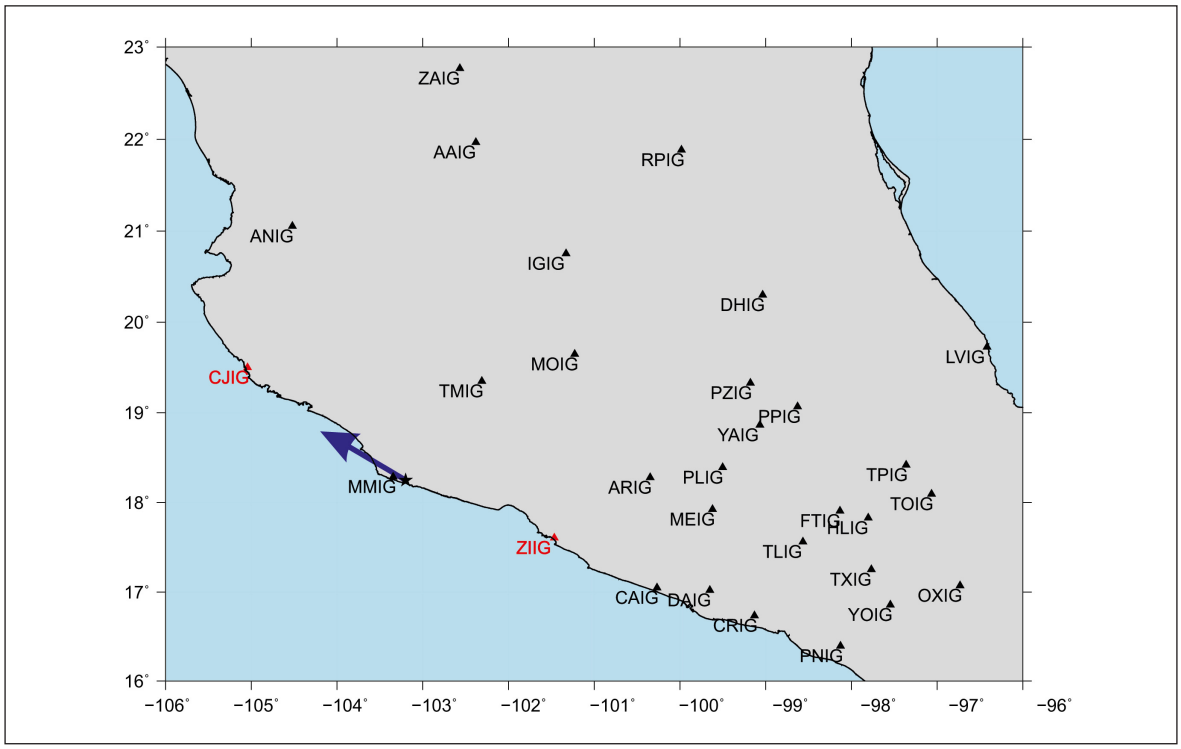

Figure 10. Some of the regional SSN stations whose recordings are analyzed in this study. PZIG is located in CU, Mexico City. Blue arrow near the station MMIG indicates the direction of rupture propagation during the 2022 mainshock.

are shown in Figure 11b. The accelerations, in this case, are higher at ZIIG (which may be due to site effect) than at CJIG, while velocities and displacements are about the same. These waveforms do not support along strike directivity during the major aftershock; rupture propagation to the east is certainly viable.

(b) Spectral ratios of the mainshock to the aftershock ground motions

Under the assumption that the mainshock and the aftershock are collocated and have similar focal mechanisms, the spectral ratio of the ground motion at a given station provides the ratio of their moment rate spectrum, *MRS*. In the absence of directivity, the *MRS* is expected to be independent of azimuth. Figures 12a,b,c,d illustrate the spectral ratios at selected stations, each frame comprising stations in a range of azimuth with respect to the mainshock directivity. Frame (a): rupture propagating towards the stations; frame (b): station perpendicular to the rupture propagation; frame (c) and (d): rupture propagating away from the station. The spectral ratios were computed for each of the three components of the ground motion. The figures also show the geometric mean of the ratios in each frame. For reference, the theoretical spectral ratio corresponding to Brune ω^2 source model (Brune, 1970) with constant stress drop of 3 MPa is included in each frame.

A strong dependence of the ratios on azimuth is immediately obvious. With respect to the theoretical spectral ratio, the observed ratios are higher in frame (a), about the same in frame (b), but lower in both frames (c) and (d). Directivity towards NW during the mainshock and an absence of ESE directivity during the aftershock are consistent with the observations.

(c) PGA and PGV ratios of mainshock to aftershock

The directivity effect should also be reflected in the azimuthal dependence of *PGA* and *PGV* ratios of the mainshock to the aftershock. Horizontal and vertical *PGA* ratios, plotted in Figure 13a, are a strong function of station azimuth φ but not of distance *R*. Here, horizontal $PGA = [(A_N^2 + A_E^2) / 2]^{1/2}$,

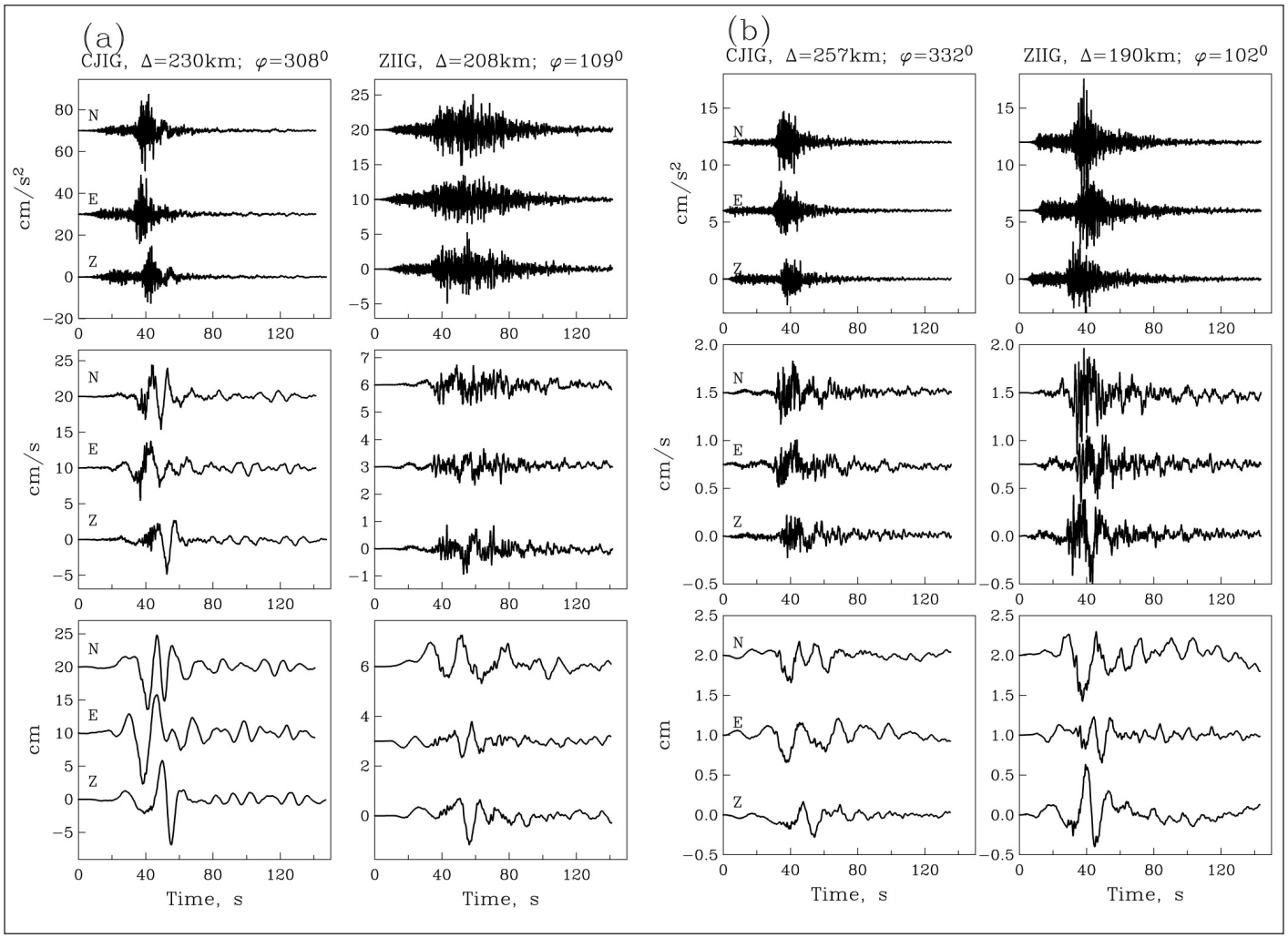

Figure 11. (a) Comparison of mainshock waveforms at stations CJIG (azimuth $\phi = 308^0$) and ZIIG ($\phi = 109^0$). The stations are located at nearly the same epicentral distance but in the opposite direction (Figure 10). (b) Same as (a) but for the M_w 6.7 aftershock.

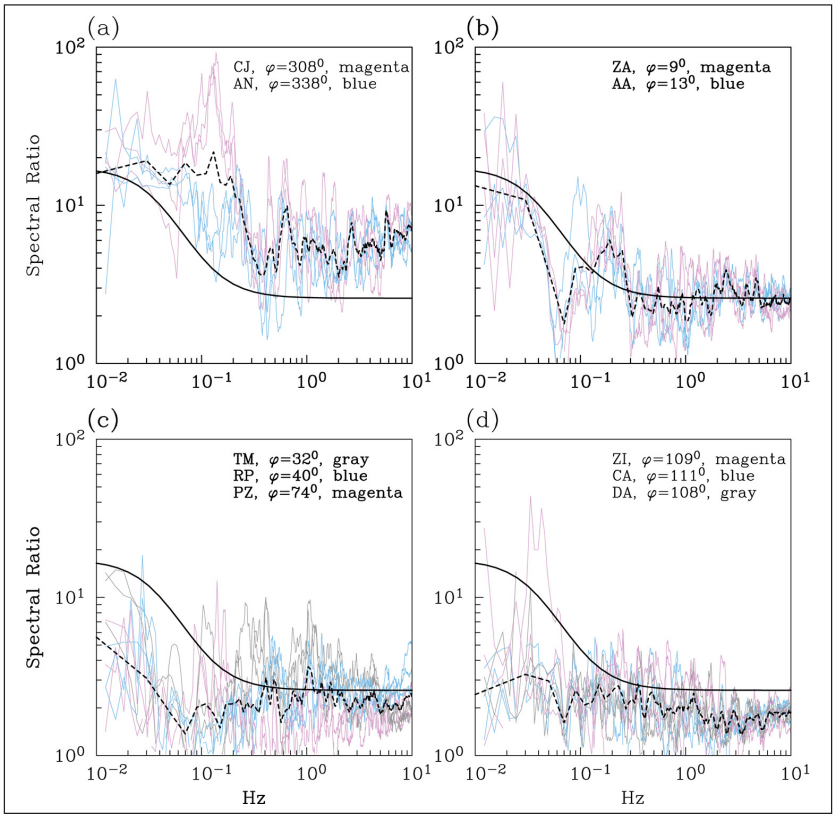

Figure 12. Spectral ratio of ground motion at selected stations during the mainshock to the M_w 6.7 aftershock. Frames (a) to (d) show the ratios at stations grouped in azimuthal range. The Figures also show geometric mean of the ratios in each frame. For reference, theoretical spectral ratio corresponding to Brune ω^2 source model are included (see text).

where A_N and A_E are maximum accelerations on NS and EW components. The ratios rapidly decrease from about 12 to 3 at stations in the azimuthal range 300° < φ < 360°. These stations are in the forward direction for the mainshock and, possibly, in the backward direction for the aftershock. The ratio slowly decreases from about 3 to 1 in the range 0° < φ < 115°. Stations in this azimuthal range are in the backward direction for the mainshock and, probably, in the forward direction for the aftershock. Again, the ratios in the figure are in agreement with the directivity of the two earthquakes. The effect of the directivity on the *PGA* ratios is better appreciated by comparing them with the horizontal *PGA* ratio of 2.5 expected from the ground motion prediction equation (GMPE) for Mexican subduction thrust earthquakes of M_w 7.6 and M_w 6.7 (Arroyo *et al.* 2010).

PGV ratios, shown in Figure 13b, follow the same trend as the *PGA* ratios. However, the maximum *PGV* ratios in the azimuthal range 300° < φ < 360° exceed 20.

(d) PGA and response spectral amplitudes as function of azimuth and distance

PGA and Sa (T=2 s) for the mainshock and the aftershock are plotted in Figure 14 as a function of the closest distance from the fault surface, *R*rup. Only stations with *R*rup < 600 km are included in the figure. The stations are grouped in 3 bins as a function of their azimuth: bin 1: $330^0 \le \varphi \le 30^0$; bin 2: $30^0 < \varphi \le 90^0$; bin 3: $90^0 < \varphi \le 120^0$. All data, except one, are contributed by stations at Rrup > 120 km. Superimposed on the data are the predicted curves from the GMPE of Arroyo *et al.* (2010). We note that: (i) In general, *PGA* values are above the predicted curves for both events irrespective of the bin. (ii) Sa (T=2 s) values for the aftershock in all bins are greater than the predicted curve. The values are smaller than predicted in bin 3 for the mainshock, consistent with its NW source directivity.

Ground motion in the Valley of Mexico

Since there was a difference of 0.9 in the magnitude of the mainshock and the major, M_w 6.7 aftershock, it was surprising that they were felt with nearly equal intensity in the Valley of Mexico. At CU, a hill-zone reference site in Mexico City, the *PGA* on the NS, EW, and Z components during the mainshock and the aftershock were (5.5, 4.5, 2.9 gal) and (6.3, 4.2, 2.5 gal), respectively. Was the source directivity the cause of the similarity of the *PGA*s?

A site-specific GMPE for CU from subduction thrust earthquakes has been recently developed by Arroyo *et al.* (2022). Figure 15 compares the observed Sa with the predicted ones for M_w 7.6 and M_w 6.7 earthquakes. As expected, the observed Sa curves are similar. Predicted Sa for an M_w 7.6 earthquake, on the other hand, is significantly higher than the observed one. The converse is true for the

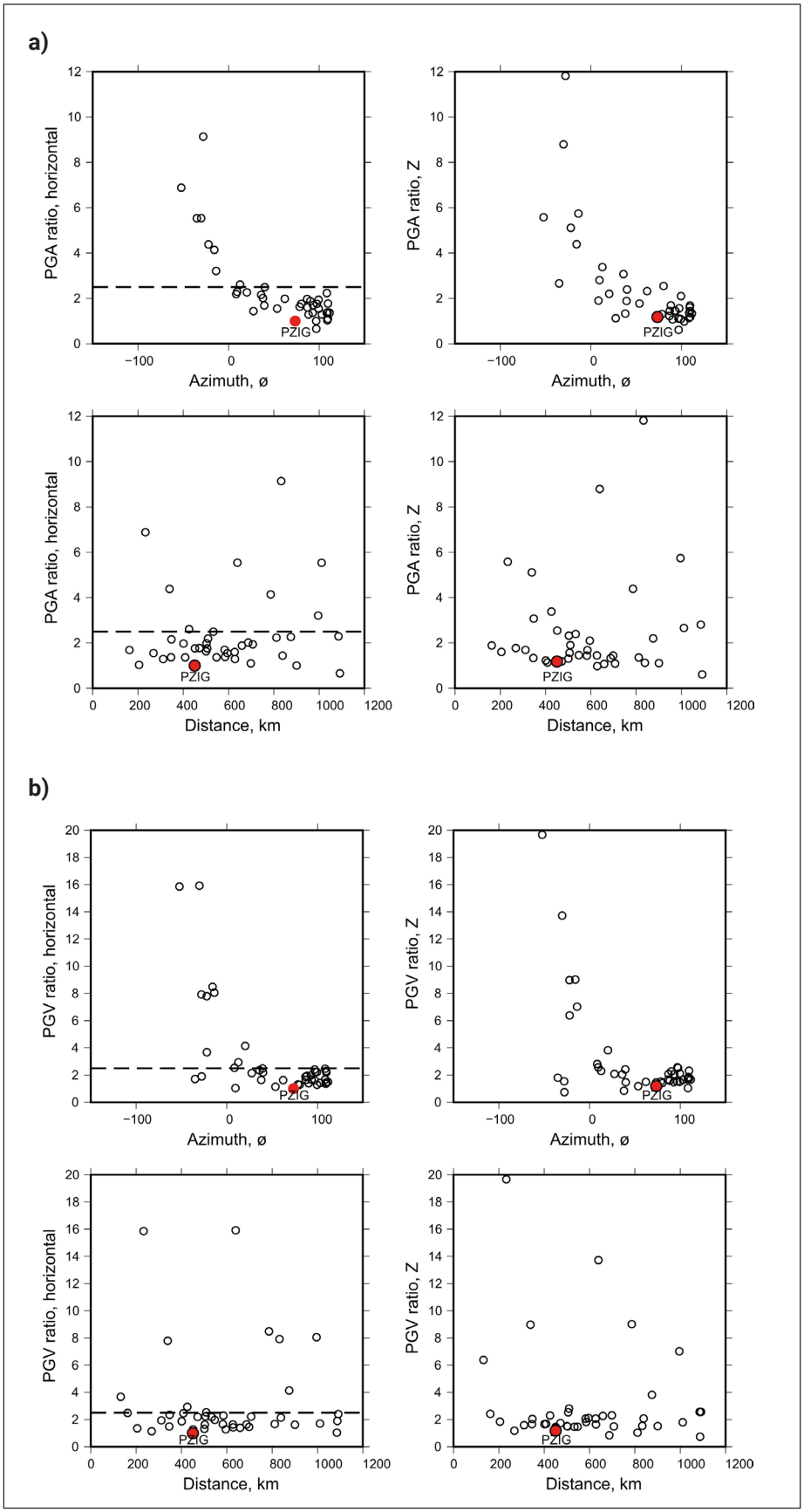

Figure 13. Peak ground motion ratios of the mainshock to the M_w 6.7 aftershock as a function of azimuth and distance. (a) PGA ratios. Dashed horizontal line shows the predicted ratio of 2.5 for the horizontal component by the GMPE of Arroyo *et al.* (2010). Station PZIG, shown by a red dot, refers to a station in CU, Mexico City. (b) PGV ratios. The ratios are strongly dependent on azimuth and are independent of distance.

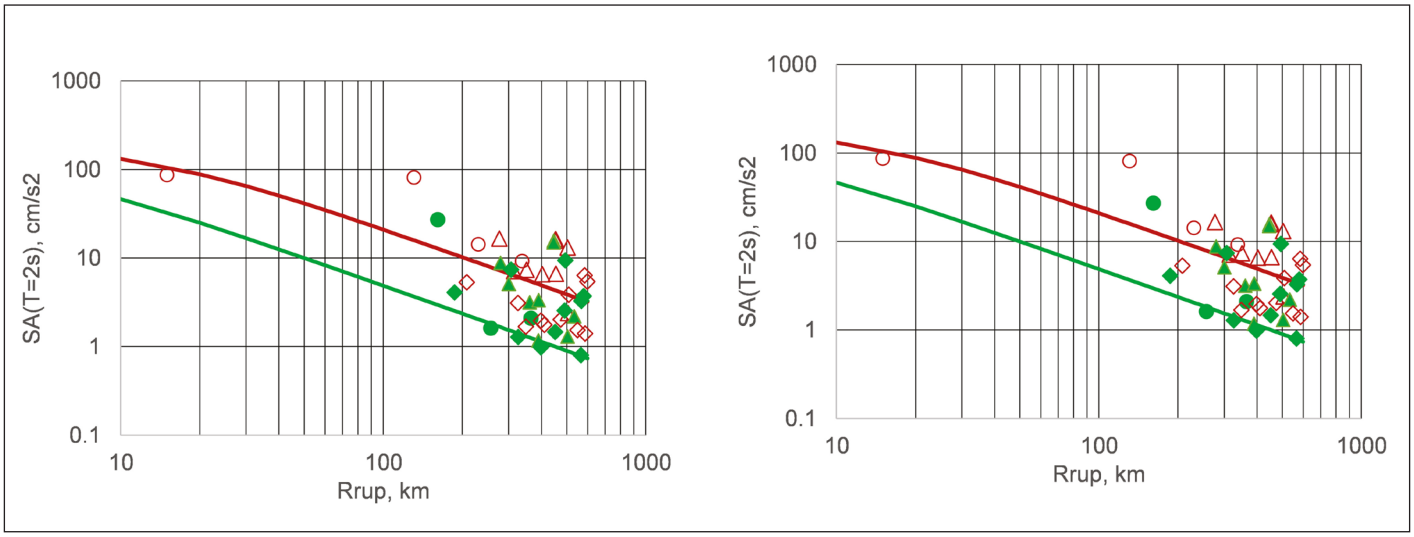

Figure 14. PGA and Sa (T=2 s) during the M_w 7.6 mainshock (red symbols) and the M_w 6.7 aftershock (green symbols) as a function of the closest distance from the fault surface, Rrup.
Circles: bin 1 ($330^0 \leq \varphi \leq 30^0$), triangles: bin 2 ($30^0 < \varphi \leq 90^0$), diamonds: bin 3 ($90^0 < \varphi \leq 120^0$). Continuous lines are median predictions from the GMPE of Arroyo *et al.* (2010).

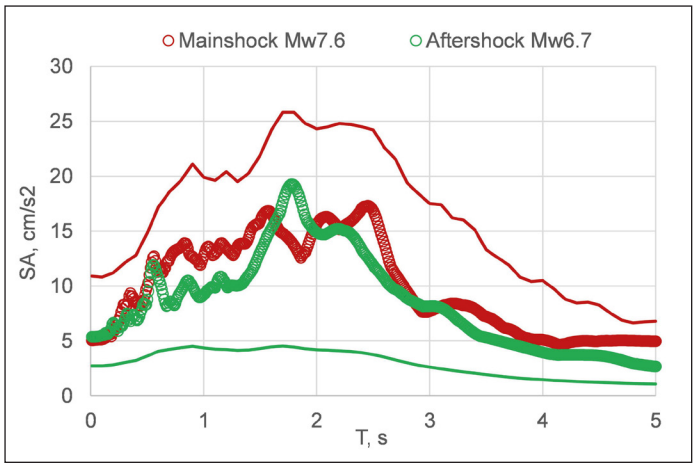

Figure 15. Observed Sa at CU, Mexico City, during the M_w 7.6 mainshock (red circles) and the M_w 6.7 aftershock (green circles). Continuous lines are median predictions (red: M_w 7.6, green: M_w 6.7) from the GMPE of Arroyo *et al.* (2022). The trends are consistent with rupture directivity away from CU during the mainshock and towards CU during the aftershock.

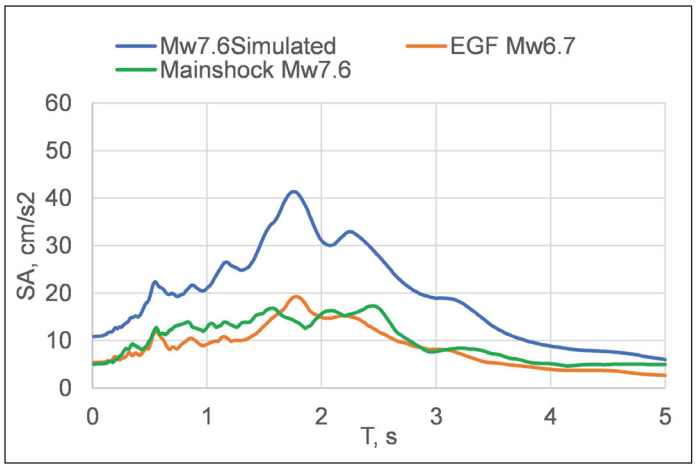

Figure 16. Median of Sa simulations at CU for a postulated M_w 7.6 event using the M_w 6.7 aftershock recording as the empirical Green´s function. The observed Sa at CU during the M_w 7.6 mainshock and the M_w 6.7 aftershock are shown for comparison.

M_w 6.7 aftershock: the observed Sa is much greater than expected. The source directivity away from CU during the mainshock explains the smaller Sa. Greater Sa during the aftershock may be attributed to rupture towards CU.

To further appreciate the role played by directivity, we used the CU recording of the M_w 6.7 aftershock as an empirical Green´s function (EGF) and synthesized ground motion from a target M_w 7.6 earthquake. A method developed by Ordaz *et al.* (1995) was followed in the synthesis. The stress drop, $\Delta\sigma$, was assumed to be the same for both events and taken as 3 MPa. The median of Sa simulations for the postulated M_w 7.6 event as well as the observed Sa during the mainshock are shown in Figure 16. We find that an M_w 7.6 earthquake with directivity similar to the aftershock would have produced Sa at CU about 2.5 times greater than the observed one.

Probability of having observed three major earthquakes on the same day

Let us estimate the probability of having observed what we observed: three major earthquakes ($M \geq 7$) that occur on exactly the same day in the last 120 years. Let's start with basic data and an assumption:

(1) In central Mexico, an average of 0.46 earthquakes occur with $M \geq 7$ per year; that is, on average one every 2 years, more or less.

(2) We assume that, in time, earthquakes occur as a Poisson process; this is relevant in order to know the probability distribution of the number of events that we would observe in any given year

It is not difficult to calculate the probability that, in the span of 120 years, we would have observed 2 or 3 earthquakes occurring on the same day. On September 19, let's say, but the probability would be the same if we chose another date. Although the calculation is not difficult, it is easier to calculate the probabilities by simulation.

Using a sample of 10 million possible realizations from those 120 years, we obtained that the probability of having observed 2 events on September 19 is 0.0103 and the probability of having observed 3 is 0.0005154.They seem improbable events. But, in reality, this is not the probability that interests us. Deep down, it strikes us that we have had 3 major earthquakes on the same date, not specifically on 19 September. Indeed, if we had observed 3 major earthquakes on, say, 24 May, we would be just as surprised.

So, the probability we are interested in is the probability of having observed 3 major earthquakes on the same date, not necessarily September 19. This is more difficult to calculate with combinatorial analysis (there is a closed formula, but complicated to apply), although just as easy to calculate with simulations. We obtain that the probability of having observed 2 earthquakes on the same date, whatever it may be, is 0.98 and the probability of having observed 3 earthquakes is 0.18.

This is amazing. According to this analysis, it is extremely likely to have two large earthquakes on the same date if we look at 120 years at a rate of 0.46 earthquakes/year. And on the other hand, the probability of observing 3 is low, but not astronomically low. If the probabilities are that big, both events should have already happened. Well, yes: before 19 September 2022 there were already 6 pairs of large events that had occurred on the same dates and another triad of events that occurred on 7 June (7 June 1911, M_s 7.7; 7 June 1982, 06:52, M_s 6.9; 7 June 1982, 10.59, M_s 7.0). We just didn't remember.

Why choose an observation period of 120 years? We chose 120 years because, on the one hand, it is the period (1900-2022) in which we consider that the earthquake catalog is complete for $M \geq 7$. On the other hand, we chose it because it seems that we would be equally surprised if the first event of the sequence of 3 on the same date had occurred in 1910, let's say, and not in 1985; but maybe we wouldn't be so surprised, so we calculated the probabilities for other lapses (Table 7). We confirm that, in reality, what we observed was not so improbable.

Table 7. Probabilities of observing 2 and 3 events large earthquakes in central Mexico on any date

Observation time (yr)	Probabilities of:	
	Observing 2 on any date	Observing 3 on any date
40	0.39	0.0086
80	0.84	0.061
120	0.98	0.18

Discussion and conclusion

There is evidence suggesting that the 2022 earthquake (M_s 7.6, M_w 7.6) is a quasi-repeat of the 1973 event (M_s 7.5, M_w 7.6): their aftershock areas approximately coincide, the Galitzin seismograms of the two events at DBN are reasonably similar, and the magnitudes are the same. Curiously, the aftershocks of both earthquakes were also concentrated at the SE end of the rupture area. This distribution of the 1973 aftershocks led Reyes *et al.* (1979) to suggest that the rupture during 1973 propagated towards the NW. This directivity is certainly true for the 2022 earthquake. However, finite fault modelling of the 1973 earthquake by Santoyo *et al.* (2006), using teleseismic *P* waves recorded at 8 stations, does not show the NW directivity. Also, an increase in the seismic moment by a factor of about 2 for the 1973 earthquake as the period increased from 100 to 300 s, noted by Reyes *et al.* (1979), is entirely absent from the 2022 earthquake (Table 6). These differences could be a consequence of increase in the quality and quantity of data and improvement in the analysis technique since 1973. It is also possible that the differences are real and the details of the rupture process of the two events differed even if their source areas were roughly the same.

Reyes *et al.* (1979) suggested that the 1973 earthquake may have been a repeat of the 1941 event (M_s 7.8). Galitzin seismogram of the 1941 earthquake at DBN, however, bears little resemblance with those of the 1973 and 2022 events (Figures 8 and 9) which suggests that the source region of the 1941 earthquake was different from those of the other two events.

A unilateral rupture propagation, along the strike towards the NW, during the 2022 mainshock is a robust feature of the finite-fault models. Azimuthal variation of moment rate spectrum and radiated seismic energy estimated from teleseismic *P* waves also support the NW directivity. According to the USGS finite fault model, the rupture area over which the slip is greater than 15% of its maximum value (3.2 m) is 3600 km^2 (90 km × 40 km). The average slip over this area is 1.48 m, which yields a static stress drop of 3.8 MPa.

If we accept that the 1973 and 2022 earthquakes ruptured the same area, then the recurrence period is 50 years. For a plate convergence rate of 6.0 cm/yr and perfect coupling, the accumulated slip deficit in 50 years would have been 3.0 m.

If we ignore post-seismic slip, then the estimated coupling ratio on this segment of the plate boundary, corresponding to a coseismic slip of 1.48 m, is 0.49. This estimate agrees surprisingly well with the GPS-derived coupling ratio for this segment (Cosenza-Muralles *et al.*, 2022a) and is slightly smaller than the coupling of about 0.6 estimated from InSAR and GNSS data (Maubant *et al.*, 2022). The post-seismic slip, however, may not be negligible. Similar or larger seismic moments than the coseismic moments were released in the post-seismic slip following the earthquakes of 2003 Tecomán (M_w 7.5) and 1995 Colima-Jalisco (M_w 8.0) (Cosenza-Muralles *et al.*, 2022b). The areas of post-seismic slip of these two earthquakes partly overlap their rupture areas and, in both cases, extend further downdip. These earthquakes, however, occurred on the RIVE-COCOS plate boundary (Figure 1). Characteristics of post-seismic slip on the COCOS-NOAM plate interface, where the 2022 earthquake occurred (Figures 1 and 3), might be different, an issue that future studies will, no doubt, address.

Our analysis of ground motions at regional distances confirm the mainshock directivity to the NW. In our study, we focused on the ratio of ground motions during the mainshock and the major M_w 6.7 aftershock, thus minimizing the site effect. These results can be interpreted by a strong NW directivity during the mainshock and an ENE or negligible directivity during the M_w 6.7 aftershock. Because of the directivity, the ground motions in the Valley of Mexico during the 2022 mainshock and the M_w 6.7 aftershock were about the same in spite of 0.9 difference in their magnitudes.

It is well known that the source directivity has a profound effect on the azimuthal variation of ground motion and, hence, in the damage distribution (e.g., Somerville *et al.*, 1997; Koketsu *et al.*, 2016). Directivity has been reported even during small earthquakes (Boatwright, 2007; Calderoni *et al.*, 2013; Seo *et al.*, 2022). Strong directivity was reported during two moderate earthquakes in the Guerrero seismic gap (8 May 2014, M_w 6.5; 11 May 2014, M_w 6.1) (Singh *et al.*, 2019). The recent Acapulco earthquake of 8 September 2021 (M_w 7.0) had a strong NE directivity (Iglesias *et al.*, 2022). Directivity, almost certainly, played a major role in causing damage to Mexico City during the1985, Michoacán earthquake (e.g., Anderson *et al.*, 1986; Kanamori *et al.*, 1993). Similar to the 2022 event, the great Colima-Jalisco earthquake of 1995 (M_w 8.0) had a NW directivity (e.g., Courboulex *et al.*, 1997; Hjörleifsdóttir *et al.*, 2018). Miranda y Marron (1911-1912) mentions that the 7 June 1911 earthquake (M_s 7.7), whose location is poorly known but was in the Michoacán – Colima region, was very strongly felt in Mexico City, causing considerable damage and leaving 40 persons dead. The intensity of the earthquake in the city was much stronger than for earthquakes of similar magnitude that occurred along the coast of Guerrero between 1907 and 1911. Isoseismic contours of the 1911 earthquake are elongated towards the east. Eastward directivity towards Mexico City provides a plausible explanation for the intensity with which it was felt in the city. The earthquakes of 2022 and others events mentioned above once again bring into focus the importance of source directivity in the recorded and simulated ground motion in Mexico.

Finally, we find that observing three major earthquakes ($M \geq 7$) on the same day in central Mexico is not so improbable.

Acknowledgments

Data used in this study were provided by the Servicio Sismológico Nacional (SSN, Mexican National Seismological Service), Red Acelerográfica del Instituto de Ingeniería (IING), Universidad Nacional Autónoma de México (UNAM, National Autonomous University of Mexico), and Centro de Instrumentación y Registros Sísmicos (CIRES). We thank personnel of SSN, IING, and CIRES for station maintenance, data acquisition and distribution. In the estimation of the radiated seismic energy and the source spectra, the data provided by the following network were used: CU (Caribbean Network, doi: 10.7914/SN/CU), G (French Global Network of Seismological Broadband Stations, GEOSCOPE, doi: 10.18715/geoscope.g), II (Global Seismograph Network - IRIS/IDA, doi: 10.7914/SN/II), IU (Global Seismograph Network, GSN - IRIS/USGS, doi: 10.7914/SN/IU), NL (Netherlands Seismic and Acoustic Network, doi: 10.21944/e970fd34-23b9-3411-b366-e4f72877d2c5). The data was accessed through the IRIS DMC. The research was partially supported by UNAM, PAPIIT project IN108221 (S.K.S.). X.P.-C. had a sabbatical fellowship from DGAPA-UNAM and thanks the Seismological Laboratory at Caltech for partial funding for her sabbatical.

References

Abe K. (1981). Magnitude of large shallow earthquakes from 1904 to 1980. *Physics of the Earth and Planetary Interiors*, 27, 72- 92.

Anderson J. G., Bodin P., Brune J.N., Prince J., Singh S.K., Quaas R., Oñate M. (1986). Strong ground motion from the Michoacan, Mexico, earthquake. *Science*, 233, 1043-1049. DOI:10.1126/science.233.4768.1043.

Arroyo D., Garcia D., Ordaz M., Mora M.A., Singh S.K. (2010). Strong ground-motion relations for Mexican interplate earthquakes. *Journal of Seismology*, 14, 769–785. doi:10.1007/s10950-010-9200-0

Arroyo D., Ordaz M., Singh S.K. (2022). Prediction of Fourier amplitude spectrum of ground motion in Mexico City from interplate thrust earthquakes, in preparation

Bandy W., Mortera C., Urrutia J., Hilde, T.W.C. (1995). The subducted Rivera-Cocos Plate boundary: Where is it, what is it, and what is its relationship to the Colima rift?. *Geophysical Research Letters*, 22, 3075-3078.

Boatwright J. (2007). The persistence of directivity in small earthquakes. *Bulletin of the Seismological Society of America*, 97, 1850–1861.

Boatwright J., Choy G.L. (1986). Teleseismic estimates of the energy radiated by shallow earthquakes. *Journal of Geophysical Research*. 91, no. B2, 2095–2112.

Boore D. M., Joyner W. B. (1997). Site amplifications for generic rock sites. . *Bulletin of the Seismological Society of America*, 87, 327–341.

Brune J. N. (1970). Tectonic stress and the spectra of seismic shear waves from earthquakes. *Journal of Geophysical Research*, 75, 4997-5009.

Calderoni G., Rovelli A., Singh S.K. (2013). Stress drop and source scaling of the 2009 April L'Aquila earthquakes. *Geophysical Journal International*, 192, 260–274, doi: 10.1093/gji/ggs011.

Corona-Fernández, R.D., Santoyo, M.A. (2022). Re-examination of the 1928 Parral, Mexico earthquake (M6.3) using a new multiplatform graphical vectorization and correction software for legacy seismic data. *Geoscience Data Journal*. **https://doi.org/10.1002/gdj3.159**

Cosenza-Muralles B., DeMets C., Marquez-Azúa B., Sánchez O., Stock J., Cabral-Cano E., McCaffrey R. (2022). Coseismic and postseismic deformation for the 1995 Colima–Jalisco and 2003 Tecoman thrust earthquakes, Mexico subduction zone, from modelling of GPS data. *Geophysical Journal International*, 228, 2137–2173, **https://doi.org/10.1093/gji/ggab435**

Cosenza-Muralles B., DeMets C., Marquez-Azúa B., Sánchez O., Stock J., Cabral-Cano E., McCaffrey R. (2022). GPS-derived interseismic fault locking along the Jalisco–Colima segment of the Mexico subduction zone. *Geophysical Journal International*, 228, 2174–2197, **https://doi.org/10.1093/gji/ggab436**

Courboulex F., Singh S.K., Pacheco J.F., Ammon C. (1997). The 1995 Colima-Jalisco, Mexico, earthquake (M_w 8): A study of the rupture process. *Geophysical Research Letters*, 34, 1019-1022.

Das S., Henry C. (2003). Spatial relation between main earthquake slip and its aftershock distribution. *Review of Geophysics*, 41 (3), 1013, doi: 10.1029/2003RG000119.

DeMets C., Gordon R.G., Argus D.F. (2010). Geologically current plate motions. *Geophysical Journal International*, 181, 1–80.

Dost B., Haak H.W. (2006). Comparing waveforms by digitization and simulation of waveforms for four Parkfield earthquakes observed in station DBN, The Netherlands. *Bulletin of the Seismological Society of America*, 96, S50–S55, doi: 10.1785/0120050813.

Duputel Z., Rivera L., Kanamori H., Hayes G. (2012). W-phase fast source inversion for moderate to large earthquakes (1990 - 2010). *Geophysical Journal International*, 189(2), 1125-1147.

EERI Preliminary Virtual Reconnaissance Report. (2022). Aquila, Michoacán, Mexico September 19, 2022, M_w 7.6 earthquake. Release date 30 September, 2022, 109 pp.

Hayes G.P., Rivera L., Kanamori H. (2009). Source inversion of the W phase: real-time implementation and extension to low magnitude. *Seismological Research Letters*, 80(5), 817-822.

Hjörleifsdóttir V., Singh S.K., Husker A. (2016). Differences in epicentral location of Mexican earthquakes between local and global catalogs: An update, *Geofísica Internacional*, 55, 79-93.

Hjörleifsdóttir V., Sánchez-Reyes H. S., Ruiz-Angulo A., Ramírez-Herrera M. T., Castillo-Aja R., Singh S. K., Ji C. (2018). Was the 9 October 1995 M_w 8 Jalisco, Mexico, earthquake a near-trench event? *Journal of Gephysical Research: Solid Earth*, 123, 8907-8925. **https://doiorg/10.1029/2017JB014899**

Iglesias, A., Singh, S. K., Castro-Artola, O., Pérez-Campos, X., Corona-Fernández, R. D., Santoyo, M. A., Espíndola V. H., Arroyo D., and Franco, S. I. (2022). A Source Study of the M w 7.0 Acapulco, Mexico, Earthquake of 8 September 2021. *Seismological Research Letters*, 93(6), 3205-3218.

Kanamori H. Anderson D. L. (1975). Theoretical basis of some empirical relations in seismology. *Bulletin of the Seismological Society of America*, 65, 1073- 1095.

Kanamori H., Jennings P. C., Singh S. K., Astiz L. (1993). Estimation of strong ground motions in Mexico City expected for large earthquakes in the Guerrero seismic gap. *Bulletin of the Seismological Society of America*, 93, 811- 829.

Kanamori H., Rivera L. (2008) Source inversion of W phase: speeding tsunami warning. *Geophysical Journal International*. 175, 222-238.

Kelleher J. A., Sykes L.R., Oliver J. (1973). Possible criteria for predicting earthquake locations and their applications to major plate boundaries of the Pacific and Caribbean. *Journal of Geophysical Research*, 78, 2547-2585.

Koketsu K., Miyake H., Guo Y., Kobayashi H., Masuda T., Davuluri S., Bhattarai M., Adhikari L. B., Sapkota S. N. (2016). Widespread ground motion distribution caused by rupture directivity during the 2015 Gorkha, Nepal earthquake. *Scientific Reports*, 6, 28536. **http://doi.org/10.1038/srep28536**

Lay T., Ye L., Koper K.D., Kanamori H. (2017). Assessment of teleseismically-determined source parameters for the April 25, 2015 M_w 7.9 Gorkha, Nepal earthquake and the May 12, 2015 M_w 7.2 aftershock. *Tectonophysics* 714, 4-20, **http://dx.doi.org/10.1016/j.tecto.2016.05.023**

Maubant L., Radiguet M., Pathier E., Doin M. P., Cotte N., Kazachkina E., Kostoglodov V. (2022). Interseismic coupling along the Mexican subduction zone seen by InSAR and GNSS. *Earth and Planetary Science Letters* 586, 117534.

Miranda y Marron M. (1911- 1912). El temblor de 7 de junio de 1911. *Société Scientifique "Antonio Alzate," – Mémoires*, 32, 27-66.

Mendoza C., Martinez-Lopez M.R. (2022). Rapid finite-fault analysis of large Mexico earthquakes using teleseismic P waves. *Journal of Seismology*, 26, 333–342. **https://doi.org/10.1007/s10950-022-1083-y**

Ordaz M., Arboleda J., Singh S. K. (1995). A scheme of random summation of an empirical Green's function to estimate ground motions from future large earthquakes. *Bulletin of the Seismological Society of America*, 85:1635–1647

Pacheco J., Singh S. K., Domínguez J., Hurtado A., Quintanar L., Jiménez Z., Yamamoto J., Gutiérrez C., Santoyo M., Bandy W., Guzmán M., and Kostoglodov V. (1997). The October 9, 1995 Colima-Jalisco, Mexico earthquake (M_w 8): An aftershock study and a comparison of this earthquake with those of 1932. *Geophysical Research Letters* 24, 2223–2226. **https://doi.org/10.1029/97GL02070**

Pérez-Campos X., Beroza G.C. (2001). An apparent mechanism dependence of radiated seismic energy. *Journal of Geophysical Research*, 106, no. B6, 11,127–11,136.

Pérez-Campos X., Singh S.K., Beroza G.C. (2003). Reconciling teleseismic and regional estimates of seismic energy. *Bulletin of the Seismological Society of America*, 93, 2123–2130.

Pérez-Campos X., Espíndola V.H., Pérez J., Estrada J.A., Cárdenas Monroy C., Zanolli B., Bello D., González-López A., González Ávila D., Maldonado R., Montoya-Quintanar E., Vite R., Martínez L.D., Tan Y., Rodríguez Rasilla I., Vela Rosas M. Á., Cruz J.L., Cárdenas A., Navarro Estrada F., Hurtado A., Mendoza Carvajal A.J. (2019). Servicio Sismológico Nacional, México. *Bulletin of the International Seismological Centre*, 53(II), 29–40, **https://doi.org/10.31905/SZ7RYBTM**

Reyes A., Brune J.N., Lomnitz C. (1979). Source mechanism and aftershock study of the Colima, Mexico earthquake of January 30, 1973. *Bulletin of the Seismological Society of America*, 69, 1819–1840.

Santoyo M. A., Mikumo T., Quintanar L. (2006). Faulting process and coseismic stress change during the 30 January, 1973, Colima, Mexico interplate earthquake (M_w=7.6). *Geofísica Internacional*, 45,3, 163-178.

Seo M.-S., Kim W.-Y., Kim Y. (2022). Rupture directivity of the 2021 ML 2.2 Gwangyang, Korea, microearthquake: Toward resolving high-resolution rupture process of a small earthquake, *The Seismic Record* 2(4), 227–236, doi: 10.1785/0320220030.

Singh, S.K., Pacheco, J.F., Alcántara, L., Reyes, G., Ordaz, M., Iglesias, A., Alcocer, S.M., Gutierrez, C. Valdés, C., Kostoglodov, V., Reyes, C., Mikumo, T., Quaas, R., Anderson, J.G. (2003). A Preliminary Report on the Tecomán, Mexico Earthquake of 22 January 2003 (M_w 7.4) and its Effects. *Seismological Research Letters*, 74, 279-289.

Singh S. K., Plata-Martínez R., Pérez-Campos X., Espíndola V.H., Iglesias A., Arroyo D. (2019). Evidence of directivity during the earthquakes of 8 and 10 May 2014 (M_w 6.5, 6.1) in the Guerrero, Mexico seismic gap and some implications. *Journal of Seismology*, 23, 683-697.

Singh S. K., Pérez-Campos X., Ordaz M., Iglesias A., Kostoglodov V. (2020). Scaling of peak ground displacement with seismic moment above the Mexican subduction thrust. *Seismological Research Letters*, 91, 956–966, doi: 10.1785/0220190155.

Singh, S.K., Corona-Fernández, R.D., Santoyo, M., Iglesias, A. (2022). Repeating large earthquakes along the Mexican subduction zone, in preparation.

Singh S. K., Ponce L., Nishenko S.E. (1985). The great Jalisco, Mexico, earthquakes of 1932: Subduction of the Rivera Plate. *Bulletin of the Seismological Society of America*, 75, 1301-1313.

Singh S.K., Lermo J. (1985). Mislocations of Mexican earthquakes as reported in international bulletins. *Geofísica Internacional*, 24, 333-351.

Singh S.K., Suárez G. (1988). Regional variation in the number of aftershocks (mb ≥ 5) of large, subduction-zone earthquakes ($M_w \geq 7.0$). *Bulletin of the Seismological Society of America*, 78, 230-242.

Somerville P. G., Smith N. F., Graves R. W., Abrahamson N. A. (1997). Modification of empirical strong ground motion attenuation relations to include the amplitude and duration effects of rupture directivity. *Seismological Research Letters* 68, 199–222.

UNAM Seismology Group (1986). The September 1985 Michoacan earthquakes: Aftershock distribution and history of rupture. *Geophysical Research Letters*, 13, 573-576.

Wang S.-C., McNally K.C., Geller R.J. (1982). Seismic strain release along the Middle America Trench, Mexico. *Geophysical Research Letters*, 9, 182-185.

Ye L., Kanamori H., Lay T. (2018). Global variations of large megathrust earthquake rupture characteristics, *Science Advances* 4, 1–8. **https://doi.org/10.1126/sciadv.aao4915**

Ye L., Lay T., Kanamori H., Rivera L. (2016). Rupture characteristics of major and great (M_w 7.0) megathrust earthquakes from 1990–2015: I. Source parameter scaling relationships. *Journal of Geophysical Research*, Solid Earth 121, 826–844. **http://dx.doi.org/10.1002/2015JB012426**

Geofísica Internacional (2023) **62-2**: 467 - 485

Evaluación de la vulnerabilidad del acuífero Victoria – Güémez mediante el método DRASTIC

Luis Gerardo Vázquez-Guevara[1], René Ventura-Houle[1*], Glenda Nelly Requena-Lara[1], Elizabeth Andrade-Limas[1], Barbara Azucena Macías Hernández[1]

Resumen

Los estudios sobre la situación del agua en los acuíferos son limitados y para el estado de Tamaulipas son escasos. Por esa razón, el objetivo de este trabajo fue evaluar la vulnerabilidad intrínseca del acuífero Victoria-Güémez, utilizando el método DRASTIC, además de emplear el modelador *WaterYield* de InVEST 3.7, que considera datos biofísicos del suelo y plantas, para estimar con mayor precisión el factor de recarga. Los resultados obtenidos permitieron identificar que la vulnerabilidad más alta del acuífero se presenta en y alrededor de las manchas urbanas de mayor superficie, mientras que la más baja se da en las zonas con alta profundidad del nivel freático y baja permeabilidad en la zona vadosa. Este estudio es el primer paso para generar una herramienta de gestión del agua subterránea en la que se establezcan las líneas de acción para administrar el agua del acuífero que se encuentra con déficit.

Palabras Clave: DRASTIC, agua subterránea, InVEST 3.7, acuífero Victoria-Güémez, Tamaulipas

Abstract

Studies about water in aquifers are limited, and scarce in the state of Tamaulipas. For this reason, the objective of this work was to evaluate the intrinsic vulnerability of the Victoria-Güémez aquifer using the DRASTIC method and the WaterYield modeler of InVEST 3.7, which considers biophysical data of the soil and plants, to estimate with greater precision the factor of recharge. The results obtained made it possible to identify that the highest vulnerability of the aquifer occurs in and around the urban areas with the largest surface area, while the lowest occurs in areas with a high depth of the water table and low permeability in the vadose zone. This study is the first step to generate a groundwater management tool in which the lines of action are established to manage the water of the aquifer that is in deficit.

Keywords: DRASTIC, groundwater, InVEST 3.7, Victoria-Güémez aquifer, Tamaulipas

Introducción

La definición de si un acuífero se considera sobreexplotado o deja de serlo está en función de la relación existente entre la extracción y la recarga, es decir, la cantidad del recurso utilizado y el tiempo que toma en recuperar su nivel (CONAGUA, 2018). Según lo documentado por la Comisión Nacional del Agua (CONAGUA), a partir del 2001, la cantidad de acuíferos sobreexplotados en México osciló anualmente entre 100 y 106. Entre el año 2015 y 2018 la cifra aumentó de 105 a 144, por lo que en tres años hubo un aumento del 37%. Esto debido a que 70 millones de habitantes viven en las regiones hidrológico-administrativas en las que se genera un 60% del PIB de México, lo que coincide con la concentración demográfica, que provoca escasez de recursos y su sobreexplotación (Caballero, 2020). El crecimiento urbano implica el aumento de zonas más impermeables, por lo que se reduce la infiltración del agua, se elimina la vegetación, hay cambios en la topografía del terreno y el uso del suelo (Ríos-Sánchez *et al.*, 2020).

La única información publicada sobre acuíferos en Tamaulipas se refiere a la disponibilidad media anual de agua en los acuíferos que realiza la CONAGUA en el Diario Oficial de la Federación (DOF). Esto se realiza conforme a los lineamientos que considera la Norma Oficial Mexicana NOM-011-CONAGUA-2015 "conservación del recurso agua que establece las especificaciones y el método para determinar la disponibilidad media anual de las aguas nacionales". Dicha información consiste en una lista de los 653 acuíferos de México, con su condición de déficit o disponibilidad, donde 205 se encuentran catalogados como "sin disponibilidad", déficit (CONAGUA, 2017).

Received: July 4, 2021; Accepted: December 13, 2022; Published on-line: April 1, 2023.

Editorial responsibility: María Aurora Armienta

* Corresponding author: René Ventura-Houle, rventura@docentes.uat.edu.mx y reneventura.houle@gmail.com
[1] Facultad de Ingeniería y Ciencias. Universidad Autónoma de Tamaulipas. Centro Universitario, CP. 87120, Cd. Victoria, Tamaulipas.

Vázquez-Guevara, L, Ventura-Houle, R, Requena-Lara, G, Andrade-Limas, E, Macías-Hernández, B
https://doi.org/10.22201/igeof.2954436xe.2023.62.2.1589

Tamaulipas cuenta con catorce acuíferos, tres de ellos con déficit: Hidalgo – Villagrán, Márgenes del Río Purificación y Victoria – Güémez (CONAGUA, 2018b). Para el acuífero Victoria – Güémez, el último estudio de disponibilidad media anual de agua subterránea (DMA), expone que presenta un déficit de 28.768,000 m^3 anuales; por tal motivo, no existe volumen disponible para otorgar nuevas concesiones para los usuarios (CONAGUA, 2020).

Otra información importante para una adecuada gestión de acuíferos, como los relativos a la vulnerabilidad y disponibilidad de agua subterránea relacionados son limitados, de acuerdo con Mendieta-Mendoza *et al.* (2021). Para el caso de México, dichos estudios son escasos y en Tamaulipas se carece de datos sobre la evaluación de la situación o la vulnerabilidad del agua subterránea en los acuíferos.

La vulnerabilidad del agua subterránea se refiere a las propiedades intrínsecas del suelo, subsuelo y del acuífero que sirven de protección natural de las aguas subterráneas (Aguilar *et al.*, 2013). Esta variable determina la sensibilidad de un acuífero ante efectos de los contaminantes y es relativa, no medible y adimensional; se le considera intrínseca cuando la evaluación se realiza incluyendo los factores hidrogeológicos del acuífero y específica si contempla factores externos como el clima o las características del contaminante (Foster, 1987).

La generación de mapas de vulnerabilidad de las aguas subterráneas funciona como herramienta esencial en la protección y gestión de estas (Thapa *et al.*, 2018). Actualmente éstos se pueden producir utilizando los sistemas de información geográfica (SIG), ya que existen diversos métodos que evalúan la vulnerabilidad del agua subterránea (González *et al.*, 2018). Uno de estos métodos más frecuentemente utilizados para su evaluación es DRASTIC, (Fijani *et al.*, 2013), que mediante su uso, se realiza una clasificación y ponderación de los factores geológicos e hidrogeológicos de los acuíferos, los cuales afectan el movimiento de contaminantes a través del suelo hasta entrar en contacto con el agua subterránea. Estos factores dan origen al nombre del método de Aller *et al.* (1987) y son, por sus siglas en inglés:

D (profundidad del nivel piezométrico), R (recarga), A (litología del acuífero), S (naturaleza del suelo), T (pendiente del terreno), I (naturaleza de la zona no saturada) y C (permeabilidad).

Mediante el desarrollo de los SIG se han propuesto modelos espaciales que simulan procesos hidrológicos. El modelador de valoración integrada de los servicios y las compensaciones de los ecosistemas (InVEST, por sus siglas en inglés), es ampliamente utilizado y resulta adecuado especialmente para establecer diversos servicios ambientales (ecosistémicos) como rendimiento de agua, retención de nutrientes, retención de sedimentos en lugares donde no existen cantidades de datos suficientes (Yang *et al.*, 2020). De acuerdo con Mendoza *et al.*, (2011) el modelo *Water Yield del InVEST*, se utiliza como factor rector principal para modelar servicios ambientales como el rendimiento hídrico o aporte de agua, así como la carga y retención de contaminantes y sedimentos.

Por lo anterior, el objetivo principal de este trabajo fue evaluar la vulnerabilidad del acuífero Victoria-Güémez, mediante el método DRASTIC a través de un Sistema de Información Geográfica.

Área de estudio

El acuífero Victoria – Güémez pertenece a la Cuenca IX "Golfo Norte" y se sitúa en la parte centro-occidente del estado de Tamaulipas. Cubre una superficie de 2,080 km^2 y presenta su zona de influencia en los municipios de Victoria, Güémez, Padilla y una porción del municipio de Hidalgo, Tamaulipas (Figura 1). Las poblaciones más importantes por su número y actividad económica son Ciudad Victoria, Güémez y Santa Engracia, con una población de casi 365 mil habitantes en 2020 (INEGI, 2020), con 96% de ellos residiendo en la primera, que es la capital estatal; en ellas el rápido crecimiento de población, el aumento de servicios urbanos y la agricultura, han elevado la competencia por el uso del agua subterránea, generando un incremento en la extracción del recurso (CONAGUA, 2017).

Para este acuífero, el volumen de extracción de aguas subterráneas es de 107'968,000 m^3 anuales, que reporta el Registro Público de Derechos de Agua (REPDA) de la Subdirección General de Administración del Agua (al 20 de febrero del 2020). No se registró un volumen disponible para otorgar nuevas concesiones, pues el déficit del acuífero Victoria - Güémez es de 28'768,000 m^3 anuales, que se están extrayendo a costa del "almacenamiento "no renovable" del acuífero (CONAGUA, 2017).

El área de estudio se localiza en las inmediaciones del conjunto montañoso que constituye el cinturón de pliegues y cabalgaduras de la Sierra Madre Oriental (SMO), conformado principalmente por rocas sedimentarias de origen marino, cuya edad va del Cretácico hasta el Mioceno. Dichas rocas son de composición calcárea, arcillosa y arcillo-arenosa dispuesta en estratos de potencia variable, cuya facie mas densa y resistente son las calizas (Rubio *et al.*, 2011), que dan lugar a una estructura kárstica altamente fracturada, rocas de color crema, gris claro, gris obscuro y gris verdoso que suelen están intercaladas con lutitas (Carrillo-Bravo 1961; Eguiluz *et al.*, 2000). Depósitos sedimentarios mas recientes sobreyacen a las predominantes calizas, los cuales son conglomerados del plioceno, además de aluviones y suelos residuales del cuaternario (Camacho 1987).

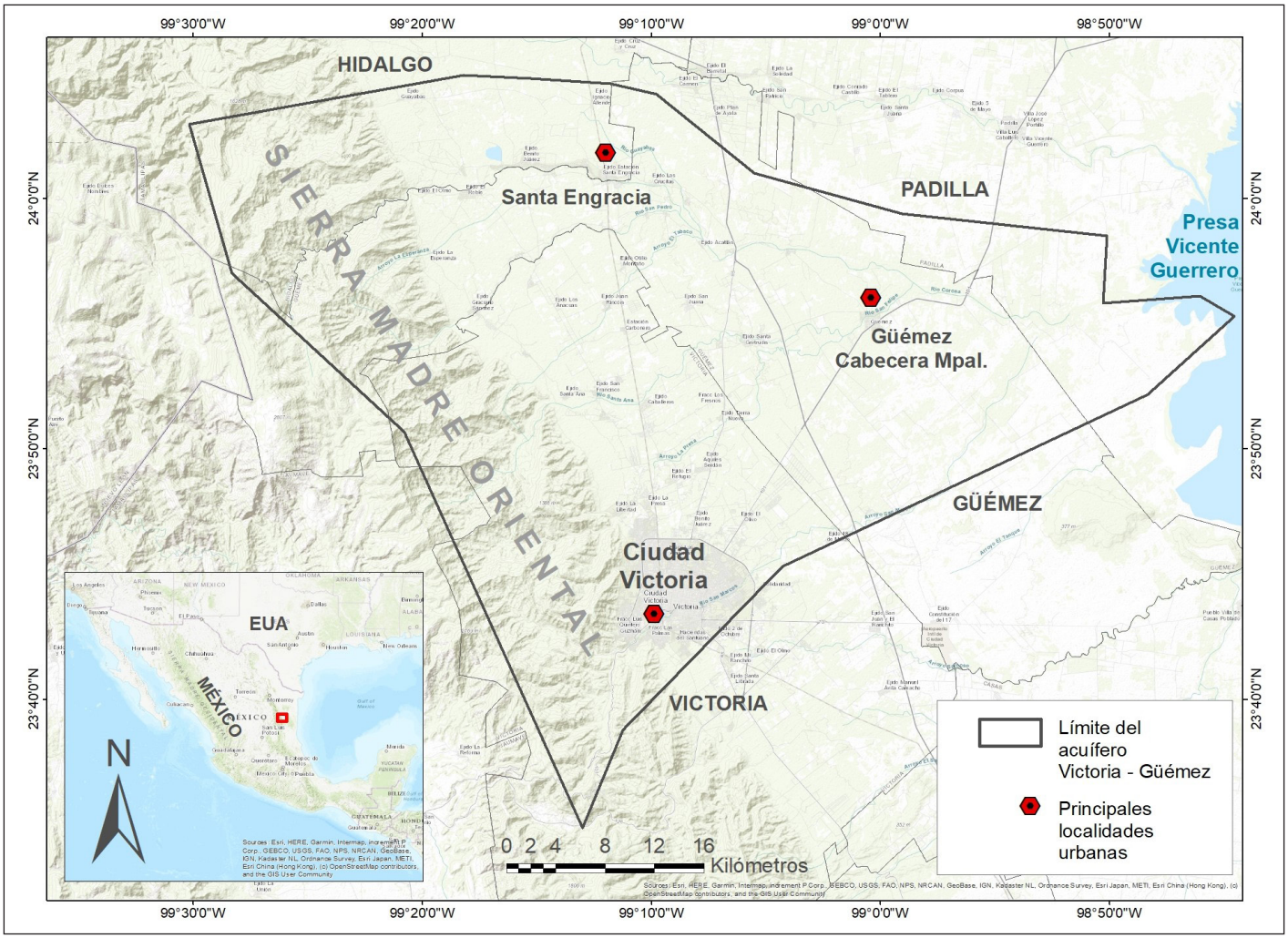

Figura 1. Localización geográfica del área de estudio.

Dichas estructuras sobreyasen a un basamento que es un complejo metamórfico de edad precámbrica, rocas metamórficas que son las estructuras mas antiguas de la región, gneis azul-verdoso poco fracturados, aflorados en la zona denominada anticlinorio huizachal-peregrina. Un proceso volcánico da lugar a las formaciones rocosas mas recientes en la región, que son una serie de rocas ígneas intrusivas, hipabisales y extrusivas que irrumpen en los materiales sedimentarios ya sea de manera intrusiva o cubriéndolos en algunas zonas puntuales (Carrillo-Bravo 1961)

Las unidades hidrogeológicas que afloran en el área del acuífero corresponden a depósitos sedimentarios de diferentes edades, víctimas de diferentes procesos diagenéticos con los que se formaron las rocas localizadas actualmente en la zona (CONAGUA, 2017).

Metodología

El método DRASTIC combina factores geológicos e hidrogeológicos y selecciona siete indicadores representativos para evaluar la vulnerabilidad del agua subterránea con aspectos cualitativos y cuantitativos (Jia *et al.*, 2019): profundidad del agua, recarga neta, medios acuíferos, medios del suelo, topografía, impacto en los medios de la zona vadosa y conductividad hidráulica (Aller *et al.*, 1987). Para cuantificar cada uno de los factores DRASTIC se aplicó un sistema de evaluación en el que se establecieron tres parámetros significativos: pesos, rangos y valores. La determinación de los índices de vulnerabilidad consistió en multiplicar cada uno de los parámetros (r), por el peso (w) asignado por el método y se suma el total. El peso para cada uno de los factores se establece de acuerdo con su importancia y aplicabilidad (Tabla 1).

Tabla 1. Pesos para cada variable del método DRASTIC.

	Tipo de variable						
	Dw	Rw	Aw	Sw	Tw	Iw	Cw
Pesos	5	4	3	2	1	5	3

Dw= peso de profundidad, Rw= peso de recarga, Aw= peso de medios acuíferos, Sw= peso de medios del suelo, Tw= peso de topografía, Iw= peso de zona vadosa, Cw= peso de conductividad

Posteriormente se realizó una clasificación a cada factor con los nuevos valores y se aplicó la herramienta "álgebra de mapas" mediante el *software* ArcGIS 10.7.1, en donde se sumaron los parámetros ponderados, de acuerdo con la Ecuación 1, obteniendo como resultado final el índice de vulnerabilidad relativo (Figura 2).
Ecuación 1:

$$IndxV = DrDw + RrRw + ArAw + SrSw + TrTw + IrIw + CrCw$$

Donde:
IndxV = Índice de vulnerabilidad
DrDw = profundidad del agua
RrRw = recarga neta
ArAw = medios acuíferos
SrSw = medios del suelo
TrTw = topografía
IrIw = impacto en los medios de la zona vadosa
CrCw = conductividad hidráulica

El resultado final es un índice relativo en forma numérica, el cual fue clasificado en la Tabla 2, con niveles para expresarlo en forma categórica, de acuerdo con Aller *et al.*, 1987, que se encuentran en la tabla siguiente.

A continuación, se describe cada factor y la forma en que se integró como modelo espacial en el SIG. En primera instancia, el territorio del acuífero se obtuvo del mapa digital de disponibilidad de agua por acuífero (CONAGUA, 2017), con el cual se procesaron el resto de las variables. La cartografía digital obtenida de CONABIO-INIFAB, del SGM, de INEGI y de CNA se encuentra a escala 1:250,000; mientras que la de CONABIO (1998) se obtuvo a 1:1'000,000. La información en formato ráster se procesó con un tamaño de celda de 100×100 metros.

1. Profundidad del agua (DrDw)

La profundidad del agua subterránea (Figura 6) se clasificó en siete rangos que van de 1 a 30 m de profundidad (Tabla 3). Los pesos asignados variaron de 1 a 10 (Aller *et al.*,

Tabla 2. Categorización de los valores numéricos del índice de vulnerabilidad (Aller *et al.*, 1987).

Índice de vulnerabilidad (IndxV)	**Clasificación Vulnerabilidad**
< 79	Muy baja
80 - 99	Baja
100 - 119	Baja - Moderada
120 - 139	Moderada
140 - 159	Moderada Alta
160 - 179	Alta
180 - 199	Muy Alta
200 >	Extremadamente Alta

Tabla 3. Valores DRASTIC para los rangos de profundidad al nivel freático.

Profundidad al nivel freático (m)	
Rango	**Clasificación**
0-1	10
1-3	9
4-9	7
9-15	5
15-22	3
22-30	2
>30	1

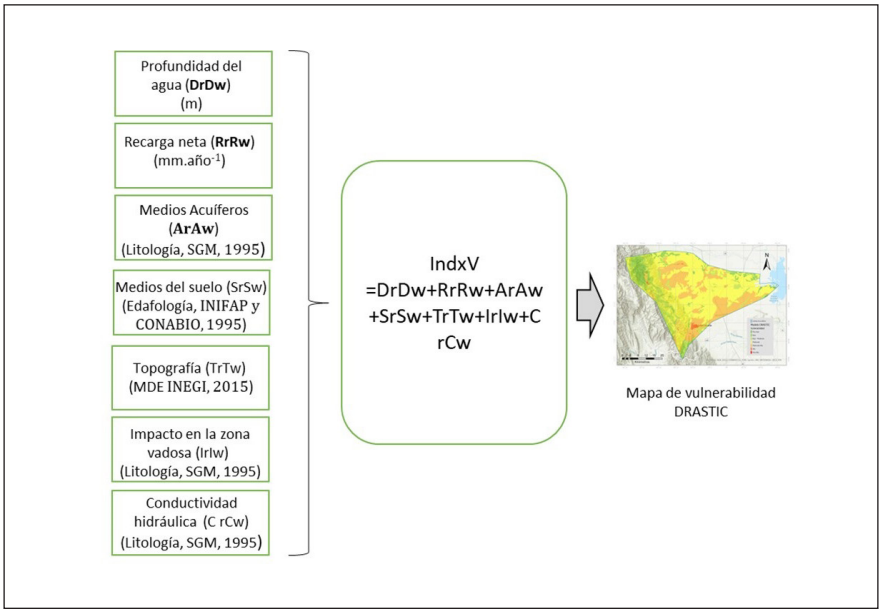

Figura 2. Esquema conceptual del desarrollo del modelo DRASTIC.

1987) indicando que, entre mayor sea el peso, mayor es la vulnerabilidad (Abunada *et al.*, 2021).

Los niveles de profundidad proporcionados por el Comité Técnico de Aguas Subterráneas (COTAS) fueron de los períodos de canícula 2018, invierno 2018 y canícula 2019. Por ello se tomó el promedio de los tres valores para cada uno de los pozos y se integraron en una base de datos para procesarla en el *software* ArcGIS 10.7.1.

2. Recarga neta (RrRw)

La recarga neta se mide en mm año^{-1}, y es definida por Abunada *et al.* (2021) como la cantidad de agua infiltrada desde la capa superior del suelo hasta el nivel freático. El método DRASTIC le asigna cinco valores a rangos de recarga, establecidos en la Tabla 4.

El factor de recarga es un indicador del movimiento de un contaminante hasta el agua subterránea mediante procesos de lixiviación. Actualmente, la generación de nuevos valores en el factor de recarga es una mejora en la evaluación de la vulnerabilidad, debido a que están sujetos a variaciones por los cambios de estación que dependen de las condiciones climáticas, así como la hidrología superficial, lo que dificulta la medición de la recarga de manera efectiva (Abunada *et al.*, 2021).

Tabla 4. Valores de clasificación para los rangos de la recarga neta otorgados por el método DRASTIC.

Recarga Neta (mm)	
Rango	**Clasificación**
0-50	1
50-100	3
100-180	6
180-255	8
>255	9

Se utilizó el *software* InVEST 3.8.9 del proyecto *The Natural Capital* para estimar los valores del factor de recarga, a través del modelador WaterYield. Este modelador parte de la hipótesis de Milly (Mendoza *et al.*, 2011), donde una estimación aproximada de la provisión de agua en un terreno puede obtenerse a partir de la interacción local entre las fluctuaciones de la precipitación y la evapotranspiración potencial (ETP), con las propiedades de almacenamiento del suelo. Esta diferencia es calculada como la provisión o aporte de agua (*Water Yield*) en cada píxel del área de estudio, indexándolo como x= 1,2,3… X, para cada uso de suelo y cobertura vegetal (LULC), a través de la Ecuación 2:
Ecuación 2:

$$Y_{xj} = \sum \left(1 - \frac{AET_{xj}}{P_{xj}}\right) \cdot P_{xj} \cdot A_{xj}$$

Donde:
Y_{xj}= Aporte de agua del píxel x en el LULC j
AET_{xj} = ETP real anualizada del píxel x que tiene un LULC j.
P_{xj} = precipitación anual en el píxel x, con un LULC j.
A_{xj} = área del píxel x en el LULC j.

La porción del balance hídrico respectiva a la ETP dada por AET_{xj}/P_{xj} es parte de la curva de Budyko, de la Ecuación 3 (Mendoza *et al.*, 2011):
Ecuación 3:

$$\frac{AET_{xj}}{P_{xj}} = \frac{1 + \omega_{xj} R_{xj}}{1 + \omega_{xj} R_{xj} + \frac{1}{R_{xj}}}$$

Donde:
R_{xj} = proporción de ETP potencial respecto a la a precipitación, o índice de aridez de Budyko (Mendoza *et al.*, 2011) en el píxel x del LULC j.
ω_{xj} = Proporción del Agua Almacenada Accesible para las Plantas (PAWC) respecto a la precipitación anual esperada.
P_{xj} = precipitación anual en el píxel x, con un LULC j.

La fracción del contenido de agua en el suelo disponible para las plantas (PAWC, por sus siglas en inglés) (Ecuación 4) caracteriza el balance de agua en las comunidades vegetales, dentro de unas condiciones prevalecientes de clima y de suelo (Mendoza *et al.*, 2011):
Ecuación 4:

$$\omega_{xj} = Z \frac{AWC_x}{P_{xj}}$$

Donde:
AWC_x = volumen (en mm) del agua contenida en el suelo que está disponible para las plantas.
Z = parámetro usado como constante de calibración, que se aplica a cada subcuenca.
P_{xj} = precipitación anual en el píxel x, con un LULC j.

Se generó el mapa de precipitación promedio anual (Figura 3), a partir de 124 estaciones climatológicas de ERIC (Extractor Rápido de Información Climatológica, de CONABIO-IMTA, 2001) que cubren los alrededores de la cuenca, en los estados de Tamaulipas y Nuevo León. A dichas estaciones se les asignaron los valores de las Normales Climatológicas del Servicio Meteorológico Nacional, que contempla un análisis de 1970 a 2000.

Por otra parte, la evapotranspiración promedio anual (Figura 4), se descargó en formato *grid* para ESRI, del CGIAR-CSI (*Consortium for Spatial Information*), de ETP promedio anual 1950-2000, producido por Trabucco & Zomer (2009). La profundidad del suelo se generó al asignar el atributo de profundidad, de acuerdo con las características de los perfiles de suelo, realizados en campo por la UAT

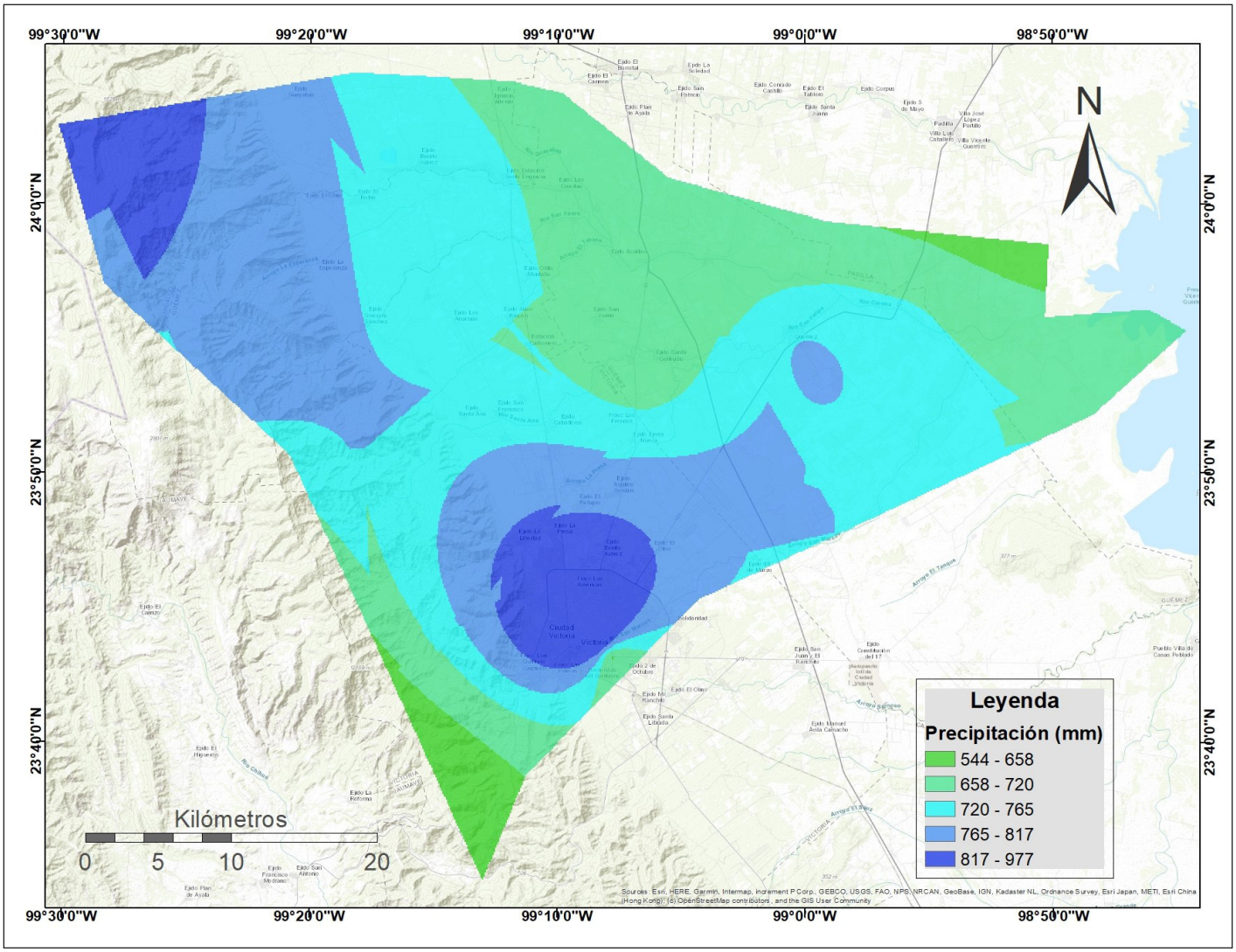

Figura 3. Precipitación promedio anual.

(2001) a la cartografía digital de edafología del INIFAP y CONABIO (1995), clasificado por tipo de suelo. La fracción del contenido de agua en el suelo disponible para las plantas (PAWC, por sus siglas en inglés) se obtuvo, como sugiere el manual de InVEST (Sharp *et al.*, 2020) mediante el uso del *software* SPAW 6.02.75 (Saxton, 2005), para análisis del agua del suelo. Se ingresaron los datos de los perfiles de la UAT (2001) respectivos a los contenidos de arcilla, arena, materia orgánica, salinidad, grava y compactación del perfil representativo de cada tipo de suelo. En algunos casos no se reportaban los contenidos de arena y arcilla como porcentaje en los perfiles, por lo que se ingresaron los que devolvió el programa al ubicar el punto medio en la casilla del triángulo de textura.

Con esos datos, se obtuvo el contenido de agua en el suelo disponible para las plantas (PAWC, por sus siglas en inglés). La fracción se obtiene dividiendo la cantidad de

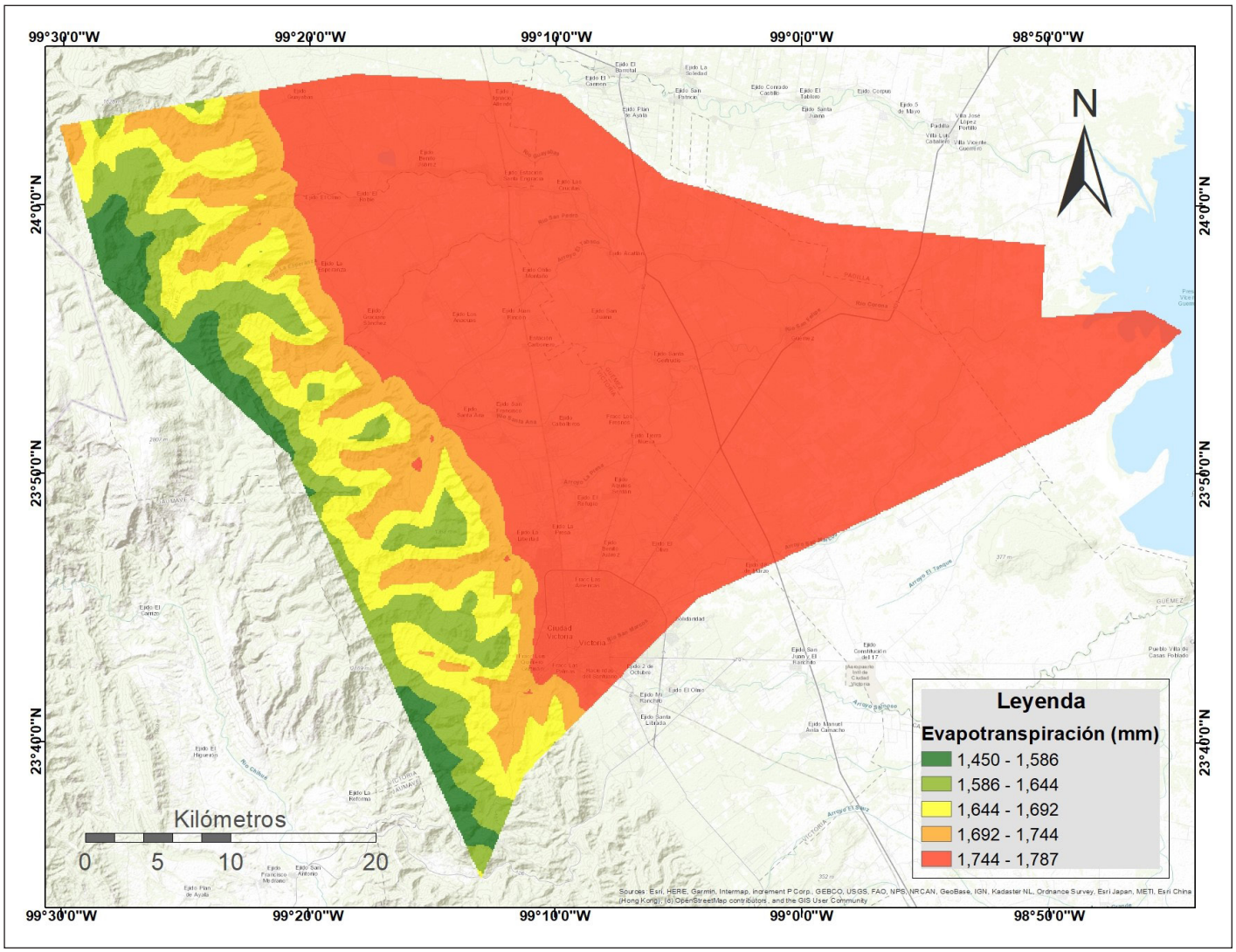

Figura 4. Evapotranspiración promedio anual con datos de Trabucco & Zomer (2009).

Tabla 5. Datos de profundidad del suelo (en mm, excepto PAWC, es adimensional)

Tipo de suelo	PRF	AW	PAWC	PRFS	PRFR
Cambisol-Cálcico	300	9.3	0.01516	1140	3420
Chernozem-Cálcico	850	8.6	0.00946	1250	3750
Litosol	300	19	0.06333	300	300
Luvisol-Vértico	800	0.2	0.01012	800	800
Regosol-Calcárico	1150	10.8	0.00939	1150	1150
Regosol-Eútrico	800	16.4	0.01632	3650	3650
Rendzina	1040	8.1	0.00779	1040	1040
Vertisol-Pélico	475	9.7	0.0218	1605	1605
Xerosol-Lúvico	360	10	0.4101	360	360

PRF= profundidad, AW= disponibilidad de agua en el perfil, PAWC= fracción del contenido de agua en el suelo disponible para las plantas, PRFS= profundidad total del suelo, PRFR= profundidad de raíces.

Tabla 6. Tabla biofísica de profundidad de raíces y coeficiente de ETP para cada tipo de vegetación y uso de suelo.

Tipo de uso de suelo y cobertura vegetal	Profundidad de las raíces (mm)	Coeficiente de evapotranspiración (ETK)
ARRE	210	500
ATCPS	7000	750
ATCA	210	500
AH	0	1
BE	7000	1000
BEVSAH	7000	1000
BPE	7000	1000
BPEVS	7000	1000
BMM	7000	1000
BMVS	7000	1000
CA	0	1000
MET	3700	750
MS	5100	1000
MSVS	5100	1000
MIH	7000	750
MIHVS	5100	750
PC	260	750
PI	260	250
SBCS	3700	1000
SBE	3700	750
SBEVS	15000	1000

ARRE= agricultura de riego (incluye riego eventual), ATCPS= agricultura de temporal con cultivos permanentes y semipermanentes, ATCA= agricultura de temporal con cultivos anuales, AH= asentamiento humano, BE= bosque de encino, BEVSAH= bosque de encino con vegetación secundaria arbustiva y herbácea, BPE= bosque de pino-encino, BPEVS= bosque de pino-encino con vegetación secundaria, BMM= bosque mesófilo de montaña, BMVS= bosque mesófilo de montaña con vegetación arbustiva y herbácea, CA= cuerpo de agua, MET= matorral espinoso tamaulipeco, MS= matorral submontano, MSVS= matorral submontano con vegetación secundaria, MIH= mezquital con huizachal, MIHVS= mezquital con huizachal y vegetación secundaria, PC= pastizal cultivado, PI= pastizal inducido, SBCS= selva baja caducifolia y subcaducifolia, SBE= selva baja espinosa, SBEVS= selva baja espinosa con vegetación secundaria.

agua disponible entre la profundidad del suelo. El PAWC se agregó como atributo al mapa del tipo de suelo. La Tabla 5 muestra los datos por tipo de suelo en los perfiles estudiados por la UAT (2001).

Se utilizaron también la cartografía digital de cuencas (CNA, 1998) y subcuencas hidrológicas (CONABIO, 1998) del acuífero así como el mapa digital de Uso de Suelo y Cobertura Vegetal, serie V (INEGI, 2013); a este último se le asignó a cada una de sus clases el atributo de profundidad de raíces, como se muestra en la Tabla 6.

Por último, el modelador requirió el valor de la constante de Zhang, que varía de 1 a 30, de acuerdo con la distribución estacional de la precipitación. Si las lluvias se producen principalmente en los meses de invierno, los valores de Zhang deben estar cerca de 10; si hay más lluvias durante meses de verano o se propaga uniformemente durante el año, los valores de Zhang deben estar más cerca de 1 (Zhang *et al.*, 2004). Para la zona de estudio se utilizó una constante de 12. Una vez calculada la provisión de agua de un terreno a través de InVEST, se obtuvo el mapa de recarga neta en mm año^{-1} de la zona de estudio.

3. Medios acuíferos (ArAw)

Se refiere como medios acuíferos a la formación consolidada, así como a rocas y guijarros que no se encuentran consolidados en los que está contenida el agua; incluye además poros y fracturas (Bera *et al.*, 2021). Dicha capa se derivó del mapa geológico de México (SGM, 1995) y se clasificó el tipo de material existente de acuerdo con los siguientes valores del método DRASTIC (Tabla 7).

Tabla 7. Valores del parámetro de Medios Acuíferos del modelo DRASTIC

Medios Acuíferos		
Rango	**Clasificación**	**Clasificación típica**
Esquisto masivo	1-3	2
Metamórfico / ígneo	2-5	3
Meteorizado metamórfico / ígneo	3-5	4
Arenisca fina, caliza, secuencias de lutitas	5-9	6
Arenisca masiva	4-9	6
Caliza masiva	4-9	6
Arena y grava	6-9	8
Basalto	2-10	9
Caliza kárstica	9-10	10

4. Medios del suelo (SrSw)

Los medios del suelo se refieren a la parte superior de la zona vadosa en la que se encuentran las actividades biológicas

activas; éstos controlan la permanencia de los contaminantes, además de la recarga en el área (Bera *et al.*, 2021). Para ingresar este indicador, se utilizó el mapa de edafología del INIFAP y CONABIO (1995), donde el tipo de suelo se clasificó, utilizando la información de los perfiles del suelo realizados por la UAT (2001). Los valores DRASTIC para este parámetro se muestran en Tabla 8.

Tabla 8. Valores del parámetro para medios de suelo para le modelo DRASTIC

Medios de suelo	
Rango	**Clasificación**
Delgado o ausente	10
Grava	10
Arena	9
Arcilla encogida y / o agregada	7
Franco arenosa	6
Franco	5
Franco limoso	4
Franco arcilloso	3
Arcilla no encogida y no agregada	1

5. Topografía (TrTw)

La topografía en este proceso indica la pendiente en la superficie de un terreno. Cuanto ésta es mayor, la tasa de infiltración es menor, por lo que las posibilidades de que los contaminantes se filtren hacia abajo y son menores (Bera *et al.*, 2021). del Modelo Digital de Elevación descargado del Continuo de Elevaciones Mexicano (INEGI, 2015), se derivó, con un tamaño de píxel de 90 por 90 m. Los rangos se clasificaron de acuerdo con el porcentaje de pendiente Tabla 9.

Tabla 9. Valores del parámetro de pendiente para le modelo DRASTIC

Topografía (% de pendiente)	
Rango	**Clasificación**
0-2	10
2-6	9
6-12	5
12-18	3
>18	1

6. Impacto en los medios de la zona vadosa (IrIw)

La zona vadosa se define como la zona no saturada entre la capa superior del suelo y el nivel freático. Mientras mayor es la capacidad de atenuación de la zona vadosa, el área será menos vulnerable (Abunada *et al.*, 2021). El mapa de la zona vadosa, se obtuvo del mapa geológico del SGM (1995) y clasificando los rangos de acuerdo con el grado de vulnerabilidad del material geológico (Tabla 10).

Tabla 10. Valores del parámetro para impacto en la zona vadosa según los materiales geológicos para le modelo DRASTIC

Impacto de la zona vadosa		
Rango	**Clasificación**	**Clasificación típica**
Limo/Arcilla	1-2	1
Esquisto	2-5	3
Caliza	2-7	6
Arenisca	4-8	6
Caliza, arenisca, lutita	4-8	6
Arena y grava con limo y arcilla significativos	4-8	6
Metamórfico / Ígneo	2-8	4
Arena y grava	6-9	8
Basalto	2-10	9
Caliza kárstica	8-10	10

7. Conductividad hidráulica (CrCw)

La conductividad hidráulica de un acuífero se refiere a la capacidad que tiene para transmitir agua mediante diversos gradientes hidráulicos, por lo que influye en la tasa del movimiento de un contaminante dentro del acuífero (Abunada *et al.*, 2021). En este trabajo, se derivó del mapa geológico de México (SGM, 1995), y los valores de conductividad se establecieron de acuerdo con el material geológico clasificado en función de la distancia diaria (m día-1) que tarda en recorrer los distintos poros en el subsuelo por los valores calculados por Freeze and Cherry,1979 (Tabla 11).

Tabla 11. Valores del parámetro conductividad hidráulica para el modelo DRASTIC (Freeze and Cherry,1979).

Rango (m^3/día)	**Litología asociada**	**Clasificación**
8-12	Esquisto	2
12-18	Gneis	3
18-22	Serpentinita	4
22 - 28	Arenisca-Conglomerado	6
22 - 28	Caliza	6
22 - 28	Caliza-Lutita	6
22 - 28	Lutita	6
22 - 28	Lutita-Arenisca	6
28-37	Conglomerado	8
8-18	Aluvial	9
59-90	Diorita	10
0-4	Sin datos	N.A.

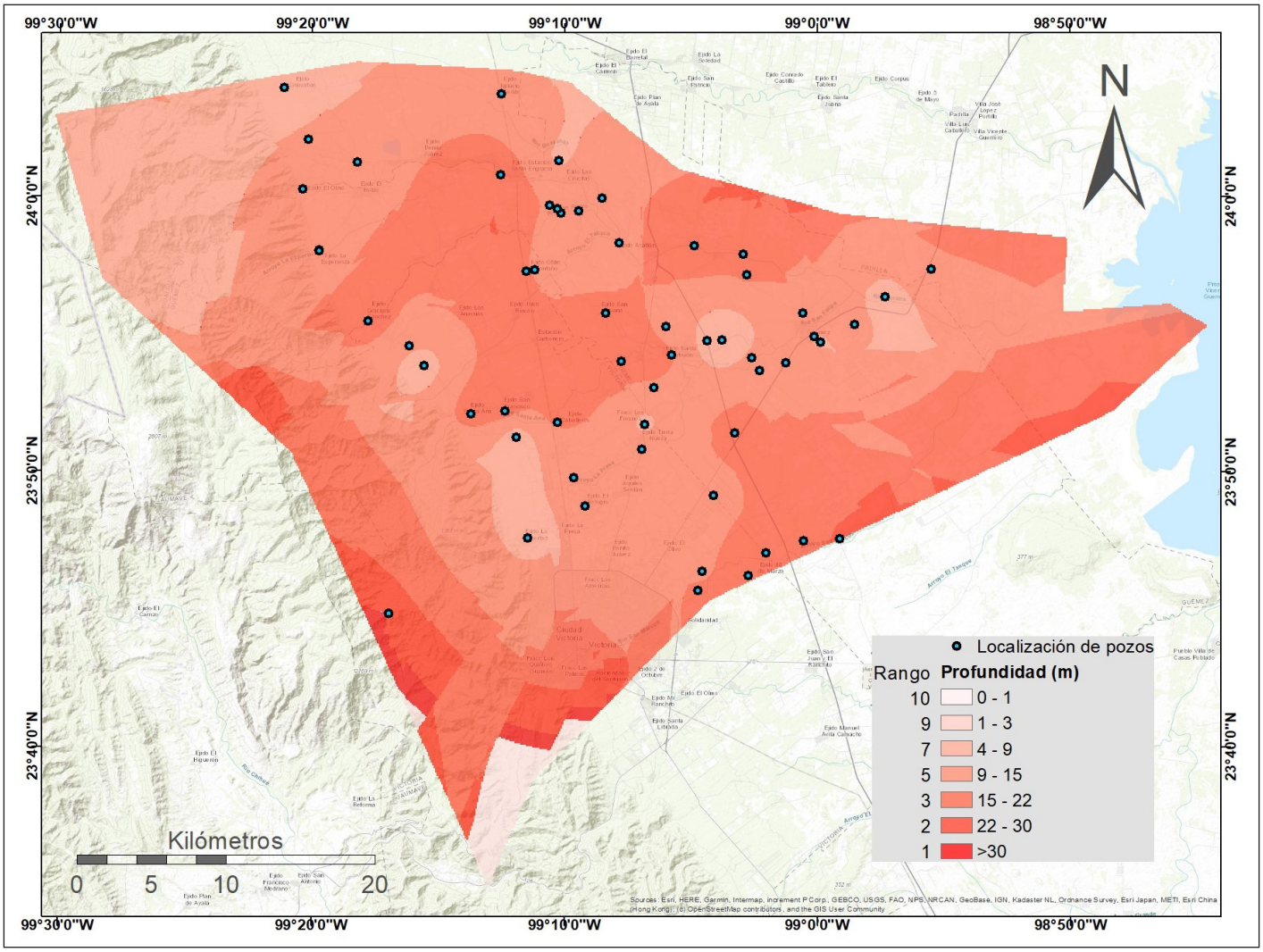

Figura 5. Profundidad del agua subterránea del acuífero Victoria-Güémez.

Resultados y discusión

1. Profundidad del agua

Los pozos de agua en la parte suroeste y sureste del área de estudio cuentan con una mayor profundidad (>30 m), lo que genera una protección al agua subterránea. Por el contrario, en la parte central del acuífero y coincidiendo con la mancha urbana de Ciudad Victoria (Figura 5), se observaron rangos de profundidad de 1 a 9 m. Esto representa una vulnerabilidad alta debido a la corta distancia por la que un contaminante puede entrar en contacto con el agua.

Las zonas donde el nivel freático se encuentra próximo a la superficie (menos de tres metros), indican una alta vulnerabilidad, de acuerdo con lo reportado Pacheco *et al.* (2018), pero en el área de estudio solo se reportan valores mayores a 4. Los acuíferos someros representan una vulnerabilidad a la degradación por concentración de componentes de interés sanitario y ambiental, como el nitrato, el nitrógeno amoniacal, derivados del petróleo, y de actividades de metalurgia, en general. Pathak y Bhandary (2020) resaltan la importan-

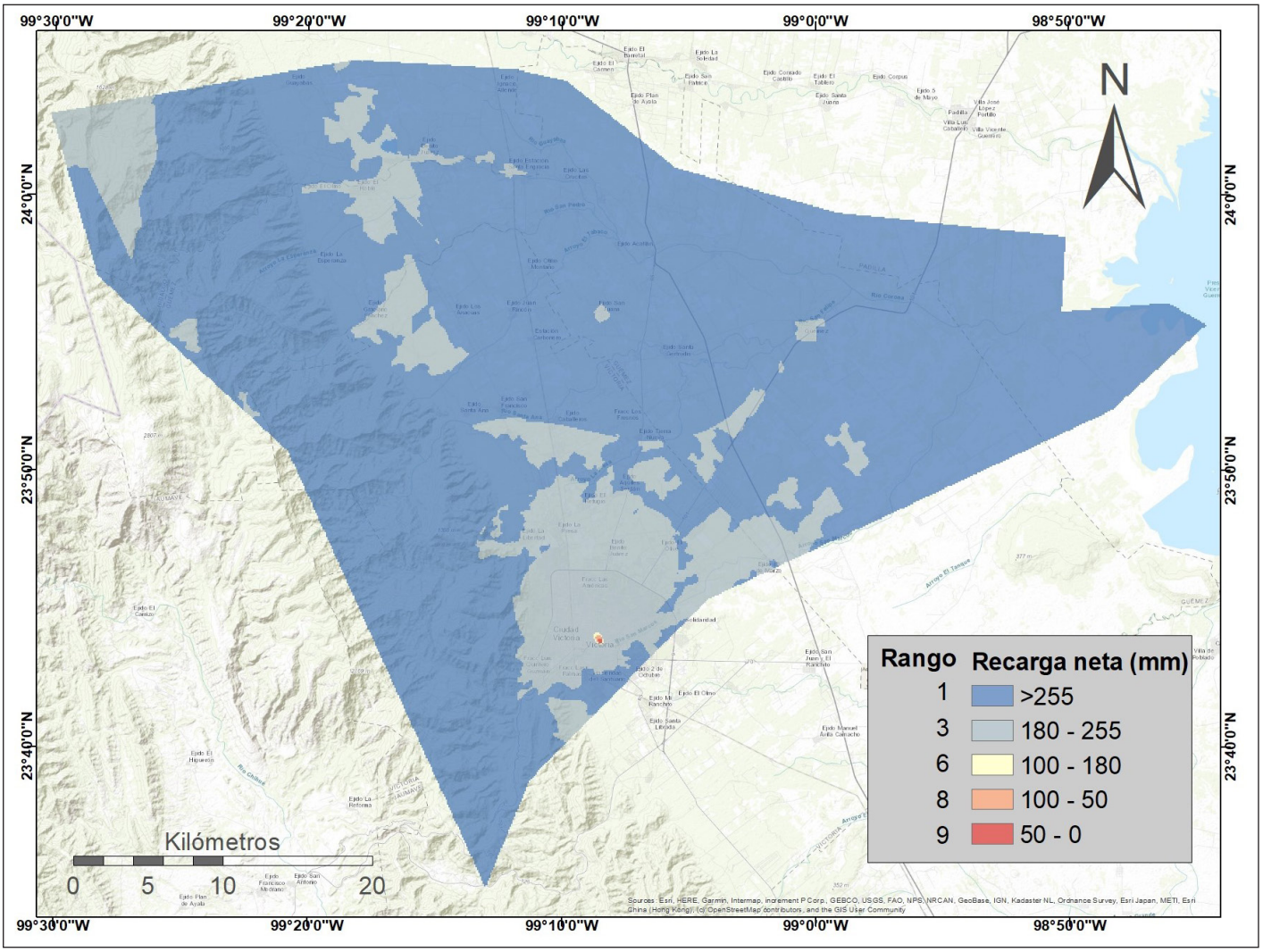

Figura 6. Distribución de la de recarga neta en el acuífero.

cia de la proximidad del manto freático a la superficie y su vulnerabilidad a la contaminación.

2. Recarga neta del agua subterránea

Se determinó que la recarga neta de agua subterránea en la mayor parte de la zona de estudio es de 255 mm año^{-1}. Su distribución espacial concuerda con el patrón del tipo de vegetación, ya que al oeste del acuífero se encuentra la Sierra Madre Oriental (SMO) donde predomina el bosque de pino encino y bosque mesófilo de montaña (Figura 6). Esto debido a que las raíces de ese tipo de vegetación suelen ser más profundas, lo que permite una mayor recarga de agua. Resultados similares fueron reportados por Sun *et al.* (2018) quienes encontraron mayor infiltración de agua en el bosque a diferencia de las zonas con pastizales; mencionan que eso se puede atribuir al hecho de que los suelos presentan una distribución más extensa de raíces debajo de las plantas leñosas.

En las zonas que pertenecen a las manchas urbanas de Ciudad Victoria, Güémez y Santa Engracia los valores os-

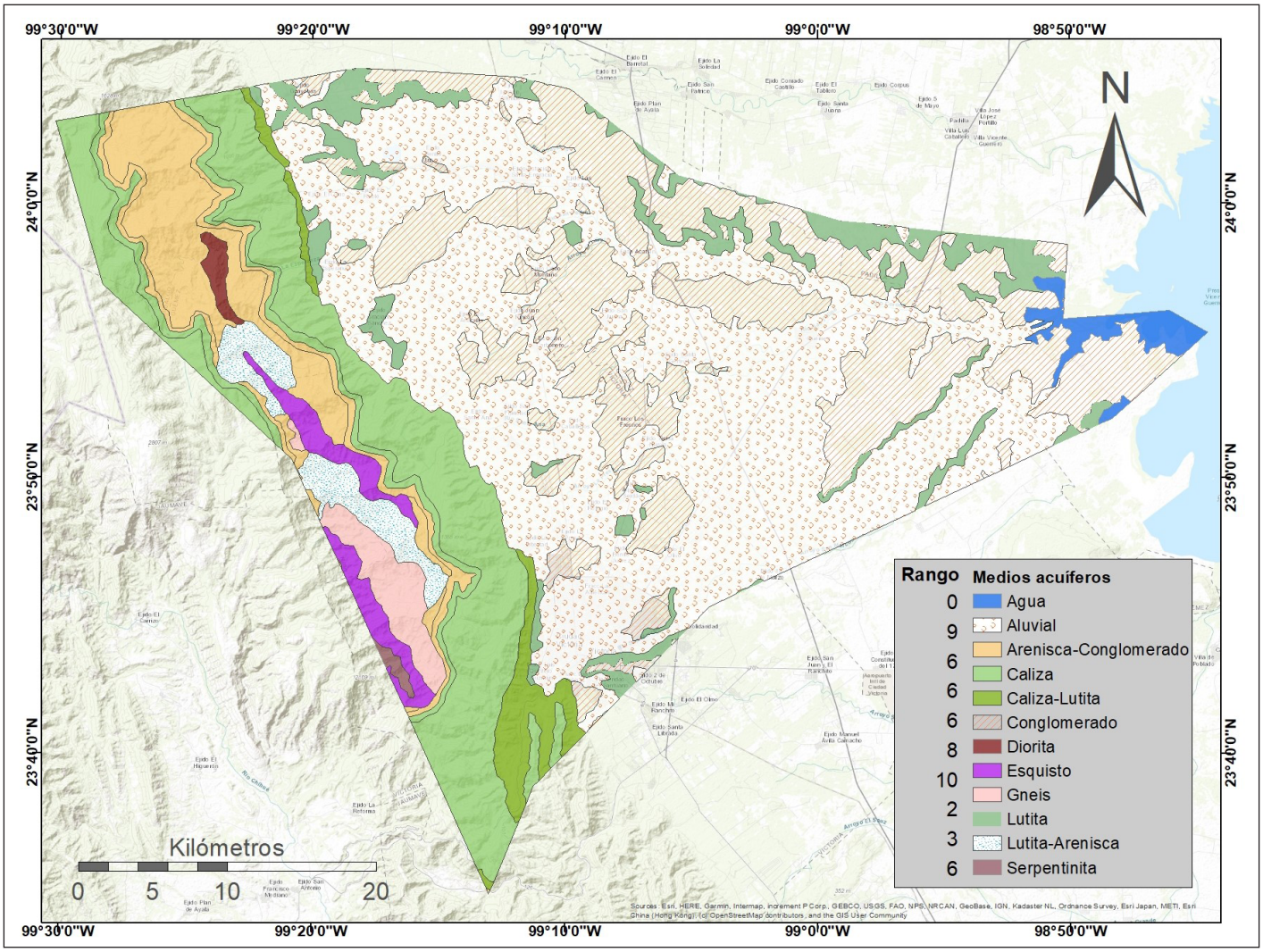

Figura 7. Medios acuíferos del acuífero Victoria – Güémez.

cilaron entre 180 y 255 mm año^{-1}. Estos resultados fueron opuestos a los de las zonas de la Sierra Madre Oriental, donde se presenta escasa o nula actividad humana.

Ye *et al.* (2019), demostraron que el consumo de agua del suelo asociado a la actividad de la vegetación depende principalmente de la precipitación, tipo de vegetación y la actividad humana, sin embargo, una zona dentro de la urbanización de Ciudad Victoria obtuvo valores de 0 a 50 mm año^{-1}. Hall *et al.* (2020), mencionan al respecto, que la urbanización produce importantes cambios a la estructura física de la superficie terrestre y al subsuelo poco profundo, además de afectar los patrones de uso del agua que cuentan con la capacidad de afectar el balance hídrico de las cuencas y los acuíferos.

3. Medios acuíferos

De norte a sur, en la parte oeste de la zona de estudio que corresponde a la Sierra Madre Oriental predominan las rocas calizas y calizas-lutitas (Figura 7). Por lo tanto, la vulnerabilidad del acuífero se encuentra en un nivel medio. Sin

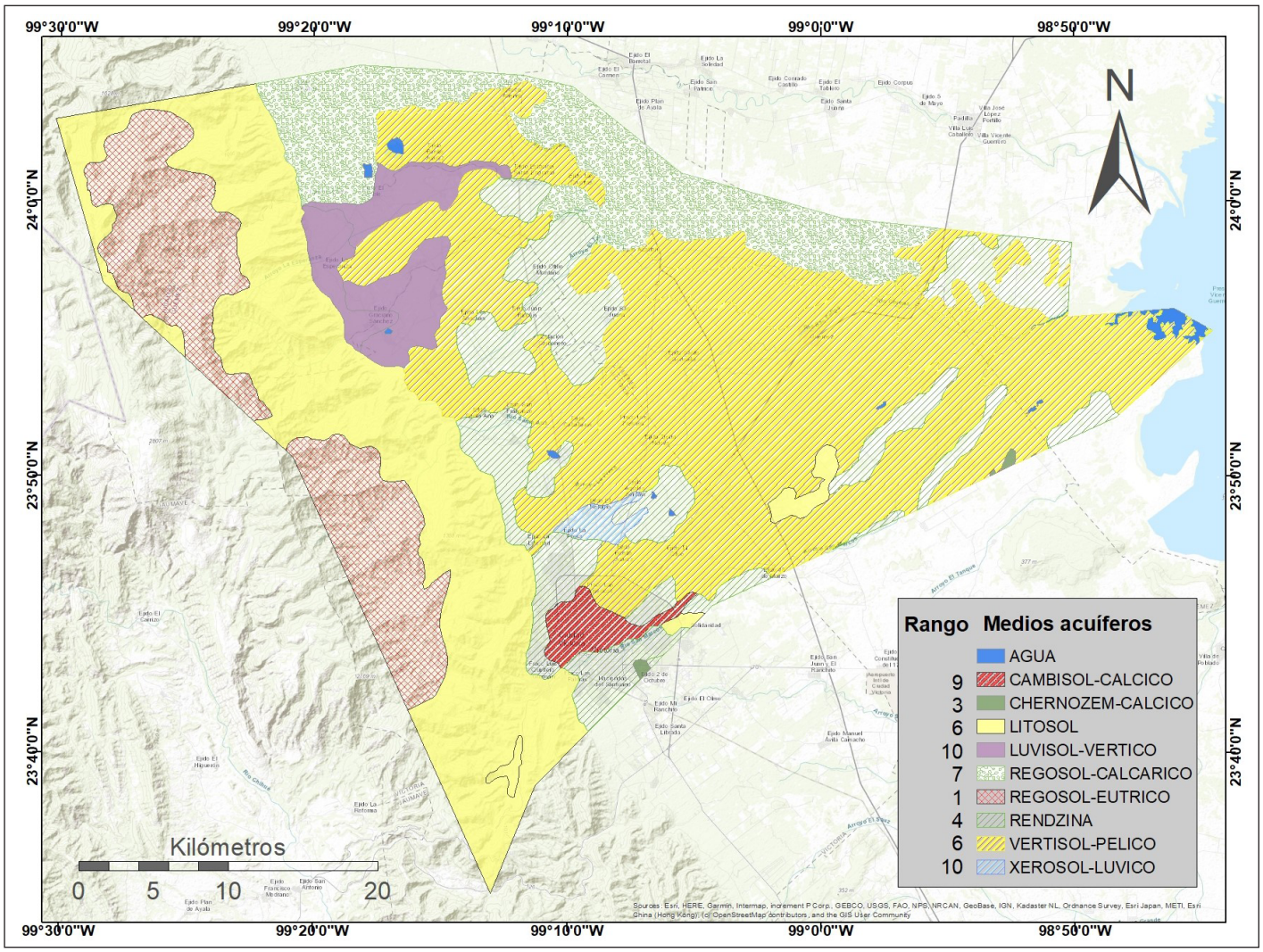

Figura 8. Medios del suelo en el acuífero.

embargo, el conglomerado y el material aluvial predominan en el resto de la zona de estudio. Este último está presente en la zona urbana de Ciudad Victoria y de acuerdo con lo que reportan Mendieta-Mendoza *et al.* (2021), las zonas donde se ubica el material aluvial se asocian con las áreas de mayor vulnerabilidad.

4. Medios del suelo

A través de la mayor parte de la zona de estudio, se distribuyen los suelos tipo Vertisol (Figura 8), siendo el tipo de suelo más abundante. El Vertisol está presente en la mayoría de las zonas agrícolas que se encuentran dentro del acuífero. En la parte norte del acuífero el tipo de suelo que predomina es el Regosol-Calcárico, mientras que en la parte oeste predomina el Regosol-Eútrico y en la zona serrana al poniente, lo hace el Vertisol.

Muhammad *et al.* (2015) mencionan que, durante la recarga, la capa de medios del suelo retiene los contaminantes al momento de infiltrarse hacia el agua subterránea, retardando la contaminación. Por su parte, Vu *et al.* (2021) reportan que

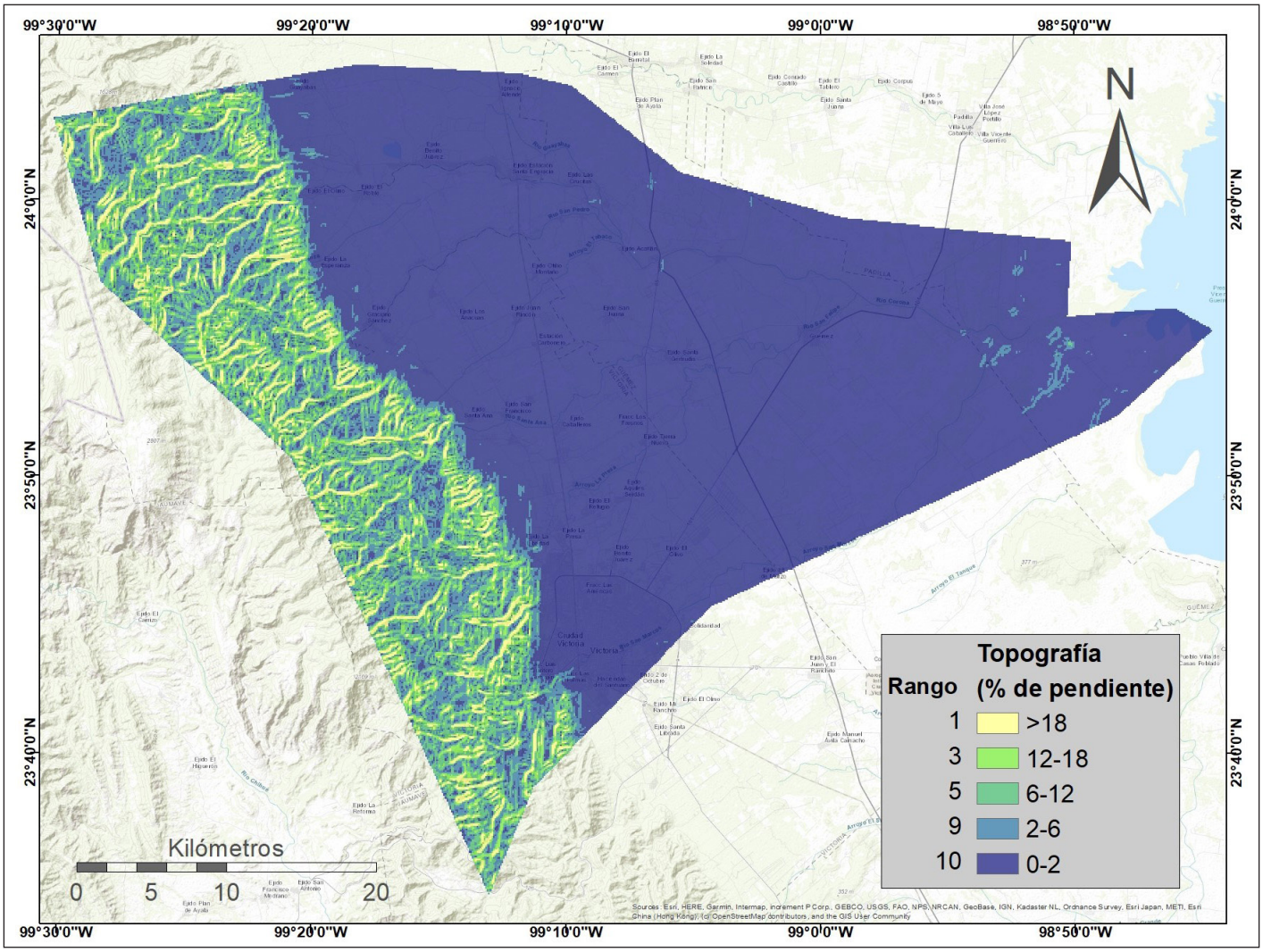

Figura 9. Topografía (pendiente) del acuífero Victoria-Güémez.

mientras más extendidas sean las zonas agrícolas, el potencial de contaminación de las aguas subterráneas aumenta.

5. Topografía

Los mayores porcentajes de la pendiente se identificaron en toda la parte oeste de la zona de estudio, donde se encuentra la Sierra Madre Oriental, con valores de la pendiente mayores de 18 % (Figura 9). De acuerdo con lo que mencionan Abunada *et al.* (2021), mientras mayor sea la pendiente menor será la vulnerabilidad en esa zona, debido a que disminuye la capacidad de que un contaminante entre en contacto con el agua subterránea. En el resto del acuífero, las zonas son de tendencia plana, con escasos lomeríos, por lo que la pendiente oscila entre 0-2%; lo que aporta a una mayor vulnerabilidad de su territorio.

6. Impacto en los medios de la zona vadosa

Para la zona no saturada que se encuentra entre la capa superficial del suelo, también llamada zona vadosa, el material predominante corresponde a rocas calizas y material aluvial

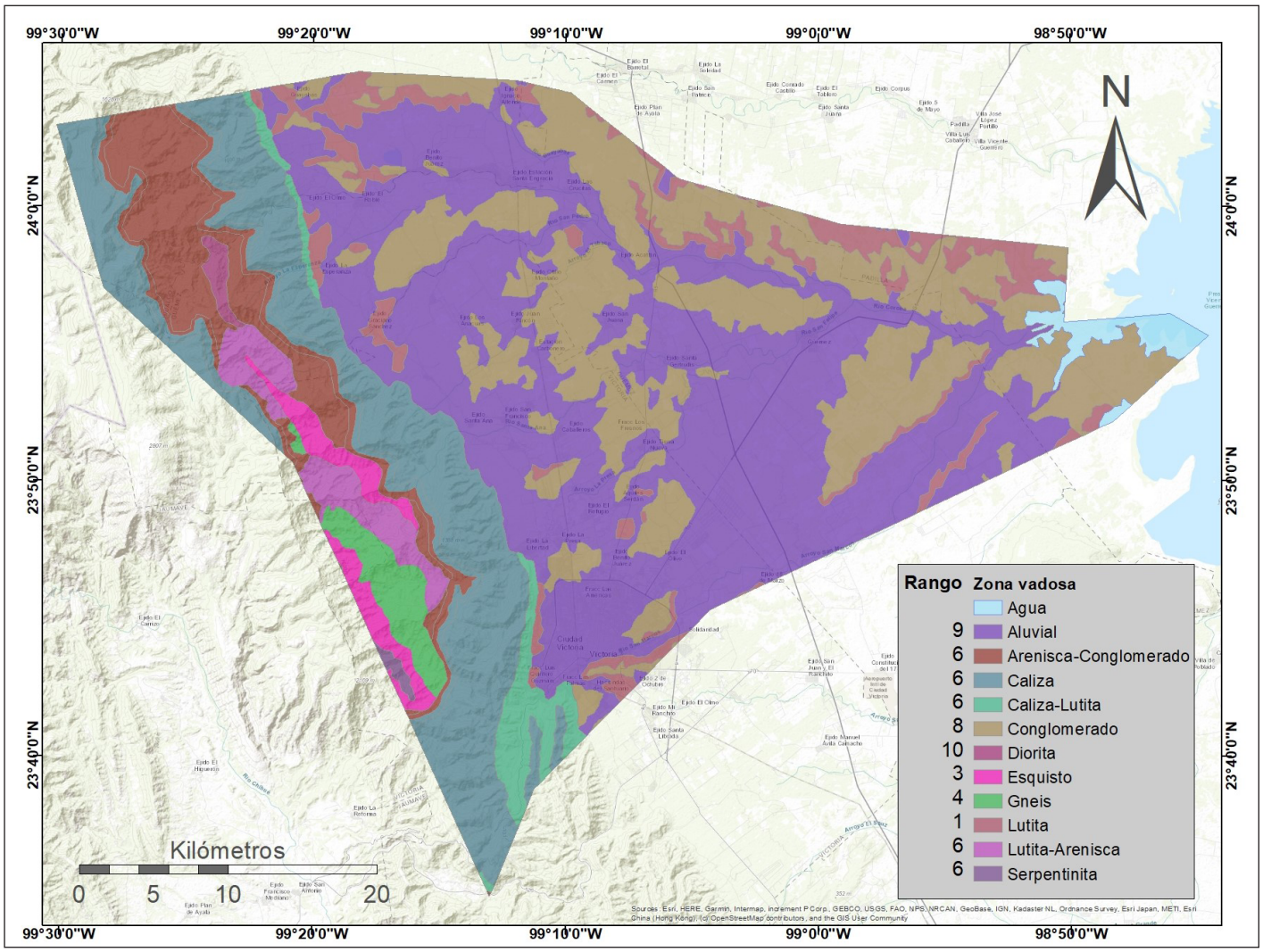

Figura 10. Impacto en los medios de la zona vadosa del acuífero.

(Figura 10). Los elementos geológicos de tipo sedimentario como las calizas, que subyacen a entornos aluviales de arenas, cuentan con características de conductividad hidráulica, que hacen a los acuíferos formados por estos materiales muy susceptibles a la infiltración de contaminantes (Bonacci 1987; Kozlowski & Sojka 2019; Pathak & Bhandary 2020)

7. Conductividad hidráulica

La conductividad hidráulica depende del material geológico presente en el acuífero, y para la mayor parte del área de estudio se estimaron rangos de 0 a 4 m día-1 (Figura 11). En la zona que corresponde al área urbana de Ciudad Victoria, se presentan estos valores, por lo que, de acuerdo con Abunada *et al.* (2021), en esos sitios se perfila una vulnerabilidad más alta, debido al corto tiempo que le toma a un contaminante recorrer los distintos poros y entrar en contacto con el agua subterránea.

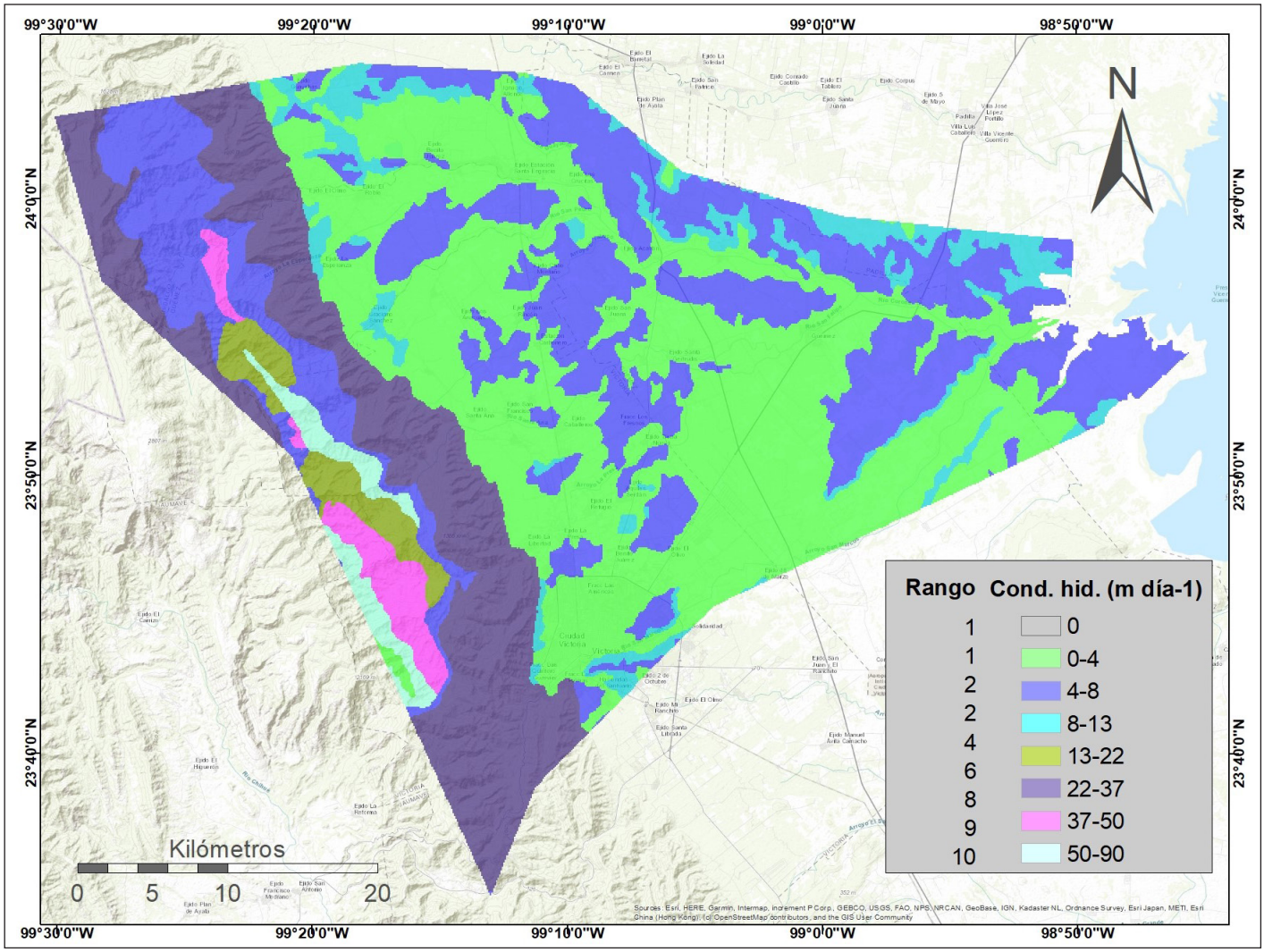

Figura 11. Conductividad hidráulica del acuífero.

8. Vulnerabilidad del acuífero Victoria - Güémez

El acuífero Victoria-Güémez presenta siete de los ocho niveles de vulnerabilidad clasificados por Aller *et al.*, 1987. Es importante señalar que las áreas con los más altos niveles registrados son poco significativas, ya que en conjunto no alcanzan a ocupar ni un punto porcentual del área de estudio. Sin embargo, cabe destacar que un 76.6% del acuífero presenta niveles de moderado a moderado-alto de vulnerabilidad (Tabla 12).

Tabla 12. Resultados de la clasificación del cálculo del índice DRASTIC

IndxV	Vulnerabilidad	Superficie (Ha)	Porcentaje
Sin datos	n/a	1,996	1.04%
62-79	Muy Baja	709	0.4%
80-99	Baja	15,195	7.9%
100-119	Baja - Moderada	26,271	13.7%
120-139	Moderada	100,556	52.3%
140-159	Moderada Alta	46,536	24.2%
160-179	Alta	968	0.5%
180-184	Muy Alta	7	0.004%

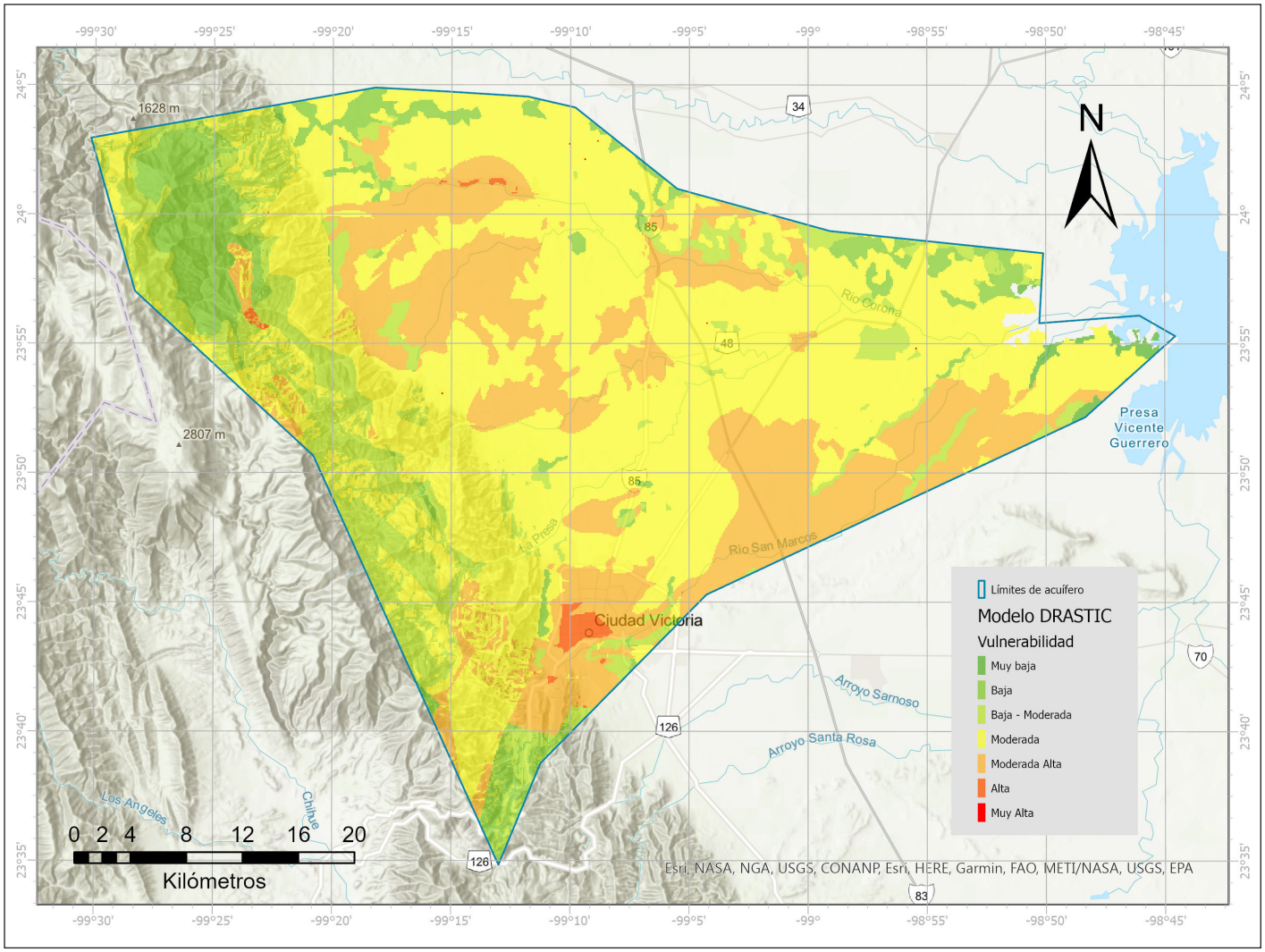

Figura 12. Vulnerabilidad del acuífero Victoria-Güémez.

En cuanto a su distribución territorial (Figura 12), las zonas menos vulnerables se localizan donde coincide una topografía de sierra o lomeríos asociados a la formación Méndez, conformado principalmente sobre lutitas con componentes arcillosos (Palmer 1927), con baja permeabilidad en la zona vadosa. Esto coincide con lo referido por Sadat-Noori & Ebrahimi (2015), quienes mencionan que factores como la alta profundidad del nivel freático y una baja permeabilidad en la zona vadosa generan bajo potencial de contaminación. De igual forma, algunas zonas asociadas a la parte alta de la Sierra Madre Oriental presenta valores de baja vulnerabilidad (zonas en color verde), áreas donde abundan calizas fracturadas que generan entornos altamente susceptibles a la infiltración de contaminantes (Henry & Suk 2018), pero que en este caso en particular, se clasifican como de vulnerabilidad baja, debido a la topografía escarpada de la zona.

En contraparte, prácticamente toda la parte central del territorio presenta una vulnerabilidad de moderada a muy alta. Se trata de las partes más planas del territorio estudiado donde se presentan profundidades del nivel freático bajas y medias, con medios aluviales y conglomerados con alta permeabilidad en la zona vadosa asociado a Formaciones Neógenas. Este tipo de entorno es vulnerable a la contaminación por las actividades que se desarrollan en la superficie, que actualmente predominan entornos agrícolas, susceptibles a contaminar con NO_3 y residuos de insumos agrícolas (Kozlowski & Sojka 2019). Por otro lado, en algunas zonas clasificadas con vulnerabilidad moderada y moderadamente alto, concurren condiciones con una topografía accidentada, en partes de la SMO dónde coincide una litología de calizas con suelos litosoles asociados a la Formación Tamaulipas.

En la zona urbana de Ciudad Victoria se presenta una vulnerabilidad muy alta del acuífero. Ahí concurre la presencia de asentamientos urbanos, que es donde se concentra la mayor carga de contaminación por presencia de automóviles, gasolineras, fábricas y talleres mecánicos, sumado a rangos de profundidad de 1 a 9 m, una recarga neta de 0 a 50 mm año-1, material aluvial y conglomerado, además de una conductividad hidráulica con valores de 0 a 4 m día-1. Los entornos urbanos son zonas con una alta vulnerabilidad

intrínseca, debido a la concentración de actividades y de seres humanos, por lo que, para efectos de estudios territoriales regionales, es normal y hasta predecible, que dichas zonas tengan alta vulnerabilidad (Vystavna et al, 2017).

Conclusiones

La modificación al factor de recarga mediante el uso del modelador *Water Yield* de InVEST, resultó en un modelo territorial de precisión adecuada para complementar la información hidrológica en el índice DRASTIC. Las áreas clasificadas por el modelo como vulnerables presentan una coherencia, aun y cuando el modelo presenta limitaciones en la calidad y la escala de los datos ingresados, el modelo se ajustó y brindó información suficiente. De acuerdo con lo representado en el modelo DRASTIC, el acuífero Victoria-Güémez presenta un 50% de su superficie con vulnerabilidad moderada, lo cual remarca la importancia de este tipo de instrumentos, para delimitar geográficamente, las características de vulnerabilidad del acuífero a ser degradado.

Los resultados de este análisis muestran que el acuífero Victoria-Güémez se encuentra expuesto casi en la totalidad de su territorio a vulnerabilidad a la contaminación con niveles moderados a muy altos. La mayor coincide con la zona urbana del municipio de Ciudad Victoria y en el poblado de Santa Engracia. Por esta razón, estos deberían considerarse como sitios prioritarios para la toma de decisiones y acciones que prevengan la contaminación en los pozos de agua que abastecen a sus usuarios.

Es necesario considerar que el modelo presentado tiene algunas limitaciones importantes, que básicamente provienen de la calidad de los datos ingresados, que depende de las fuentes; por ello, no fue posible sustituir la mayoría de la información cartográfica, pues es la existente en las fuentes oficiales, con escala de 1:250,000. La modelación de la profundidad freática se interpoló a partir de la información disponible de la profundidad de los pozos, por lo que es sólo un indicativo de ese valor. Por lo que, algunas formas plausibles para afinar este modelo, serían sustituir la evpotranspiración, la precipitación y la vegetación y uso de suelo por datos geoespaciales para estimar la recarga del acuífero; además, podrían utilizarse una mayor cantidad de mediciones piezométricas el acuífero y sus alrededores. Finalmente, debería utilizarse cartografía digital geológica y edafológica a una escala local, ya sea producida por fuentes oficiales o por proyectos específicos de la región.

El presente análisis debe considerarse como un primer avance en el desarrollo de una herramienta de gestión del agua subterránea, pues el déficit de agua del acuífero es notorio. Y como las leyes estatales y nacionales carecen de atribuciones para tomar decisiones en materia de administración del agua, es necesario tomar acciones que generen un adecuado plan de gestión, en conjunto con los tomadores de decisiones. Por estas razones, se propone que se afine más el modelo, utilizando la información digital ya mencionada, para continuar monitoreando la situación del acuífero.

Referencias

Abunada, Z., Kishawi, T., Alslaibi, Kaheil, N. and Mittelstet, A. 2021. The application of SWAT-GIS tool to improve the recharge factor in the DRASTIC framework: Case study. Journal of Hydrology, 592,125613.

Aguilar, D., Bautista, F., Mendoza, M. y Delgado, C. 2013. Vulnerabilidad y riesgo de contaminación de acuíferos kársticos. Tropical and Subtropical Agroecosystems 16,243-263.

Aller, L., Lehr, J. and Petty, R. 1987. A standardized system to evaluate ground water pollution potential using hydrogeologic settings Natl. Water Well Assoc.

Bera, A., Mukhopadhyay, B. P., Chowdhury, P., Ghosh, A., and Biswas, S., 2021. Groundwater vulnerability assessment using GIS-based DRASTIC model in Nangasai River Basin, India with special emphasis on agricultural contamination. *Ecotoxicology and Environmental Safety*, 214, 112085.

Bonacci Ognjen, 1987. Karst Hydrology, Springer Verlag, Berlin.

Caballero, A., 2020. La Sequía En México, Un Efecto Más De La Crisis Climática En Los Recursos Hídricos. *Crisis Climática Y Recursos Hídricos*, 27.

Comisión Nacional del Agua (CONAGUA). 2017. Disponibilidad de agua por acuífero. Valores de los términos que intervienen en su determinación conforme a la NOM-011-CONAGUA-2003. Cartografía digital, escala 1:250,000

Comisión Nacional del Agua CONAGUA. 2018. Estadísticas del agua en México. Edición 2018. **https://files.conagua.gob.mx/conagua/publicaciones/Publicaciones/EAM2018.pdf** 303 p.

Comisión Nacional del Agua CONAGUA. 2018b. Atlas del agua en México. Edición 2018 **https://files.conagua.gob.mx/conagua/publicaciones/Publicaciones/AAM2018.pdf** 147 p.

Diario Oficial de la Federacion . 2020. Actualización de la disponibilidad media anual de agua en el acuífero Victoria - Güémez (2807), Estado de Tamaulipas.

Comisión Nacional para el Conocimiento y Uso de la Biodiversidad (CONABIO). 1998. Cartografía digital de Subcuencas hidrológicas, escala 1:000,000,000. **http://www.conabio.gob.mx/informacion/metadata/gis/subcu1mgw.xml?_httpcache=yes&_xsl=/db/metadata/xsl/fgdc_html.xsl&_indent=no**

Foster, S. 1987. Fundamental Concepts in Aquifer Vulnerability, Pollution Risk and Protection Strategy: International Conference, Noordwijk Aan Zee, the Netherlands Vulnerability of Soil and Groundwater to Pollutants. Netherlands Organization for Applied Scientific Research, The Hague, 69-86.

Fijani, E., Nadiri, A. Moghaddam, A., Tsai, T. and Dixon, B. 2013. Optimization of DRASTIC method by supervised committee machine artificial intelligence to assess groundwater vulnerability for Maragheh–Bonab plain aquifer, Iran. *Journal of Hydrology* 503, 89-100.

Freeze, R. A., & Cherry, J. A., 1979. Groundwater. Englewood Cliffs, N.J: Prentice-Hall.

González, R., Albornoz, B., Sanchez, I., y Osorio, J., 2018. El acuífero yucateco. Análisis del riesgo de contaminación con apoyo de un sistema de información geográfica. *Revista Internacional de Contaminación Ambiental* 34,667-683.

Instituto Nacional de Estadística y Geografía (INEGI). 2013. Conjunto de datos vectoriales de uso de suelo y vegetación escala 1:250 000, serie V. 2da. Edición. Instituto Nacional de Estadística y Geografía. Aguascalientes, Aguascalientes. **http://www.conabio.gob.mx/informacion/metadata/gis/usv250s5ugw.xml?_httpcache=yes&_xsl=/db/metadata/xsl/fgdc_html.xsl&_indent=no**

INEGI. 2015. "Continuo de Elevaciones Mexicano 3.0". De **https://www.inegi.org.mx/app/geo2/elevacionesmex/**

INEGI. 2020. Resultados definitivos del Censo de Población y Vivienda 2020. **https://www.inegi.org.mx/servicios/widgets_poblacion.html**

Instituto Nacional de investigaciones Forestales y Agropecuarias (INIFAP). 1995. Comisión Nacional para el Conocimiento y Uso de la Biodiversidad (CONABIO), 'Edafología'. Escala 1:250000

Instituto Mexicano de Tecnología del Agua (IMTA). 1996. Estaciones climatológicas del país obtenidas del Extractor Rápido de Información Climatológica (ERIC). Catálogo de metadatos geográficos. Comisión Nacional para el Conocimiento y Uso de la Biodiversidad. Disponible en: **http://www.conabio.gob.mx/informacion/metadata/gis/estclimgw.xml?_httpcache=yes&_xsl=/db/metadata/xsl/fgdc_html.xsl&_indent=no**

Jia, Z., Bian, J., Wang, Y., Wan, H., Sun, X., and Li, Q., 2019. Assessment and validation of groundwater vulnerability to nitrate in porous aquifers based on a DRASTIC method modified by projection pursuit dynamic clustering model. *Journal of contaminant hydrology*, 226, 103522.

Kozłowski, M., and Sojka, M. 2019. Applying a Modified DRASTIC Model to Assess Groundwater Vulnerability to Pollution: A Case Study in Central Poland. *Polish Journal of Environmental Studies*, 28(3).

Mendieta-Mendoza, A., Hanson, R., and Renteria-Villalobos, M. 2021. Potential adverse impacts on vulnerability and availability of groundwater from climate-change and land use. *Journal of Hydrology*, 594:125978.

Mendoza, G., Ennaanay, D., Conte, D., Walter, M., Freyberg, D., Wonly, S., Hay, L., White, S., Nelson, E., and Solórzano, L. 2011. Chapter 4. Water supply as an ecosystem service for hydropower and irrigation. Natural Capital. *Theory and Practice of Mapping Ecosystem Services*. Oxford University Press. Oxford. 365 pp.

Muhammad, A., Zhonghua, T., Dawood, A., and Earl, B. 2015. Evaluation of local groundwater vulnerability based on DRASTIC index method in Lahore, Pakistan. *Geofísica internacional*, 54, 67-81.

Palmer, R.H., 1927, Geology of eastern Hidalgo and adjacent parts of Vera Cruz, Mexico: American. Association of Petroleum Geologists, Bulletin, 11(12), 1173-1220.

Ríos-Sánchez, K., Sánchez, E., Santillan, Y., Ramírez, C., y Flores, M. 2020. Expansión urbana descontrolada: ¿Qué pasará con el agua? Pädi *Boletín Científico de Ciencias Básicas e Ingenierías del ICBI*, 54-59.

Sadat-Noori, M., and Ebrahimi, K. 2016. Groundwater vulnerability assessment in agricultural areas using a modified DRASTIC model. *Environmental monitoring and assessment*, 188, 19.

Saxton, K.E. 2005. SPAW, Soil-Plant-Air-Water. Field and Pond Hydrology. Versión 6.02.75. USDA Agricultural Research Service y Departament of Biological Systems Engineering de Washington State University.

Servicio Geológico Mexicano (SGM). 1995. Continúo Nacional de Geología de la República Mexicana de los años 1995 y 2005 con datos geológicos generados corresponden a la serie en formato digital de los años 1995 y 2005 escala 1:250,000

Sharp, R., Douglass, J., Wolny, S., Arkema, K., Bernhardt, J., Bierbower, W., Chaumont, N., Denu, D., Fisher, D., Glowinski, K., Griffin, R., Guannel, G., Guerry, A., Johnson, J., Hamel, P., Kennedy, C., Kim, C.K., Lacayo, M., Lonsdorf, E., Mandle, L., Rogers, L., Silver, J., Toft, J., Verutes, G., Vogl, A. L., Wood, S, and Wyatt, K. 2020. InVEST 3.9.0.post86+ug.g1897be6 User's Guide. The Natural Capital Project, Stanford University, University of Minnesota, The Nature Conservancy, and World Wildlife Fund.

Thapa, R., Gupta, S., Guin, S., and Kaur, H. 2018. Sensitivity analysis and mapping the potential groundwater vulnerability zones in Birbhum district, India: a comparative approach between vulnerability models. *Water Science*, 32,1, 44-66.

Trabucco, A. and Zomer, R. 2009. *Global Aridity Index (Global-Aridity) and Global Potential Evapo-Transpiration (Global-PET) Geospatial Database*. CGIAR Consortium for Spatial Information. Published online, available from the CGIAR-CSI GeoPortal

UAT (Universidad Autónoma de Tamaulipas). 2001. Diagnóstico Ecológico del Estado de Tamaulipas. Documento inédito. Ciudad Victoria. México.

Vu, T., Ni, C., Li, W., Truong, M., and Hsu, S., 2021. Predictions of groundwater vulnerability and sustainability by an integrated index-overlay method and physical-based numerical model. *Journal of Hydrology*, 596, 126082.

Vystavna, Y., Diadin, D., Yakovlev, V. 2017. Nitrate contamination in a shallow urban aquifer in East Ukraine: evidence from hydrochemical, stable isotopes of nitrate and land use analysis. *Environ Earth Sci* 76, 463. **https://doi.org/10.1007/s12665-017-6796-1**

Zhang, L., Hickel, K., Dawes, W., Chiew, F., Western, A., y Briggs, P. 2004. A rational function approach for estimating mean annual evapotranspiration. *Water Resources Research.* 40 (2).

Geofísica Internacional (2023) **62-2**: 487 - 506

Joint stochastic simulation of petrophysical properties with elastic attributes based on parametric copula models

Daniel Vázquez-Ramírez[1*], Van Huong Le[2], Martín A. Díaz-Viera[3], Raúl del Valle-García[4], Arturo Erdely[5]

Resumen

El método de co-simulación estocástica espacial, basado en cópulas, es un método general que permite simular variables con cualquier tipo de dependencia y funciones de distribución de probabilidad. Esta flexibilidad proviene del uso de un modelo de cópula para la representación de la función de distribución de probabilidad conjunta. El método se ha implementado principalmente a través de un enfoque no paramétrico utilizando cópulas de Bernstein y se ha aplicado con éxito para la simulación de propiedades petrofísicas usando atributos sísmicos elásticos como variables secundarias. En el presente trabajo este método se implementa mediante otros dos enfoques: paramétrico y semi-paramétrico. Específicamente, para el enfoque paramétrico se usa la familia de cópulas Arquimedianas. Primero, el enfoque paramétrico se valida con un caso publicado y luego se realiza una comparación de los tres enfoques en términos de precisión y rendimiento. Los resultados mostraron que el enfoque paramétrico es el que peor reproduce las estadísticas de los datos y presenta mayor incertidumbre con un menor costo computacional, mientras que el enfoque no-paramétrico resultó el que mejor reproduce la dependencia de los datos a un alto costo computacional. El enfoque semi-paramétrico reduce un 10% el costo computacional respecto al no-paramétrico, pero se degrada significativamente su precisión.

Palabras Clave: co-simulación, cópulas, Bernstein, Arquimedeanas, propiedades petrofísicas, atributos sísmicos elásticos.

Abstract

The spatial stochastic co-simulation method based on copulas is a general method that allows simulating variables with any type of dependency and probability distribution functions. This flexibility comes from the use of a copula model for the representation of the joint probability distribution function. The method has been mainly implemented through a non-parametric approach using Bernstein copulas and has been successfully applied for the simulation of petrophysical properties using elastic seismic attributes as secondary variables. In the present work this method is implemented through two other approaches: parametric and semi-parametric. Specifically, for the parametric approach the family of Archimedean copulas is used. First, the parametric approach is validated against a published case, and then a comparison of the three approaches in terms of accuracy and performance is made. The results showed that the parametric approach is the one that reproduces the data statistics worse and presents greater uncertainty with a lower computational cost, while the non-parametric approach was the one that best reproduces the dependence of the data at a high computational cost. The semi-parametric approach reduces the computational cost by 10% compared to the non-parametric approach, but its accuracy is significantly degraded.

Keywords: co-simulation, copulas, Bernstein, Archimedean, petrophysical properties, elastic seismic attributes.

Received: April 4, 2022; Accepted: August 16, 2022; Published on-line: April 1, 2023.

Editorial responsibility: Ana Teresa Mendoza Rosas

* Corresponding author: Daniel Vázquez Ramirez
[1] Posgrado de Ciencias de la Tierra, Universidad Nacional Autónoma de México, Circuito de Posgrado S/N, Coyoacán Ciudad Universitaria, 04510 Ciudad de México, Mexico, daniel.geofisico89@comunidad.unam.mx ORCID: 0000-0002-6326-9141
[2] Department of Plant & Soil Sciences, University of Delaware, Newark, Delaware 19716, United States, levanhuong15011989@gmail.com ORCID: 0000-0002-3700-9987
[3] Instituto Mexicano del Petróleo, Eje Central Lázaro Cárdenas No. 152, Col. San Bartolo Atepehuacan, México D.F. 07730, Mexico, mdiazv@imp.mx ORCID: 0000-0001-5811-6186
[4] Independent consultant, Ciudad de México, México. raul.vontal@gmail.com ORCID: 0000-0001-8964-714X
[5] Universidad Nacional Autónoma de México, FES Acatlán, Avenida Alcanfores y San Juan Totoltepec S/N, Santa Cruz Acatlán, 53150 Naucalpan de Juárez, Mexico, aerdely@acatlan.unam.mx ORCID: 0000-0003-1653-8342

https://doi.org/10.22201/igeof.2954436xe.2023.62.2.1593

1. Introduction

One of the most common problems of reservoir geological-petrophysical modeling workflow (Cosentino, 2001) consists in predicting petrophysical properties considering the dependency relationships with the seismic attributes. For this purpose, different methods and approaches have been used, ranging from empirical relationships (Diaz-Viera *et al.*, 2006), regression methods, neural networks (Parra *et al.*, 2014), (Iturraran-Viveros & Parra, 2014) to spatial stochastic models. The latter being more flexible since they better reproduce the statistical and spatial behavior of petrophysical properties(Pyrcz & Deutsch, 2014).

In the last decade, various spatial stochastic simulation methods, also known as geostatistical simulation methods, have been developed. Among the most used are: Monte Carlo simulation (Bosch *et al.*, 2007), (Oh & Kwon, 2001) and (Grana, 2014), sequential indicator simulation (Caers *et al.*, 2000), direct simulation (Azevedo & Soares, 2017) or sequential Gaussian simulation whose methods are widely developed in the works of (Chilès & Delfiner, 1999), (Dubrule *et al.*, 2003), (Bortoli *et al.*, 1993) and (Pyrcz & Deutsch, 2014).

The disadvantage of most of these methods is that they assume that the data follow Gaussian distributions and that the dependency relationships between them are linear, which makes their application to real problems very limited. In the best case, it is forced to be applied by data transformation, which produces biased results when they are back transformed.

The copula-based spatial stochastic co-simulation method was proposed by (Diaz-Viera *et al.*, 2017) as an alternative to the aforementioned simulation methods. This method can be basically divided into two steps. Firstly, a dependence model between the primary and secondary variables is established by estimating and modeling the joint cumulative probability distribution function (CPDF) using a copula. The CPDF model is used in conjunction with a variogram (spatial correlation) model to simulate the primary variable using the second one as a conditioning variable. This last step can be done in a global optimization framework using one method, such as simulated annealing, but other methods, such as genetic algorithms, can also be applied.

Recently, the copula-based simulation method was successfully applied for the prediction of petrophysical properties using seismic attributes as a secondary variable in (Le, 2021), (Le *et al.*, 2020), (M. Díaz-Viera *et al.*, 2018), (Vázquez, 2018). But in these works, the method was implemented using a non-parametric approach with Bernstein copulas. The non-parametric approach has the disadvantage that it requires a high computational cost, especially when calculating the joint probability distribution function estimated with the Bernstein copula.

In this work it is proposed to use a parametric copula model, through the implementation of Archimedean copula family. This approach is expected to reduce the computational cost. The paper aim is to compare the parametric, semi-parametric and non-parametric approaches in terms of precision and performance. The comparative study is carried out through the application to two case studies in a marine reservoir in the Gulf of Mexico, where the total porosity and the density are simulated by means of the acoustic impedance and the P-wave velocity as secondary variables, respectively.

The paper has the following structure. First, the copula-based spatial stochastic co-simulation method is briefly described, distinguishing between non-parametric, semi-parametric and parametric approaches. In particular, the members of Archimedean copula family are defined. An outline of the method application workflow is provided. Subsequently, the validation of the method is carried out by applying it to a previously published case study and the three approaches are compared. Finally, the parametric approach is applied to a new case study and the conclusions are given. In appendices, the definition of copula and its basic properties, as well as the Bernstein copula simulation method description are shown.

2. Copula-based spatial stochastic co-simulation method

Copula-based spatial stochastic co-simulation had its origins in the works of (Diaz-Viera & Casar-González, 2005), (Erdely *et al.*, 2012) and (Hernandez-Maldonado *et al.*, 2014). The method has the advantages of not requiring linear dependence or a specific type of distribution and has been successfully applied to simulate petrophysical properties using seismic attributes as a secondary variable. The method has been implemented mainly by a non-parametric approach using Bernstein copulas, where the copula is estimated using the empirical copula and the variables are interpolated using Bernstein polynomial function (Appendix 10.2).

However, there are two more approaches that have not been sufficiently explored and used in the dependency model estimation: semi-parametric and parametric approaches. The semi-parametric approach estimates margins non-parametrically using empirical distribution functions and parametric copula is estimated (Jaworski *et al.*, 2010) or the margins are estimated using parametric functions and the copula is estimated non-parametrically. The parametric approach uses different parametric distribution functions that are selected and best fit the petrophysical property or seismic attribute and then couple them within the parametric copula.

The difference between the non-parametric, parametric and semi-parametric approaches lies in the estimation procedure. In the non-parametric approach, the behavior of the joint sampling distribution function is adapted by means of a polynomial approximation, reducing the estimation variance.

In the parametric approach, the data samples are fitted to copula models and parametric probability distribution functions. While the semi-parametric approach is a combination of the two previous approaches, and therefore, there are two options: parametric copulas with non-parametric marginals, or non-parametric copulas with parametric marginals. Therefore, if the joint distribution function that allows relating two or more petrophysical properties and seismic attributes in terms of their dependence is generated, it is possible to obtain more consistent simulations with their data sample statistics without having to assume a specific distribution or dependency. In the following subsections the parametric joint distribution functions are analyzed, especially the Archimedean copula family.

2.1 Parametric copula approach

The parametric copulas are a classification of copula whose advantage is to use the parameters of the joint function to control the dependence. There are three great parametric copula families: elliptical, Archimedean and extreme values (Joe, 2014).

The elliptical copulas are recommended when the dependence model is derivated from elliptical distributions and the symmetry should be elliptical respect to the diagonal (Shemyakin & Kniazev, 2017). Gaussian and *t*-copula are examples of elliptical copulas.

The extreme value copulas are based on random vectors distributed according to multivariate extreme value distributions. Galambos, Hüstle-Reis and Tawn are examples of extreme values copulas (Hofert *et al.*, 2019).

Archimedean copulas are the most used copulas because they are easier for implementation, they just need one parameter θ to control the dependence and the differentiation and integration to obtain the generator and inverse is simple (Shemyakin & Kniazev, 2017). Frank, Gumbel and Clayton are examples of Archimedean copulas.

2.1.1 Archimedean copulas

After describing the basic properties of copulas (Appendix 10.1), it is necessary to study a class of copulas that will be useful for the development of Copula-based spatial stochastic co-simulation: Archimedean copulas. These copulas are very useful alternatives because they are easy to build and there is a wide variety of families of copulas with interesting properties (Nelsen, 2006).

$$C(u,v)=\varphi^{[-1]}(\varphi(u)+\varphi(v)) \qquad \text{(Eq. 1)}$$

The (Eq. 1) is the Archimedean copula. The φ function is called copula generator. Consider that if $\varphi(0)=\infty$ then φ is strictly generator, in that case $\varphi^{[-1]}=\varphi^{-1}$ and $C(u,v)=\varphi^{[-1]}(\varphi(u)+\varphi(v))$ and is said to be strictly an Archimedean copula. Another important property is the Archimedean density copula (Eq. 2), this can be expressed through the generator and its derivatives as (Shemyakin & Kniazev, 2017):

$$c(u,v)=\frac{\delta^2 C(u,v)}{\delta u \delta v}=\frac{\varphi''\left(C(u,v)\right)\varphi'(u)\varphi'(v)}{\left(\varphi'\left(C(u,v)\right)\right)^3} \qquad \text{(Eq. 2)}$$

2.1.1.1 Clayton copula

This family of copulas has been used when the dependence of the tails is strong on the left and weak on the right. Generally, Clayton copula does not accept negative dependencies, the copula parameter θ is restricted into the region $(0,\infty)$, if the value of θ is zero, then the marginals become independent (Trivedi & Zimmer, 2007). Some members of Clayton copula can be implemented in models with negative dependencies; however, its use is not suggested under those conditions because the copula is not strict and it can violate the region restriction; reflecting the shape of the countermonotocity copula as the value of θ approaches -1, which itself is not an Archimedean copula. It cannot properly capture the negative dependency nor estimate the value of the parameter θ special conditions are needed to guarantee that the copula is strict (Cooray, 2018). The Clayton copula that can be evaluated in negative dependencies is defined as:

$$C_\theta(u,v)=\left\{\left(u^{-\theta}+v^{-\theta}-1\right)^{-\frac{1}{\theta}},0\right\} \qquad \theta\in[-1;0]\cup(0,\infty) \qquad \text{(Eq. 3)}$$

Whose generator is:

$$\varphi(t)=\frac{1}{\theta}t\left(t^{-\theta}-1\right) \qquad \text{(Eq. 4)}$$

2.1.1.2 Frank copula

This family of copulas is well known because it can be used in models with positive and negative dependencies between their marginals, it is a symmetric copula on both tails and includes both Frechet limits throughout the region $(-\infty,\infty)$. The disadvantage of Frank's copula is that the dependency tends to be weak in the tails and strong in the central part of the marginals; therefore, it is recommended to use this type of copula if the dependency model exhibits tails with low dependency (Trivedi & Zimmer, 2007). The Frank copula is defined as:

$$C_\theta(u,v)=\frac{1}{\theta}\ln\left(1+\frac{\left(e^{-\theta u}-1\right)\left(e^{-\theta v}-1\right)}{e^{-\theta}-1}\right)\ \theta\neq 0 \qquad \text{(Eq. 5)}$$

Whose generator is:

$$\varphi(t) = -\ln - \frac{e^{-\theta t} - 1}{e^{-\theta} - 1} \quad \text{(Eq. 6)}$$

2.1.1.3 Gumbel-Hougaard copula

This family of copulas, like Clayton's copula, does not allow negative dependencies. The parameter θ is restricted to the interval $[1,\infty)$, if the value is 1 the copula is considered independent, if the value of θ is ∞ it is a countermonotocity copula or upper Frechet limit. Gumbel copula exhibits strong dependence on the tails located on the right and weak on left tails, therefore, it is recommended when the highest values of the sample have strong dependence, while the low values have less dependency (Trivedi & Zimmer, 2007). The Gumbel-Hougaard copula is defined as:

$$C_\theta(u,v) = \exp\left(-\left(\left(-\ln(u)^\theta\right) + \left(-\ln(v)^\theta\right)\right)^{\frac{1}{\theta}}\right) \quad \theta \geq 1 \quad \text{(Eq. 7)}$$

Whose generator is:

$$\varphi(t) = \left(-\ln(t)\right)^\theta \quad \text{(Eq. 8)}$$

2.1.1.4 Joe copula

This copula family is based on Sibuya distribution LT (Joe, 2014). It only works with positive dependence and the goodness of fit is reasonably well when it is applied to small samples with moderate dependence (Hofert *et al.*, 2019). The Joe copula is:

$$C_\theta(u,v) = 1 - \left((1-u)^\theta + (1-v)^\theta - (1-u)(1-v)^\theta\right)^{\frac{1}{\theta}} \quad \theta \in [1-\infty] \quad \text{(Eq. 9)}$$

And the generator is:

$$\varphi(t) = -\ln\left(1-(1-t)^\theta\right) \quad \text{(Eq. 10)}$$

3. Method application workflow

The workflow follows the next steps:

1. Exploratory data analysis: this step studies the variable using statistical properties, histograms and scatter plot.
2. Variographic analysis: this step consists in estimating and modeling a spatial correlation function, as the variogram, from a random function sample (M. A. Díaz-Viera, 2002).
3. Marginal estimation and model fitting: for this step the variable is fitting using parametric probability functions, the best option is selected considering the result of log-likelihood, Akaike information criteria (AIC) and Bayesian information criteria (BIC). In case of (AIC) and (BIC) criteria, the parametric function with the lowest value will be the best fit, while the log-likelihood with the highest criterion value is the best fit. However, it is advisable to use graphical tools to assess whether the fit is adequate, therefore, the fit criteria must be confirmed using the histogram, the cumulative histogram and the cumulative distribution function.
4. Parametric copula estimation and model fitting: This step uses the results obtained in step 3 and the bivariate samples to estimate and select the best Archimedean copula model. The estimation is developed using maximum likelihood (MLE), Kendall inversion τ (ITau) and Spearman inversion ρ (IRho) (Hofert *et al.*, 2019).
5. Well-log simulation uses the joint probability distribution function using simulated annealing.
6. Compare the statistics and the spatial distribution between the variables (step 1) and the simulated variables obtained in step 5.

This algorithm is implemented using the RGEOSTAD tools (M. A. Díaz-Viera *et al.*, 2021) and GSLIB (Deutsch & Journel, 1998).

4. Method validation

To implement the stochastic simulation using parametric, semi-parametric and non-parametric copulas, the Lakach-1 geophysical well logs are taken. This well crosses the Miocene turbiditic system. This system is important due to unassociated fields discovered in this unit; the unit is divided into three sections: Lower Miocene, Middle Miocene and Upper Miocene. The age of interest of this implementation is the Lower Miocene, in this zone the flow goes from southwest to northeast with some dominant channel systems. The rocks are medium-grained sandstones; evidence of volcanic material, feldspars, quartz and some metamorphic fragments were also found. The rock is poorly consolidated and mineralogically immature; the porosity ranges from 12 to 28% (Arreguin-Lopez *et al.*, 2011). The interval to be evaluated is from 3035 to 3404.5 meters with a sampling interval of 0.1 meters.

4.1 Exploratory data analysis

Analyzing the geophysical well logs, the best option is the bivariate case (Ip, ϕ_t). The Figure 1 shows the well log plots.

The statistics are in Table 1, both well-logs have 3696 samples. The total porosity well-log (ϕ_t) has difference between the mean and the median is -0.0075, which is very low. Regarding the box plot (Figure 2, green histogram), most of the outliers are to the left of the graph. Meanwhile the impedance acoustic well log (Ip), the difference between

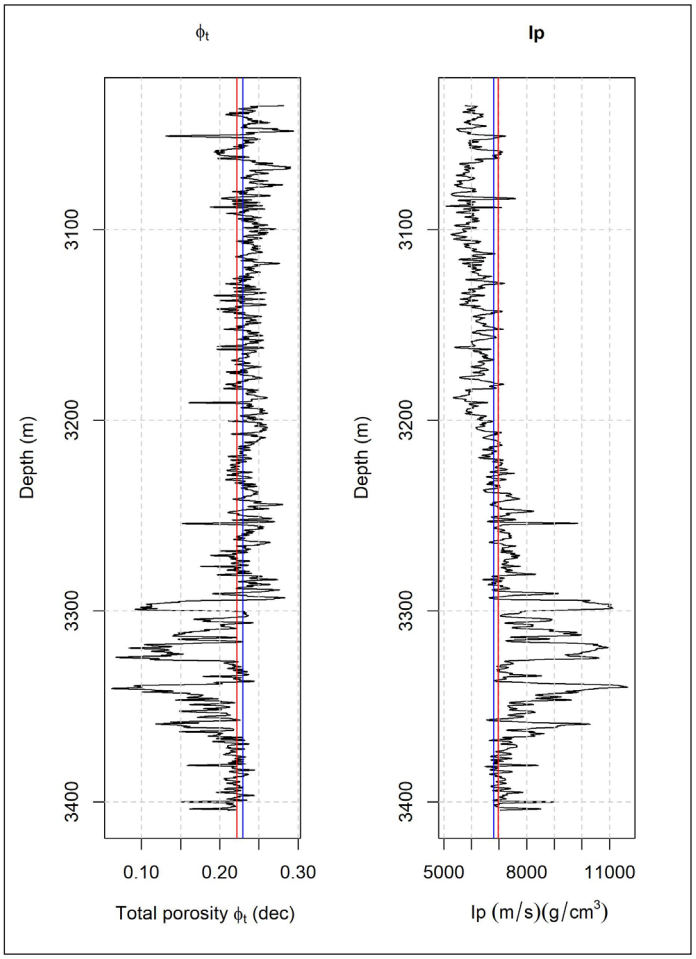

Figure 1. ϕ_t (left) and *Ip* (right) geophysical well logs.

the mean and the median is 158.7265, it indicates that it has positive skewness, which is possibly caused by the large number of outliers located to the right of the graph (Figure 2, blue histogram).

Table 1. Basic statistics of total porosity (ϕ_t) and acoustic impedance (*Ip*).

Statistics	ϕ_t	*Ip*
Samples	3696	3696
Minimum	0.0620	5086.0072
1st quartile	0.2147	6157.0051
Median	0.2295	6809.5573
Mean	0.2219	6968.2838
3rd quartile	0.2414	7321.6169
Maximum	0.2939	11661.4642
Range	0.2319	6575.4569
Interquartile range	0.0267	1164.6118
Variance	0.0011	1310302.94
Standard deviation	0.0337	1144.6846
Skewness	-1.8109	1.5616
Kurtosis	6.9969	5.7657

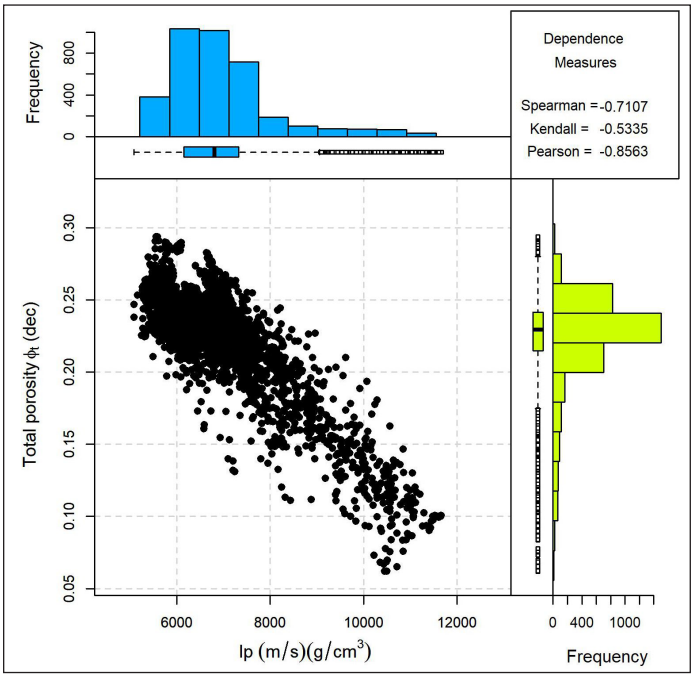

Figure 2. (Ip, ϕ_t) scatter plot and dependence measures.

The dependency measures and the scatter plot of (Ip, ϕ_t) is in Figure 2, this shows good dependence. The Spearman measure is -0.7107, Kendall -0.5335 and Pearson -0.8563

4.2 Variographic analysis

In this step the variogram of ϕ_t is estimated using three models: exponential, Gaussian, and spherical. The best model selected is spherical with sill 0.0011, range 16 meters and nugget 0 (Figure 3). This model will be used to obtain the simulations using the simulated annealing method.

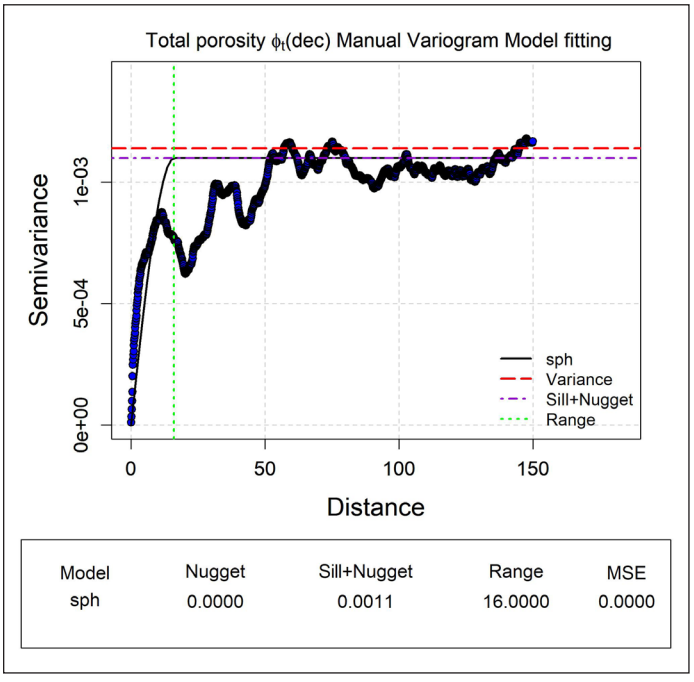

Figure 3. ϕ_t variogram model

4.3 Parametric modeling of the marginal CDF

The (lp, ϕ_t) samples are fitted in parametric probability distribution function that allows to represent it. The Akaike information criteria (AIC), Bayesian information criteria (BIC) and log-likelihood are used to select the best option.

4.3.1 Total porosity CDF modeling

For this variable, the gamma, beta, normal, logistic, lognormal and Weibull functions were tested. The goodness of fit results for ϕ_t is in Table 2 which shows the best option is Weibull function, followed by the normal function. As can see in the Figure 4, the functions cannot cover the entire histogram, only a large part of the central area, the lower values located to the left of the histogram are omitted Figure 4(A). This is confirmed in the cumulative histogram Figure 4(B), so it is possible that the results obtained in the simulation give greater importance to the largest values and not so much to the minimum values reported during the univariate analysis.

4.3.2 Acoustic impedance CDF modeling

This estimation uses the following functions: gamma, normal, logistic, lognormal and Weibull, the goodness of fit results for *Ip* is in Table 3, the best function for *Ip* is lognormal, gamma function is very close to lognormal and maybe that function could be a good option, however, the lognormal function is taken.

Table 2. Goodness of fit results for ϕ_t

Function	Parameter	Error	Parameter	Error	Likelihood	AIC	BIC
Weibull	$\alpha = 5.164$	0.129	$\lambda = 0.220$	0.0010	1791.958	-3579.91	-3569.90
Normal	$\mu = 0.205$	0.001	$\sigma = 0.040$	0.0010	1747.720	-3491.45	-3481.43
Logistics	$\mu = 0.210$	0.001	$\beta = 0.028$	0.0002	1735.720	-3467.45	-3457.44
Beta	$\alpha = 11.662$	0.489	$\beta = 45.080$	1.9240	1685.870	-3367.75	-3357.74
Gamma	$k = 13.994$	0.588	$\beta = 67.980$	2.9130	1660.400	-3316.80	-3306.79
Lognormal	$Log\mu$=-1.610	0.008	$Log\sigma$=0.280	0.0060	1598.540	-3193.09	-3183.08

Table 3. Goodness of fit results for *Ip*

Function	Parameter	Error	Parameter	Error	Likelihood	AIC	BIC
Lognormal	$Log\mu$=8.905	0.005	$Log\sigma$=0.190	0.004	-9562.235	19128.47	19138.48
Gamma	k=26.558	0.411	β=0.003	5.03e-5	-9586.137	19176.27	19186.28
Normal	μ=7513.696	45.850	σ=1521.670	32.406	-9647.394	19298.79	19308.80
Logistics	μ=7317.655	45.170	β=858.563	21.770	-9653.742	19311.48	19321.50
Weibull	α=4.963	0.108	λ=8153.500	52.592	-9710.083	19424.17	19434.18

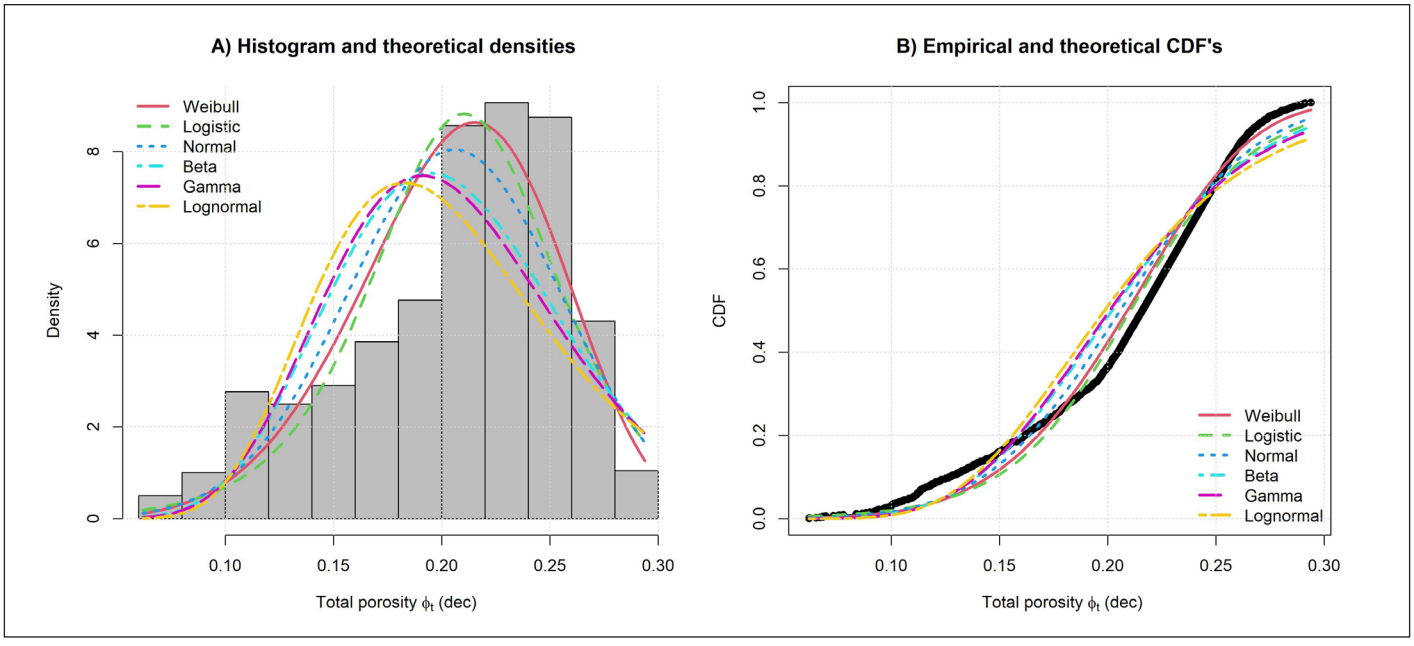

Figure 4. Histogram (A) and empirical CDF (B) with the best-fit probability functions for the total porosity ϕ_t

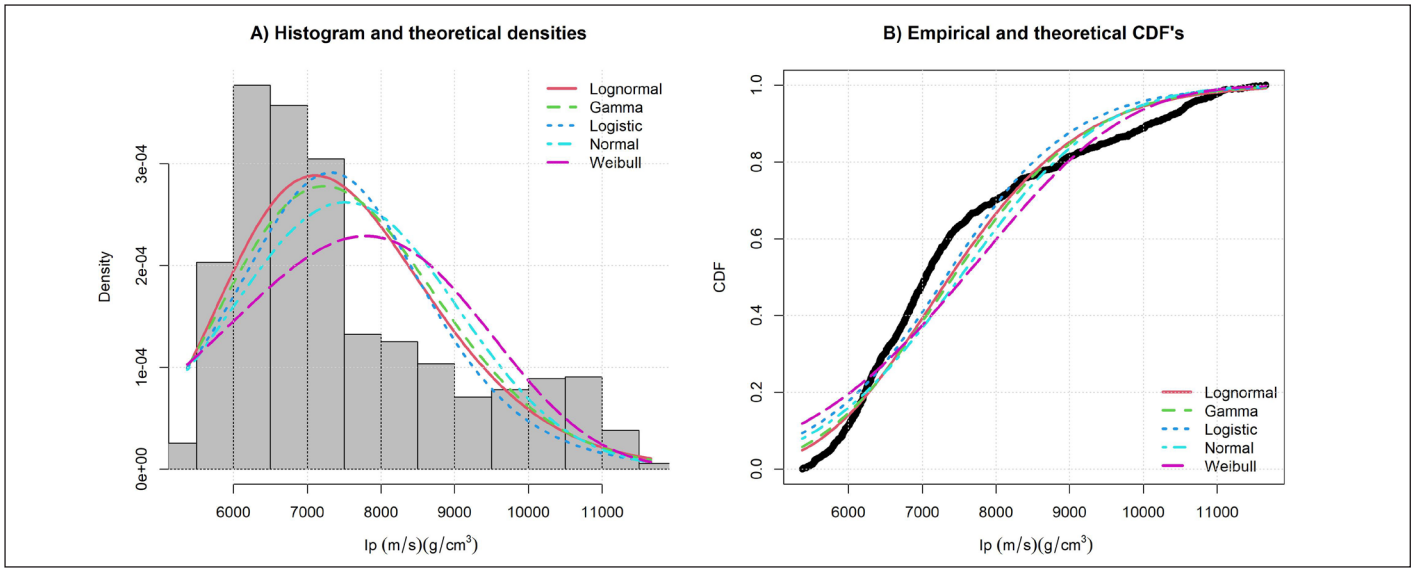

Figure 5. Histogram (A) and the empirical CDF (B) with the best-fit probability functions for the acoustic impedance Ip

Table 4. Fitted values for parameter θ

Copula	Method	Parameter θ	Error
Clayton	ITau	-0.86	0.006
Clayton	IRho	-0.92	0.006
Frank	ITau	-15.22	0.030
Frank	MLE	-15.04	0.443
Frank	IRho	-14.03	0.664

As ϕ_t variable, all functions fail to cover the entire histogram Figure 5(A). Notice that the highest values are not covered. If the cumulative histogram in Figure 5(B) is examined, the interval 6000 to 7000 has good approximation to empirical function.

4.4 Copula parametric modeling

After selecting the best-fit marginal probability functions, the best-fit parametric copula is sought. Considering the dependence model has negative dependencies, it is necessary to omit the Gumbel-Hougaard copula because it is not valid on negative dependencies, Clayton copula can be calculated in negative dependencies only if the parameter estimation method is semi-parametric, for this reason the Kendall inversion τ (ITau) and Spearman inversion ρ (IRho) is used. To select the best joint distribution function, the error or standard deviation and the graphs in the Figure 6 are used. Examining the information in Table 4, the best option is Clayton copula (Figure 6(A)). However, using this function could omit the values that are outside its coverage area, therefore the Frank's copula with the parameter estimated by maximum likelihood method (MLE) is used (Figure 6(B)).

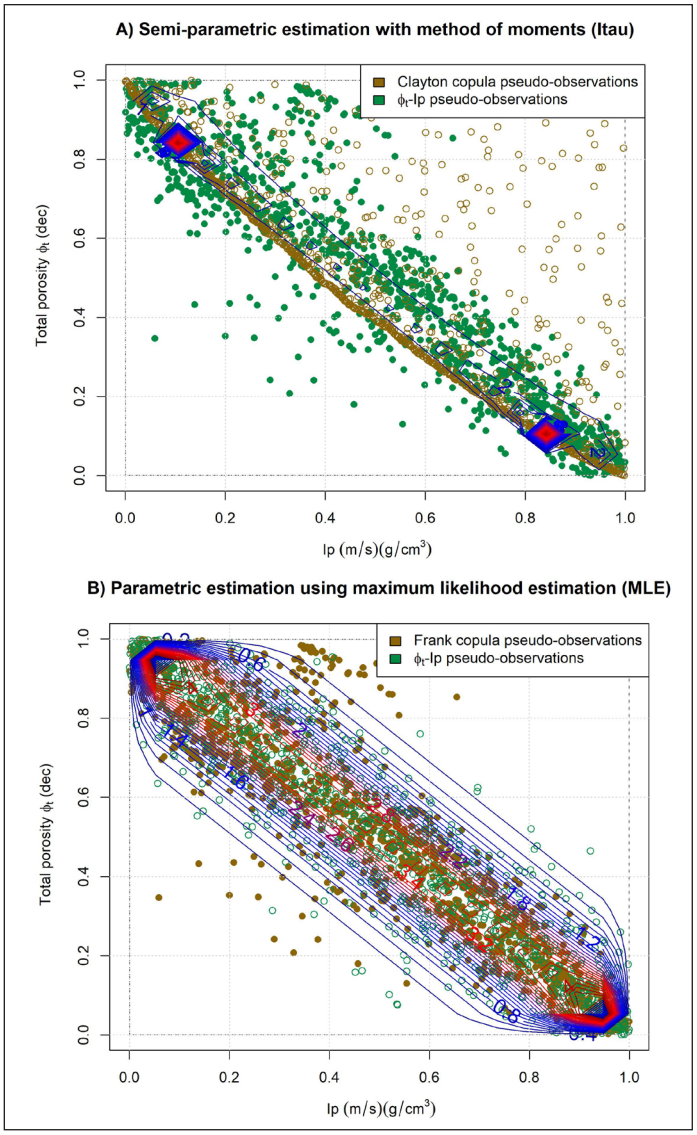

Figure 6. (A) Clayton copula, (B) Frank copula obtained with semi-parametric and parametric estimation.

4.5 Conditional joint simulation of total porosity with acoustic impedance.

After selecting the best parameters for the joint probability distribution function, a considerable number of pairs (Ip,ϕ_t) are simulated, it is proposed to simulate 40,000 observations based on the best estimate selected. The simulation samples under the parametric approach are very fast, less than a second. Considering the information in comparative Table 5, the case of ϕ_t simulated and ϕ_t variable has difference in the minimum values of 0.01 and maximum 0.007; in the case of mean and median, their differences are even lower. Therefore, it can be considered that the probability distribution function is representative. With the case of Ip, the difference in the minimum and maximum values have considerable differences, however, the mean and median values are very close to each other.

In comparison, the dependency measures obtained from the simulated samples appear to be quasi linear, however this may be due to the large number of samples. Regarding the comparison in the scatter plots (Figure 7), it is noted that the joint probability distribution function fails to adequately sample the area located in the interval Ip (10000,12000) ϕ_t (0.05,0.15). Sampling is abundant in the central part of the data sample (red dots), which is to be expected given the properties of Frank's copula (black dots).

Table 5. Comparative between (Ip, ϕ_t) data sample and simulated using parametric copula approach.

Statistics	ϕ_t	ϕ_t **simulated**	Ip	Ip **simulated**
Samples	3696	40000	3696	40000
Minimum	0.0620	0.0316	5086.0072	3018.2752
1st quartile	0.2147	0.1767	6157.0051	6492.1272
Median	0.2295	0.2089	6809.5573	7376.3306
Mean	0.2219	0.2065	6968.2838	7511.1841
3rd quartile	0.2414	0.2388	7321.6169	8377.4856
Maximum	0.2939	0.3548	11661.4642	15836.6388
Range	0.2319	0.3233	6575.4569	12818.3636
Interquartile range	0.0267	0.0620	1164.6118	1885.3584
Variance	0.0011	0.0020	1310302.9400	2099141.1700
STD	0.0337	0.0455	1144.6846	1448.8413
Skewness	-1.8109	-0.2597	1.5616	0.6097
Kurtosis	6.9969	2.9036	5.7657	3.7259

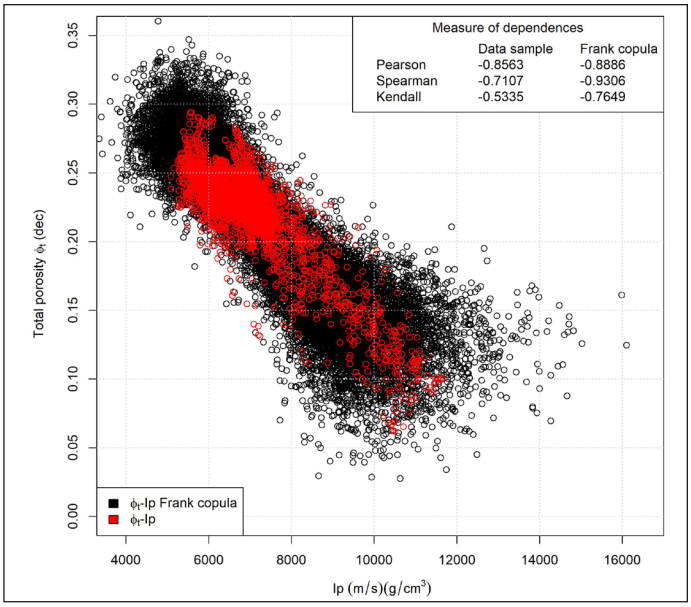

Figure 7. (Ip, ϕ_t) samples (red dots), (Ip, ϕ_t) simulated using parametric copula approach (black dots).

4.6 Total porosity spatial simulation

The total porosity ϕ_t is simulated using simulated annealing method, the GSLIB package (Deutsch & Journel, 1998) was used for the implementation. The variogram estimated for ϕ_t (Figure 3) is used as objective function and considered 100 realizations. The results are shown in the comparative Table 6. The minimum, maximum, mean and median values have low differences, not greater than 0.01.

Superimposing all realizations (Figure 8 (A)) dispersion in the interval 3200 to 3330 meters is noted.

5. Comparison between parametric, non-parametric and semi-parametric based copula simulations.

5.1 Non-parametric copula simulation.

The comparison with the non-parametric approach is made using a Bernstein copula for the estimation of the joint probability distribution function. The same data set (Ip, ϕ_t) is used for its implementation. As in the parametric case,

Table 6. Statistics obtained from ϕ_t data sample, 100 realizations, best realization and their differences using parametric approach.

Statistics	**ϕ_t data sample**	**ϕ_t 100 realizations**	**Difference 100 realizations**	**ϕ_t best realization**	**Difference best realization**
Samples	3696	369600		3696	
Minimum	0.0620	0.0541	0.0079	0.0707	-0.0087
1st quartile	0.2147	0.2071	0.0076	0.2071	0.0075
Median	0.2295	0.2284	0.0011	0.2284	0.0010
Mean	0.2220	0.2244	-0.0020	0.2244	-0.0024
3rd quartile	0.2414	0.2489	-0.0070	0.2487	-0.0072
Maximum	0.2939	0.3338	-0.0400	0.3102	-0.0162
Range	0.2319	0.2798	-0.0480	0.2394	-0.0075
Interquartile range	0.0267	0.0418	-0.0150	0.0416	-0.0148
Variance	0.0011	0.0014	-0.0003	0.0014	-0.0002
STD	0.0338	0.0375	-0.0040	0.0375	-0.0037
Skewness	-1.8110	-0.8640	-0.9470	-0.8750	-0.9364
Kurtosis	6.9970	4.2437	2.7533	4.2437	2.7532

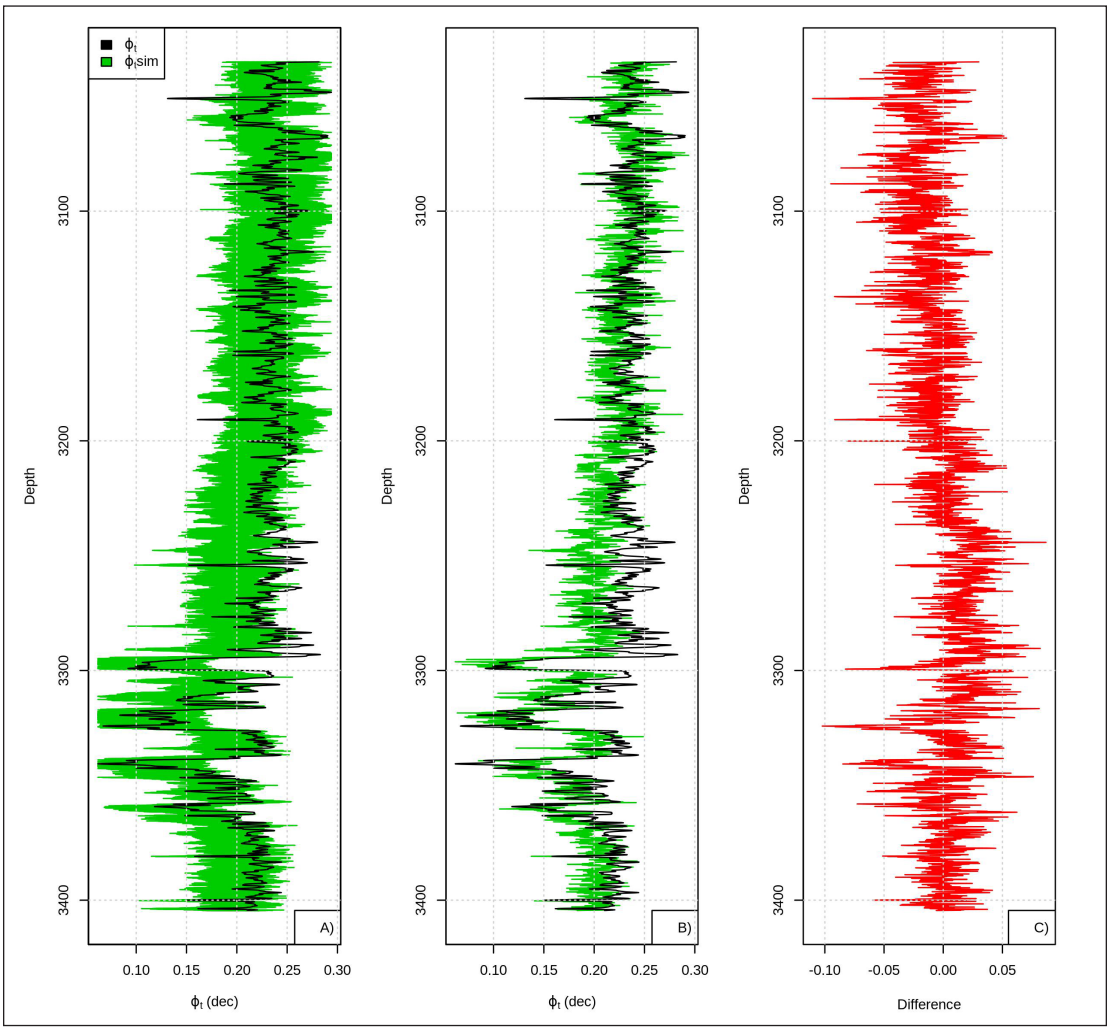

Figure 8. Well-log plots of A) 100 realizations of ϕ_t (green lines) with the well-log data values (black line), B) the ϕ_t best realization (green line) and C) the difference of the ϕ_t best realization with respect to the well-log data.

Table 7. Comparative between (Ip, ϕ_t) data samples and data simulated using non-parametric approach.

Statistics	ϕ_t	ϕ_t simulated	Ip	Ip simulated
Samples	3696	40000	3696	40000
Minimum	0.0620	0.0620	5086.0072	5086.0072
1st quartile	0.2147	0.2147	6157.0051	6157.0052
Median	0.2295	0.2295	6809.5573	6809.5574
Mean	0.2219	0.2220	6968.2838	6968.2839
3rd quartile	0.2414	0.2415	7321.6169	7321.6170
Maximum	0.2939	0.2938	11661.4642	11661.4642
Range	0.2319	0.2318	6575.4569	6575.4570
Interquartile range	0.0267	0.0268	1164.6118	1164.6118
Variance	0.0011	0.0011	1310302.9400	1309980.6378
Standard deviation	0.0337	0.0338	1144.6846	1144.5439
Skewness	-1.8109	-1.8212	1.5616	1.5617
Kurtosis	6.9969	7.0257	5.7657	5.7657

Table 8. Statistics obtained from ϕ_t data sample, 100 realizations, best realization and their differences using non-parametric approach.

Statistics	ϕ_t data sample	ϕ_t 100 realizations	Difference 100 realizations	ϕ_t best realization	Difference best realization
Samples	3696	369600		3696	
Minimum	0.0620	0.0620	0	0.0622	-0.0002
1st quartile	0.2147	0.2154	-0.0006	0.2154	-0.0006
Median	0.2295	0.2295	0	0.2294	0.0001
Mean	0.2220	0.2220	0	0.2220	0
3rd quartile	0.2414	0.2413	0.0001	0.2412	0.0002
Maximum	0.2939	0.2938	0.0001	0.2868	0.0071
Range	0.2319	0.2318	0.0001	0.2246	0.0072
Interquartile range	0.0267	0.0259	0.0008	0.0258	0.0009
Variance	0.0011	0.0011	0	0.0011	0
STD	0.0338	0.0330	0.0008	0.033	0.0008
Skewness	-1.8111	-1.9460	0.1349	-1.97	0.1590
Kurtosis	6.9970	7.4361	-0.4391	7.5698	-0.5728

40,000 samples using the Bernstein joint distribution function are simulated (Figure 11).

Each step takes around 10 hours, which compared to the time of parametric copula estimate, is too much. However, the statistics obtained from this estimate are very close to data samples (Table 7), this is confirmed in the Figure 11, the samples simulated using Bernstein copula (green dots) are close to data sample.

100 simulations using the samples obtained from Bernstein copula are made. As shown, the spatial distributions (Figure 9) obtained using the Bernstein copula are even closer to the data sample distribution. However, the computational cost is high, the simulation of 40,000 samples can take hours.

5.2 Semi-parametric copula simulation.

This is formed using Bernstein copula and parametric marginals, the marginals are Lognormal (Ip) and Weibull (ϕ_t). The statistics obtained are close for Ip; ϕ_t has differences, especially in minimum and maximum (Table 9). Comparing the scatter plot (Figure 11) the samples obtained with semi-parametric joint distribution function are between Frank copula and Bernstein copula. The computational cost

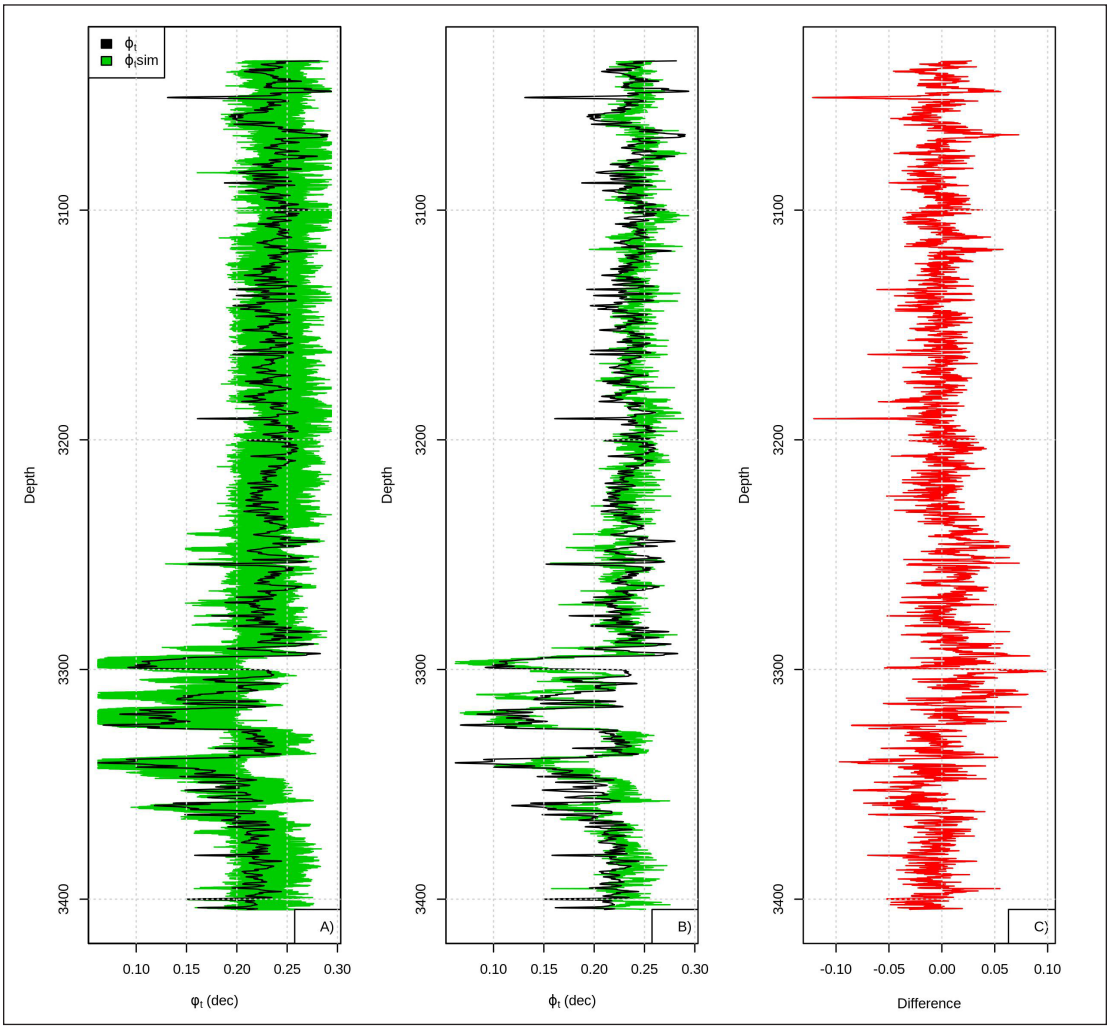

Figure 9. Realizations (green) superimposing over ϕ_t (black), B) Best realization obtained and C) difference between well-log ϕ_t and best simulated ϕ_t.

Table 9. Comparative between (Ip, ϕ_t) data sample and data simulated using semi-parametric approach.

Statistics	ϕ_t	ϕ_t **simulated**	Ip	Ip **simulated**
Samples	3696	40000	3696	40000
Minimum	0.0620	0.0298	5086.0072	5086.0072
1st quartile	0.2147	0.1967	6157.0051	6157.0052
Median	0.2295	0.2217	6809.5573	6809.5574
Mean	0.2219	0.2183	6968.2838	6968.2839
3rd quartile	0.2414	0.2459	7321.6169	7321.6170
Maximum	0.2939	0.3340	11661.4642	11661.4642
Range	0.2319	0.3042	6575.4569	6575.4570
Interquartile range	0.0267	0.0492	1164.6118	1164.6118
Variance	0.0011	0.0017	1310302.9400	1309983.8600
STD	0.0337	0.0411	1144.6846	1144.5453
Skewness	-1.8109	-0.6140	1.5616	1.5617
Kurtosis	6.9969	3.8246	5.7657	5.7657

is 10% less than the Bernstein copula, but the statistics are not the same.

Comparing the 100 ϕ_t simulations (Figure 10), the realizations are centered, this does not happen with the realizations obtained using Frank copula samples, but have more dispersion than the realizations obtained using the Bernstein copula samples, the statistics between data sample and data simulation are very close (Table 10).

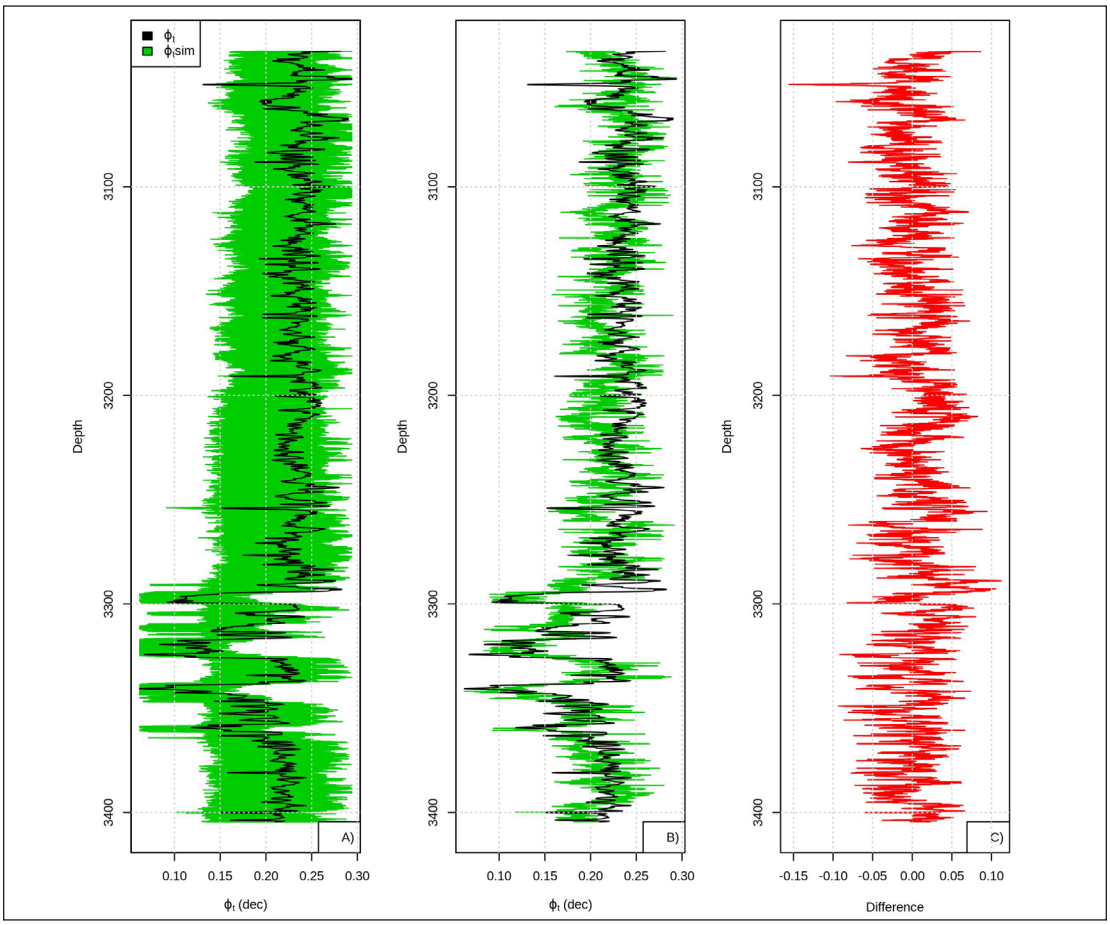

Figure 10. Realizations (green) superimposing over ϕ_t (black), B) Best realization obtained and C) difference between well-log ϕ_t and best simulated ϕ_t.

Table 10. Statistics obtained from ϕ_t data sample, 100 realizations, best realization and their differences using semi-parametric approach.

Statistics	**ϕ_t data sample**	**ϕ_t 100 realizations**	**Difference 100 realizations**	**ϕ_t best realization**	**Difference best realization**
Samples	3696	369600		3696	3696
Minimum	0.0620	0.0608	0.0012	0.0637	-0.0017
1st quartile	0.2147	0.1979	0.0168	0.1978	0.0169
Median	0.2295	0.2216	0.0079	0.2215	0.0080
Mean	0.222	0.2182	0.0038	0.2181	0.0039
3rd quartile	0.2414	0.2453	-0.0039	0.2456	-0.0042
Maximum	0.2939	0.3226	-0.0287	0.3054	-0.0115
Range	0.2319	0.2617	-0.0298	0.2418	-0.0099
Interquartile range	0.0267	0.0474	-0.0207	0.0479	-0.0212
Variance	0.0011	0.0015	-0.0004	0.0015	-0.0004
STD	0.0338	0.0383	-0.0045	0.0382	-0.0044
Skewness	-1.8110	-0.7330	-1.0780	-0.751	-1.0600
Kurtosis	6.9970	3.7493	3.2477	3.7789	3.2181

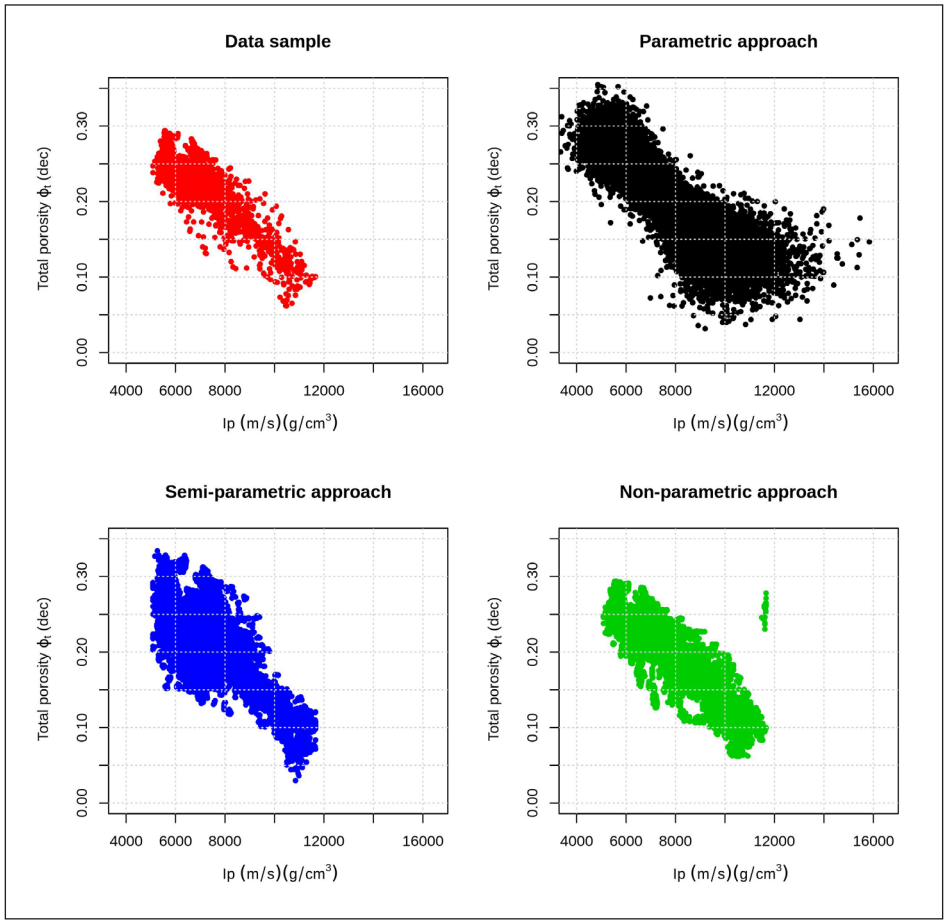

Figure 11. (Ip, ϕ_t) data samples (red dots), (Ip, ϕ_t) simulated using parametric copula (black dots), (Ip, ϕ_t) simulated using Semiparametric copula (blue dots) and (Ip, ϕ_t) simulated using non-parametric copula (green dots).

As shown in Table 11, the non-parametric approach almost perfectly reproduces the existing dependency relationship in the data sample, while the parametric and semi-parametric approaches either overestimate or underestimate it, respectively.

6. Application to case study: density vs. P- wave velocity

This example uses (Vp,ρ) well logs. The statistics (Table 15) and the histograms of Vp (Figure 12, blue histogram)

Table 11. Comparison of (Ip, ϕ_t) dependency measures among the parametric, semi-parametric and non-parametric approaches with respect to the data samples.

	Pearson	Spearman	Kendall
Data sample	-0.8563	-0.7107	-0.5335
Parametric approach	-0.8886	-0.9306	-0.7649
Semiparametric approach	-0.6780	-0.5074	-0.3671
Non-parametric approach	-0.8481	-0.7073	-0.5303

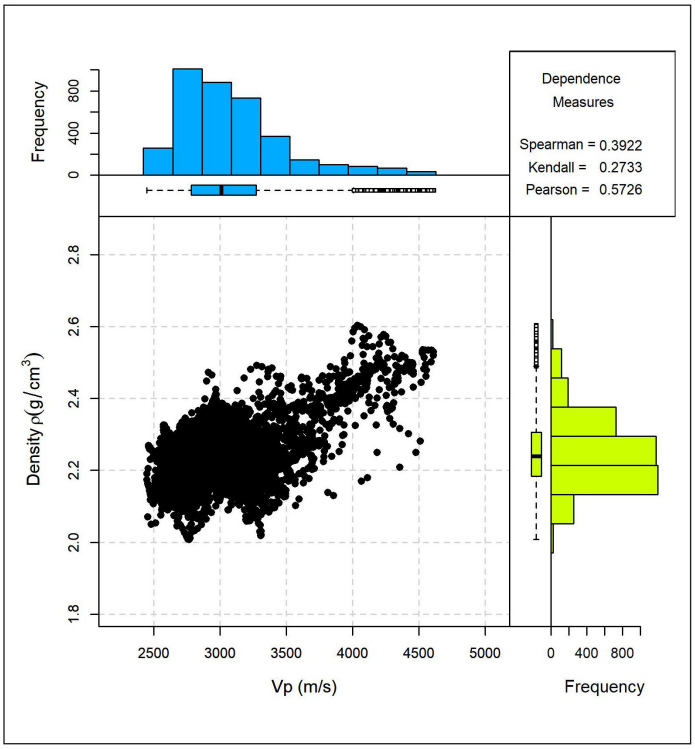

Figure 12. (Vp,ρ) Scatter plot, Vp histogram (blue) and ρ histogram (green).

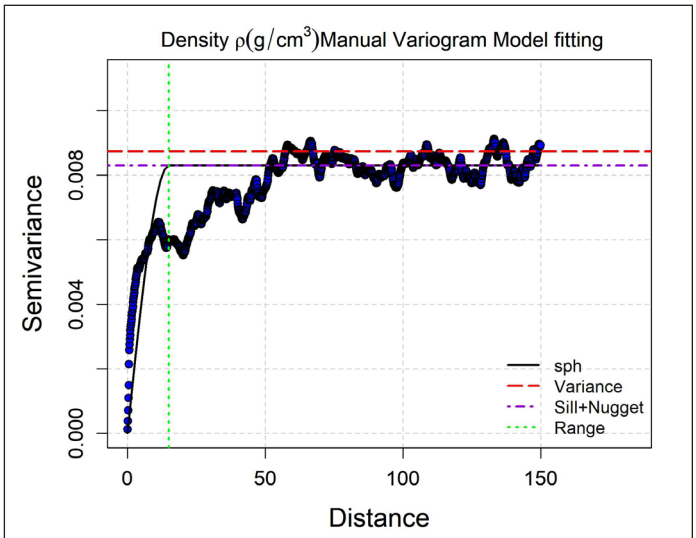

Figure 13. ρ variogram model

and ρ (Figure 12, green histogram) show high asymmetry although the difference between median and median is low in both variables. This case has positive dependence (Figure 12), but the dependence is less compared with the (Ip,ϕ_t) case. So, the use of Frank, Gumbel, Clayton and Joe copula is allowed.

The variogram model estimated for ρ (Figure 13) is spherical with sill 0.0083, range 15 meters and nugget effect 0.

The parametric estimation for ρ (Table 12) suggests the lognormal function as best option, but the cumulative distribution functions in Figure 14 (B) shows all functions, except Weibull function has good fit. Gamma and normal functions have likelihood, AIC and BIC very close to lognormal.

Now, the Vp variable goodness of fit results in Table 13 shows gamma function as best option, Logistic and lognormal are close to gamma function results, and the graphs in Figure 15 demonstrate that gamma and lognormal functions have similar fitted.

Table 12. Goodness of fit results for ρ

Function	Parameter	Error	Parameter	Error	Likelihood	AIC	BIC
Lognormal	$Log\mu$ =0.8130	0.009	$Log\sigma$ =0.04	0.006	1845.260	-3686.52	-3675.11
Gamma	k = 455.2500	13.650	β=201.60	6.050	1838.346	-3672.69	-3661.28
Normal	μ = 2.2581	0.002	σ = 0.10	0.001	1822.310	-3640.63	-3629.22
Logistics	μ = 2.2524	0.002	β = 0.06	0.001	1804.600	-3605.21	-3593.80
Weibull	α= 20.278	0.303	λ = 2.31	0.002	1568.410	-3132.83	-3121.42

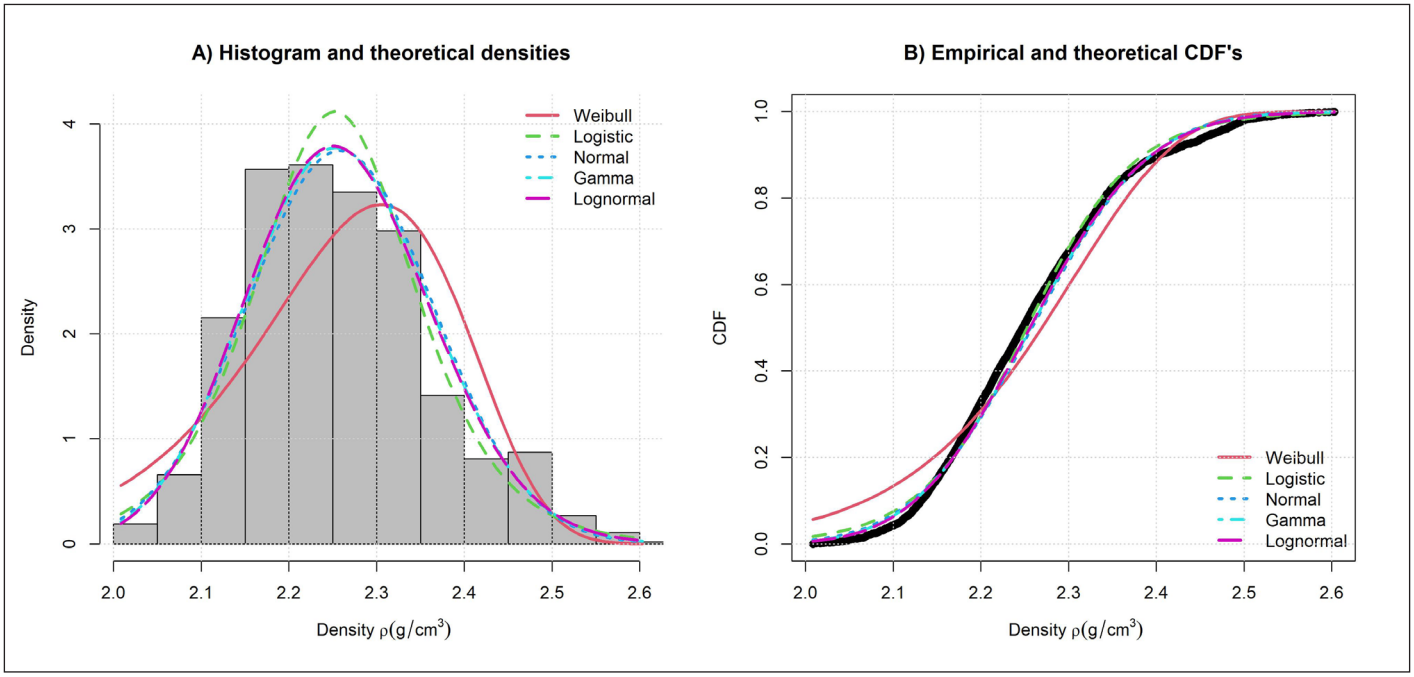

Figure 14. Histogram and theoretical densities (A) and empirical and theoretical CDF's (B) of Goodness of fit results for ρ

Table 13. Goodness of fit results for Vp

Function	Parameter	Error	Parameter	Error	Likelihood	AIC	BIC
Gamma	k = 58.244	1.440	β = 0.018	0.0004	-16500.00	33004.01	33015.42
Logistic	μ =3069.300	8.140	β = 224.63	4.0810	-16523.25	33050.51	33061.92
Lognormal	Logμ = 8.039	0.002	Logσ =0.12	4.0800	-16523.44	32902.89	32914.30
Normal	μ =3128.730	9.117	σ = 429.69	6.4470	-16617.57	33239.13	33250.54
Weibull	α= 6.628	0.096	λ = 3325.87	11.3400	-16903.62	33811.24	33822.65

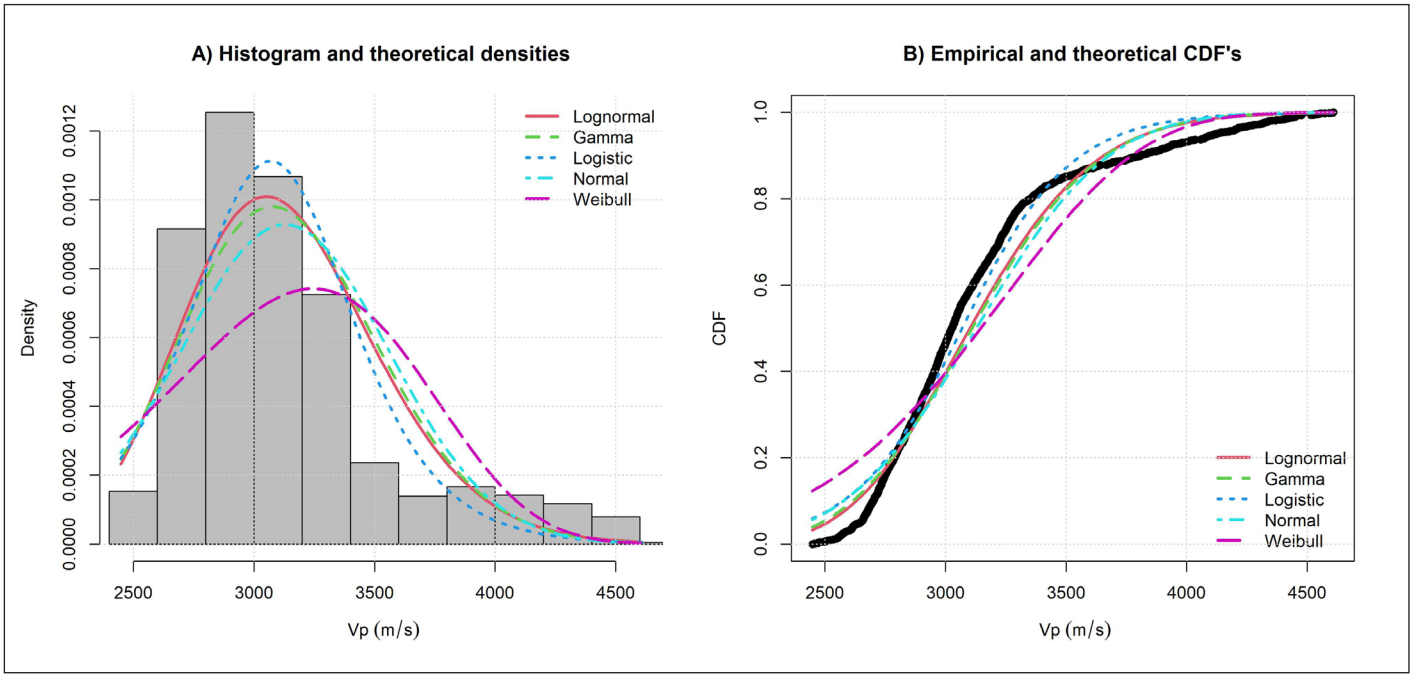

Figure 15. Histogram and theoretical densities (A) and empirical and theoretical CDF's (B) of Goodness of fit results for *Vp*

Table 14. Fitted values for parameter θ

Copula	Method	Parameter θ	Error	Loglikelihood
Joe	MLE	2.038	0.044	550.6
Gumbel	MLE	1.643	0.028	522.6
Frank	MLE	3.671	0.141	342.4
Clayton	MLE	0.570	0.035	170.2

The fit copula results show Joe copula model as best option (Table 14). Gumbel copula could be a good option, but Joe copula can cover the pseudo-observations, especially the samples in the extremes (Figure 16).

Simulating 40,000 samples from Joe copula, superimposing the results (Figure 17) the drop form of Joe copula samples is evident. The measures of dependences show Pearson values have difference of 0.02, but Spearman and Kendall measures are high. Other characteristic is the scatter of Joe copula samples, simulated samples are near to data samples. Comparing the variance and standard deviation in

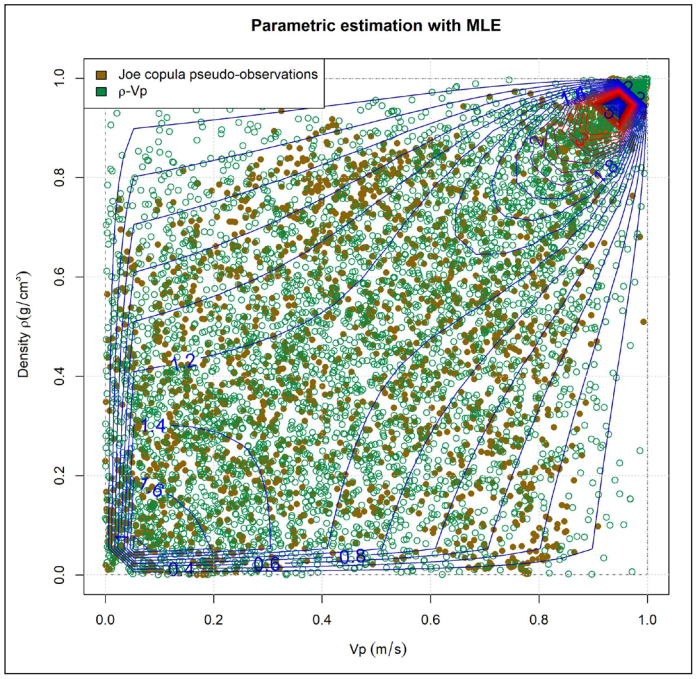

Figure 16. Joe copula estimated for (Vp,ρ)

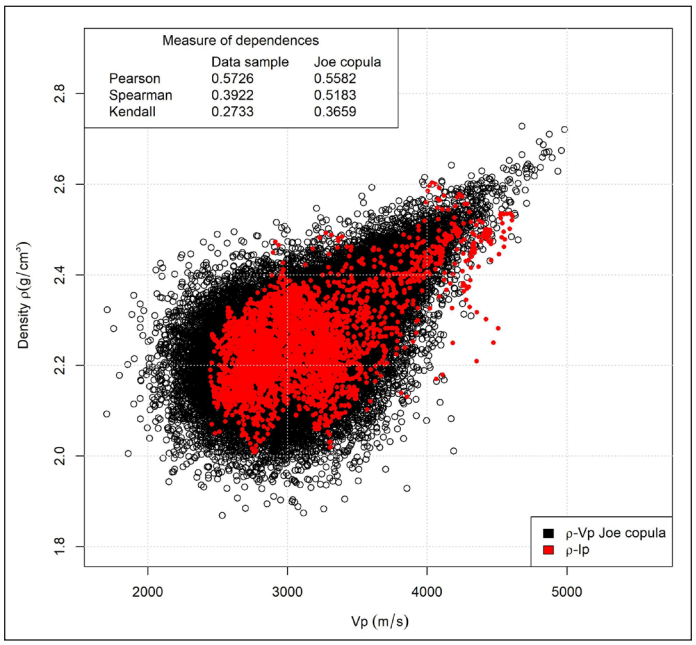

Figure 17. (*Vp, ρ*) samples (red dots), (*Vp, ρ*) simulated using Joe copula (black dots)

Table 15. Comparative between (*Vp, ρ*) data samples and simulated using Joe copula.

Statistics	***Vp***	***Vp* simulated**	***ρ***	***ρ* simulated**
Samples	3696	40000	3696	40000
Minimum	2448.0983	1619.7990	2.0085	1.8630
1st quartile	2785.1214	2843.1401	2.1835	2.1873
Median	3011.4426	3112.6668	2.2395	2.2568
Mean	3088.0889	3129.2969	2.2494	2.2590
3rd quartile	3273.1712	3398.5189	2.3062	2.3276
Maximum	4608.5457	5038.7143	2.6031	2.7328
Range	2160.4473	3418.9152	0.5946	0.8697
Interquartile range	488.0498	555.3788	0.1227	0.1402
Variance	165004.4920	168551.6370	0.0087	0.0110
Standard deviation	406.2074	410.5504	0.0934	0.1050
Skewness	1.2392	0.2460	0.6631	0.1302
Kurtosis	4.5799	3.0456	3.5973	3.0462

Table 15, the values are very close, this is not the same with the validation case, this could be an advantage of positive dependence.

The spatial distributions obtained to 100 simulations (Figure 18) show good covering except in the interval 3350-3400, the variance in that range is high.

7. Conclusions

In the comparison between parametric, semi-parametric and non-parametric approaches of the spatial stochastic simulation method based on copulas, it is concluded that the parametric approach has a very low computational cost, since its execution lasts only a few seconds; while the semi-parametric and non-parametric approach can take up to hours. Given that the first approach involves analytic functions in the calculation, while the second approach requires the calculation of the joint probability distribution function through the numerical approximation of the copula and its marginals with Bernstein polynomials.

When comparing the numerical results, it can be verified that the parametric approach does not reproduce data statistics such as minimum, maximum, skewness and kurtosis with the same precision as the semi-parametric and non-parametric approach. The parametric approach presents a greater dispersion expressed by its variance, which means more uncertainty. This fact is due to it is practically im-

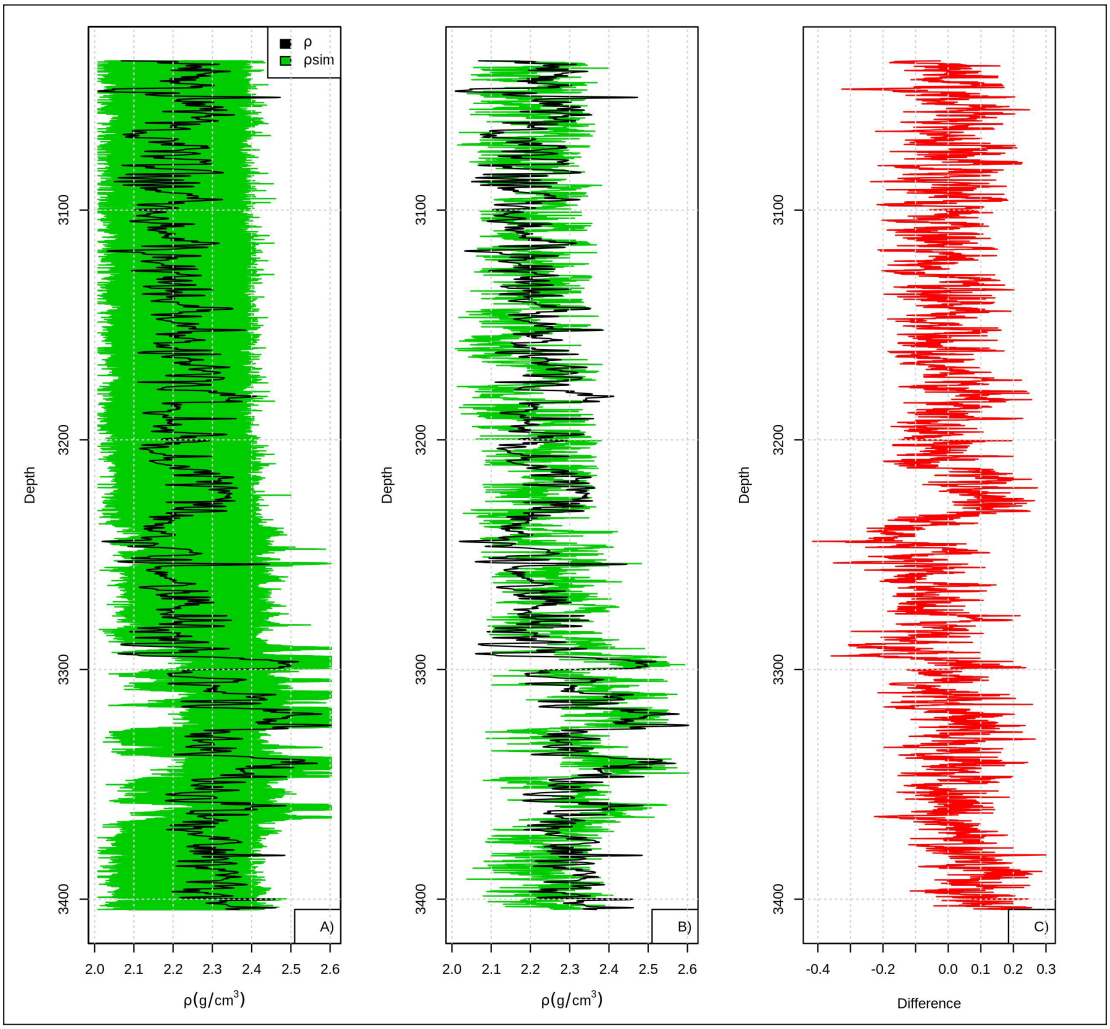

Figure 18. Realizations (green) superimposing over ρ (black), B) Best realization obtained and C) difference between well-log ρ and best simulated ρ.

possible to be able to represent the underlying dependence complexity between data with a parametric model, since the data is forced to fitting an analytical model depending of a single parameter, whereas the objective is to represent the real dependence complexity existing in the data, the latter only could be done by the non-parametric approach.

This indicates that it is advisable to use the parametric approach in cases with large data samples and limited computing capabilities. This problem would be expected to occur when the method is applied in three spatial dimensions and when more than two variables are included in the multivariate joint estimation as well. However, the non-parametric approach could be applied if the appropriate computational capabilities are available and predictions with less uncertainty are required.

8. Acknowledgments

The data were provided by the National Hydrocarbons Commission of Mexico, according to appendix C of the license to use the information in favor of Universidad Nacional Autónoma de México, dated December 11, 2017, under the nomenclature CNIH-C-00417.305. This reference information is the property of Mexico and its collection, safekeeping, use, administration and updating, as well as its publication is only authorized to the National Hydrocarbons Commission.

9. Supplementary material

A pdf version of Jupyter notebook in R language is available in **https://github.com/esmg-mx/Copula-Base-modelling**

10. Appendix

10.1 Appendix A: Copula definition and basic properties

As defined by Nelsen (2006), a copula is "*a function that joins or couples multivariate distribution functions to their one-dimensional marginal distribution functions*". If want to use copulas in the field of statistics, use Sklar's theorem. Sklar's theorem is defined as: *Let H be a joint distribution function with margins F and G. Then there exists a copula C such that for all (x, y) in R.*

$$H(x,y)=C(F(x),G(y)) \qquad \text{(Eq. A1)}$$

If $u=F(x)$ and $v=G(y)$ are marginal distribution functions and $C(u,v)=C(F(x),G(y))$ is a valid distribution function, then for any copula $C(u,v)$ its partial derivatives are $\frac{\partial C}{\partial u}$ and $\frac{\partial C}{\partial v}$ exist for almost all (u,v) in [0;1]. Then $\frac{\partial^2 C}{\partial u \partial v}$ and $\frac{\partial^2 C}{\partial v \partial u}$ exist and are continuous on I^2. If this is true, the density function of the copula is

$$C(u,v)=\frac{\partial^2 C}{\partial u \partial v} \qquad \text{(Eq. A2)}$$

And the joint probability density function of x and y is:

$$f(x,y)=\frac{\partial^2 (C)}{\partial u \partial v}\cdot\frac{dF}{dx}\cdot\frac{dG}{dy} \qquad \text{(Eq. A3)}$$

10.2 Appendix B: Bernstein copula simulation method

The Bernstein copula provides an estimate to the copula using the empirical copula and the Bernstein polynomials. If $F(x)$ and $G(y)$ are continuous, by elementary probability it is known that $U=F(X)$ and $V=G(Y)$ are continuous Uniform(0,1) random variables, and the underlying copula C for the random vector (U,V) is the same copula corresponding to (X,Y), and by Sklar's Theorem the joint probability distribution function for (U,V) is equal to $F_{UV}(u,v)=C(F(u),G(v))=C(u,v)$. Therefore, in case $F(x)$ and $G(y)$ are known and F_{XY} is unknown, if $\{(x_1, y_1),\ldots,(x_n, y_n)\}$ is an observed random sample from (X,Y), the set $\{(u_k,v_k)=(F_X(x_k),F_Y(y_k)) : k=1,\ldots,n\}$ would be an observed random sample from (U,V) with the same underlying copula C as (X,Y), and since $C=F_{UV}$ may use the (u_k,v_k) values (called copula observations) to estimate C as a joint empirical distribution:

$$\hat{C}(u,v)=\frac{1}{n}\sum_{k=1}^{n} 1_{\{u_k\le u, v_k\le v\}} \qquad \text{(Eq. B1)}$$

Strictly speaking, the estimation $\hat{C}$ is not a copula since it is discontinuous and copulas are always continuous. If F_X, F_Y, and F_{XY} are all unknown (the usual case), then F_X and F_Y are estimated by univariate empirical distribution functions:

$$\hat{F}_x(x)=\frac{1}{n}\sum_{k=1}^{n} 1_{\{x_k\le x\}} \qquad \hat{F}(y)=\frac{1}{n}\sum_{k=1}^{n} 1_{\{y_k\le y\}} \qquad \text{(Eq. B2)}$$

Now the set of pairs $\left\{(u_k,v_k)=\left(\hat{F}_X(x_k),\hat{F}_Y(y_k)\right): k=1,\ldots,n\right\}$ is referred to as copula pseudo-observations. It is straightforward to verify that $\hat{F}_X(x_k)=\frac{1}{n}rank(x_k)$ and $\hat{F}_Y(y_k)=\frac{1}{n}rank(y_k)$. In this case the concept of empirical copula, see (Nelsen, 2006), is defined as the following function $C_n : I_n^2 \to [0,1]$, where $I_n=\left\{\frac{i}{n}: i=0,\ldots,n\right\}$, given by:

$$C_n\left(\frac{i}{n},\frac{j}{n}\right)=\frac{1}{n}\sum_{k=1}^{n} 1_{\{rank(x_k)\le i,\ rank(y_k)\le j\}} \qquad \text{(Eq. B3)}$$

Again, C_n is not a copula but it is an estimation of the underlying copula C on the grid that may be extended to a copula on $[0,1]^2$ by means of, for example, Bernstein polynomials, as proposed and studied in Sancetta & Satchell (2004), which leads to what is known as a Bernstein copula non-parametric estimation $\tilde{C}:[0,1]^2\to[0,1]$ given by:

$$\tilde{C}(u,v)=\sum_{i=0}^{n}\sum_{j=0}^{n} C_n\left(\frac{i}{n},\frac{j}{n}\right)\binom{n}{i}u^i(1-u)^{n-i}\binom{n}{j}v^j(1-v)^{n-j} \qquad \text{(Eq. B4)}$$

As summarized in Erdely & Diaz-Viera (2010) in order to simulate replications from the random vector (X,Y) with the dependence structure inferred from the observed data $\{(x_1,y_1),\ldots,(x_n,y_n)\}$ it has the following:

Algorithm 1

1. Generate two independent and continuous Uniform(0,1) random variates u and t.
2. Set $v=c_u^{-1}(t)$ where $c_u(v)=\frac{\partial C(u,v)}{\partial u}$.
3. The desired pair is $(x,y)=(Q_n(u),R_n(v))$ where Q_n and R_n are empirical quantile functions for X and Y, respectively.

For a value x in the range of the random variable X and a given $0<\alpha<1$ let $y=\varphi_\alpha(x)$ denote the solution to the equation $P(Y\le y|X=x)=\alpha$. Then the graph of $y=\varphi_\alpha(x)$ is the α-quantile regression curve of Y conditional on $X=x$. In Nelsen (2006) is proven that:

$$P(Y\le y\,|\,X=x)=C_u(v)\Big|_{u=F_X(x),v=F_Y(y)} \qquad \text{(Eq. B5)}$$

This result leads to the following algorithm to obtain the α-quantile regression curve of Y conditional on $X=x$:

Algorithm 2

1. Set $c_u(v)=\alpha$.
2. Solve for v the regression curve, say $v=g_\alpha(u)$.
3. Replace u by $Q_n^{-1}(x)$ and v by $R_n^{-1}(y)$.
4. Solve for y the regression curve, say $y=\varphi_\alpha(x)$.

Bibliography

Arreguin-Lopez, M. A., Reyna-Martinez, G., Sánchez-Hernández, H., Escamilla-Herrera, A., & Gutierrez-Araiza, A. (2011). *Tertiary Turbidite Systems in the Southwestern Gulf of Mexico*.

Azevedo, L., & Soares, A. (2017). *Geostatistical Methods for Reservoir Geophysics*. Springer International Publishing. **https://books.google.fr/books?id=j_ShDgAAQBAJ**

Bortoli, L.-J., Alabert, F., Haas, A., & Journel, A. (1993). Constraining stochastic images to seismic data. In *Geostatistics Tróia'92* (pp. 325–337). Springer.

Bosch, M., Cara, L., Rodrigues, J., Navarro, A., & Díaz, M. (2007). A Monte Carlo approach to the joint estimation of reservoir and elastic parameters from seismic amplitudes. *Geophysics, 72*. **https://doi.org/10.1190/1.2783766**

Caers, J., Srinivasan, S., & Journel, A. G. (2000). Geostatistical Quantification of Geological Information for a Fluvial-Type North Sea Reservoir. *SPE Reservoir Evaluation and Engineering - SPE RESERV EVAL ENG, 3*. **https://doi.org/10.2118/66310-PA**

Chilès, J. P., & Delfiner, P. (1999). *Geostatistics: Modeling Spatial Uncertainty*. Wiley. **https://books.google.com/books?id=adkSAQAAIAAJ**

Cooray, K. (2018). Strictly Archimedean copulas with complete association for multivariate dependence based on the Clayton family. *Dependence Modeling, 6*(1), 1–18. **https://doi.org/10.1515/demo-2018-0001**

Cosentino, L. (2001). Integrated Reservoir Studies. In *Journal of Chemical Information and Modeling* (Vol. 53, Issue 9). **https://doi.org/10.1017/CBO9781107415324.004**

Deutsch, C. v., & Journel, A. G. (1998). GSLIB: Geostatistical software library and user's guide. In *New York* (Vol. 369). **https://doi.org/10.1016/0098-3004(94)90041-8**

Díaz-Viera, M. A. (2002). Geoestadística aplicada. *Instituto de Geofísica, 144*. **https://doi.org/10.1017/CBO9781107415324.004**

Díaz-Viera, M. A., Hernández-Maldonado, V., Méndez-Venegas, J., Mendoza-Torres, F., Le, V. H., & Vázquez-Ramírez, D. (2021). *RGEOESTAD: Un programa de código abierto para aplicaciones geoestadísticas basado en R-Project*. **https://github.com/esmg-mx/RGEOSTAD**

Díaz-Viera, M., Anguiano-Rojas, P., Mousatov, A., Kazatchenko, E., & Markov, M. (2006, April). Stochastic Modeling of Permeability in Double Porosity Carbonates Applying a Monte-Carlo Simulation Method With T-Copulas.

Díaz-Viera, M., & Casar-González, R. (2005). Stochastic Simulation of Complex Dependency Pattern of Petrophysical Properties Using T-copulas. GIS and Spatial Analysis - 2005 Annual Conference of the International Association for Mathematical Geology, IAMG 2005, 7.

Díaz-Viera, M., Erdely, A., Kerdan, T., del Valle, R., & Mendoza-Torres, F. (2017). Bernstein Copula-Based Spatial Stochastic Simulation of Petrophysical Properties Using Seismic Attributes as Secondary Variable (pp. 487–504). **https://doi.org/10.1007/978-3-319-46819-8_33**

Díaz-Viera, M., Le, V., & Vázquez-Ramírez, D. (2018). A Prediction of the Spatial Distribution of Petrophysical Properties with Bernstein Copula using Seismic Attributes as Secondary Variables. InterPore2018 New Orleans. **https://events.interpore.org/**

Dubrule, O., of Exploration Geophysicists, S., of Geoscientists, E. A., & Engineers. (2003). Geostatistics for Seismic Data Integration in Earth Models: 2003 Distinguished Instructor Short Course. Society of Exploration Geophysicists. **https://books.google.com/books?id=Lc3Ehp0ULd8C**

Erdely, A., Diaz-Viera, M., & Hernandez-Maldonado, V. (2012). Trivariate nonparametric dependence modeling of petrophysical properties.

Erdely Arturo and Diaz-Viera, M. (2010). Nonparametric and Semiparametric Bivariate Modeling of Petrophysical Porosity-Permeability Dependence from Well Log Data. In F. and H. W. K. and R. T. Jaworski Piotr and Durante (Ed.), Copula Theory and Its Applications (pp. 267–278). Springer Berlin Heidelberg. **https://doi.org/10.1007/978-3-642-12465-5_13**

Grana, D. (2014). Probabilistic approach to rock physics modeling. Geophysics, 79. **https://doi.org/10.1190/geo2013-0333.1**

Hernandez-Maldonado, V., Diaz-Viera, M., & Erdely, A. (2014). A multivariate Bernstein copula model for permeability stochastic simulation. Geofísica Internacional, 53, 163–181. **https://doi.org/10.1016/S0016-7169(14)71498-9**

Hofert, M., Kojadinovic, I., Mächler, M., & Yan, J. (2019). Elements of Copula Modeling with R. Springer International Publishing. **https://books.google.com/books?id=QxyDDwAAQBAJ**

Iturraran-Viveros, U., & Parra, J. (2014). Artificial Neural Networks applied to estimate permeability, porosity and intrinsic attenuation using seismic attributes and well-log data. Journal of Applied Geophysics, 45–54. **https://doi.org/10.1016/j.jappgeo.2014.05.010**

Jaworski, P., Durante, F., Härdle, W. K., & Rychlik, T. (2010). Copula Theory and Its Applications: Proceedings of the Workshop Held in Warsaw, 25-26 September 2009. Springer Berlin Heidelberg. **https://books.google.com/books?id=vX233feaA6MC**

Joe, H. (2014). Dependence Modeling with Copulas. Taylor & Francis. **https://books.google.com/books?id=09ThAwAAQBAJ**

Le, V. H. (2021). Copula-based modeling for petrophysical property prediction using seismic attributes as secondary variables [Universidad Nacional Autónoma de México]. **http://132.248.9.195/ptd2021/marzo/0810397/Index.html**

Le, V. H., Díaz-Viera, M. A., Vázquez-Ramírez, D., del Valle-García, R., Erdely, A., & Grana, D. (2020). Bernstein copula-based spatial cosimulation for petrophysical property prediction conditioned to elastic attributes. Journal of Petroleum Science and Engineering, 193, 107382. **https://doi.org/https://doi.org/10.1016/j.petrol.2020.107382**

Nelsen, R. B. (2006). An Introduction to Copulas. Springer New York. **https://books.google.com/books?id=yexFAAAAQBAJ**

Oh, S., & Kwon, B.-D. (2001). Geostatistical approach to Bayesian inversion of geophysical data: Markov chain Monte Carlo method. Earth Planets and Space, 53, 777–791. **https://doi.org/10.1186/BF03351676**

Parra, J., Iturraran-Viveros, U., Parra, J., & Xu, P.-C. (2014, April). Neural network and rock physics for predicting and modeling attenuation logs. **https://doi.org/10.1190/segam2014-0095.1**

Pyrcz, M. J., & Deutsch, C. v. (2014). Geostatistical Reservoir Modeling. OUP USA. **https://books.google.com/books?id=wNhBAgAAQBAJ**

Sancetta, A., & Satchell, S. (2004). The Bernstein copula and its applications to modeling and approximations of multivariate distributions. Econometric Theory, 20(3), 535–562. **https://doi.org/10.1017/S026646660420305X**

Shemyakin, A., & Kniazev, A. (2017). Introduction to Bayesian Estimation and Copula Models of Dependence. Wiley. **https://books.google.com/books?id=13gNDgAAQBAJ**

Trivedi, P., & Zimmer, D. (2007). Copula Modeling: An Introduction for Practitioners. Foundations and Trends(R) in Econometrics, 1(1), 1–111. **https://EconPapers.repec.org/RePEc:now:fnteco:0800000005**

Vázquez, D. (2018). Simulación estocástica conjunta de propiedades petrofísicas con cópulas de Bernstein usando atributos sísmicos como variables secundarias a escala de registros de pozo [Universidad Nacional Autónoma de México]. **https://repositorio.unam.mx/contenidos/80610**

Geofísica Internacional (2023) **62-2**: 507 - 517

Natural Gamma Ray Borehole Logging Technique for Estimating Radiogenic Heat Production in Basaltic Environment, Case study from Kodana region, Southern Syria

Jamal Asfahani[1*]

Resumen

Con el propósito de evaluar la producción de calor radiactivo (HP, por sus siglas en inglés) se han utilizado dos técnicas nucleares en un entorno basáltico de Kodana, en el sur de Siria. Estos son: sondeo de pozos para el registro de rayos gamma de origen natural (Ra) y espectrometría de rayos gamma. Las medidas de Ra se convierten a valores HP con base a la relación de Bucker y Rybach. La subestimación de los valores HP en el caso de estudio del sondo de pozos en Kodana señala la necesidad de una modificación de las constantes de la relación de Bucker y Rybach (0.0158 y 0.8). Por ello se propone establecer una nueva ecuación de la siguiente forma: HP(μW/m^3)= 0.037 (Ra(API)+ 4.35, más adecuada para caracterizar HP en ambientes basálticos continentales. Además, su eficacia se ha validado con la estimación y análisis del HP en tres pozos adicionales en la región de estudio. El análisis de 377 puntos medidos a lo largo del pozo Kodana muestra que el Ra varía entre 4.93API y 9.31API, con un valor promedio de 6.83API, mientras que el HP corregido y calibrado varía entre 0.32 y 0.51 μW/m^3, con un valor promedio de 0.42 μW/m^3.

Utilizando multifractales número-concentración y gráficas log-log se distinguen cuatro rangos de valores de HP calibrados en la región de estudio. El primer rango (<0.354μW/m^3) está relacionado con basalto denso y masivo; el segundo (0.354–0.41μW/m^3) con basalto sólido; el tercero (0.41–0.44μW/m^3) con basalto piroclástico, y el cuarto (>0.44μW/m^3) con productos de alteración del basalto y arcillas.

Palabras Clave: Producción de calor radiactivo, Técnica de registro de pozos de rayos gamma naturales, Basalto en el sur de Siria

Abstract

Two nuclear techniques are used to evaluate the radioactive heat production (HP) in a basaltic environment in the Kodana region, Southern Syria: natural gamma ray borehole logging (Ra) and spectrometry gamma ray. The Ra measurements are converted into (HP) values based on the Bucker and Rybach relationship. The underestimated HP values obtained in this case study of Kodana well require therefore a modification of the Bucker and Rybach relationship constants (0.0158 and 0.8). A new equation is thereafter established and proposed as follows: HP (μW/m^3) = 0.037* Ra(API) + 4.35. This equation is more suited to characterize HP in continental basaltic environments. The proposed equation is validated and has proven its efficacy through estimating and analyzing the HP in three additional boreholes in the study region. The analysis of 377 measured points along the Kodana borehole shows that Ra varies between 4.93API and 9.31API, with an average value of 6.83API, while the corrected and calibrated HP varies between 0.32 and 0.51 μW/m^3, with an average value of 0.42 μW/m^3.

Four calibrated HP ranges were isolated in the study region using the multi-fractal concentration number and log-log graphs. The first range (<0.354 μW/m^3) is related to hard massive basalt, the second (0.354 - 0.41 μW/m^3) is related to hard basalt, the third (0.41 - 0.44 μW/m^3) is related to pyroclastic basalt, and the fourth (> 0.44 μW/m^3) is related to basalt alteration products and clay.

Keywords: Radioactive heat production, Natural gamma ray borehole logging technique, Basalt Southern Syria

Received: June 6, 2022; Accepted: November 11, 2022; Published on-line: April 1, 2023.

Editorial responsibility: Michel Monnin

* Corresponding author: Jamal Asfahani
[1] Geology Department, Atomic Energy Commission of Syria, P.O.Box. 6091, Damascus- Syria.

https://doi.org/10.22201/igeof.2954436xe.2023.62.2.1588

1. Introduction

The radiogenic heat production (HP), an important parameter, is produced in the rocks through the decay of radioactive elements such as uranium, thorium and potassium. The heat production rate of a given rock can be therefore computed based on the concentrations of those radioactive elements and the density rocks (Rybach, 1988). The HP parameter has a considerable effect on the temperature distribution (Black Well and Steele, 1989), where its importance is evident in the modeling of deep sedimentary basins and in the heat-flow studies (e.g. Deming *et al.*, 1990). The heat-flow variations within a sedimentary basin are essentially due to the changes in radiogenic heat production of the underlying basement.

This paper deals with the characterization and identification of the radiogenic heat production in basaltic environments by using two different nuclear techniques, particularly, the natural gamma ray borehole logging, based on the use of Bucker and Rybach relationship, 1996, and the gamma ray spectrometry techniques.

Bucker and Rybach relationship, 1996, directly relates the gamma ray log records with the radioactive heat production. Asfahani, 2018, and 2022 evaluated the heat production in Area-1 and Area-2 in Syria respectively, applying the aerial spectrometry gamma ray technique. Asfahani (2019a) also applied the spectrometry gamma ray technique on 748 rock samples taken from Syrian territory to estimate their heat production and to map its spatial distribution on a constructed map. Asfahani, 2019-b, used the natural gamma ray well logging technique to evaluate the heat production in the phosphatic Khneifis deposit in Syria. Asfahani *et al.*, 2021, applied also this technique to characterize laterally and vertically the radioactivity (Ra) and the heat production in Banting district, SW of Malaysia, based on the Bucker and Rybach relationship. They explained that the high radioactivity and heat production ranges are mainly related to the silty clay layers, bearing uranium and thorium.

Prior to this research work, no available data on radiogenic heat production existed for the basaltic environments in Syria. Thus, it is timely to get the order of magnitude of this radioactive heat production parameter for different basaltic litho-types. The data reported here may also be useful for future thermal studies in neighboring areas.

The main objective of this paper is therefore to evaluate the radioactive heat production parameter (HP) in the study region, as a function of depth, concentrating mainly on the available Kodana borehole.

The API unit is required to be used for the gamma ray intensity in the Bücker and Rybach relationship. The counts per second (cps) unit of the measured natural gamma ray borehole logging records must be therefore converted into API units.

A new adapted equation is established and proposed in this paper to estimate the heat production in basaltic environments, where the use of Bücker and Rybach (1996) equation gives underestimated values of the heat production HP for such basaltic environments.

The log-log graph related to the concentration-number (C-N) model is used to identify the different ranges of both, the measured natural gamma ray (Ra) and the computed (HP) parameters in the Kodana study region. Those Ra and HP ranges reflect the vertical boundaries of the different lithologies traversed by the study borehole.

The following is achieved in this paper:

1. Evaluating the radioactive heat production (HP) as a function of depths along the study boreholes in the Kodana region by using the available natural gamma ray logs.
2. Evaluating the radioactive heat production (HP) of the rock samples taken from different depths of the Kodana borehole, applying the gamma ray spectrometry technique in laboratory.
3. Validating and proving the accuracy of the new equation proposed for HP estimation in three additional boreholes available in the study region.
4. Determining the main statistical characteristics of the measured natural gamma ray borehole logging records and the computed radioactive heat production in the analyzed boreholes, particularly the Kodana one (Min, Max, Mean, and standard deviation σ).
5. Assessing the different population ranges of both, the measured natural gamma ray logging records, and the computed HP parameters in the Kodana region through a fractal approach.

2. Field work

Nuclear and electrical borehole logging techniques were used to log four drilled boreholes of depths varying between 190 and 300m in Southern Syria; their locations are shown in the Figure 1. A Digital Robertson geology borehole logging station was used for executing and acquiring the borehole logging records.

The present paper focuses mainly on the results obtained at the Kodana borehole, as similar borehole logging results have been obtained in the other three boreholes.

Figure 2 shows the different logs obtained in the Kodana borehole. Those logs include the natural gamma ray (cps), the density LSD log (g/cm^3), the porosity (%), and the short and long normal resistivity (Ohm-m) (Asfahani, 2011). The logs shown in Figure 2 cover only the saturated Neogene basalt aquifer from a depth of 110m. The water level and the interface between the saturated and non-saturated zones were already determined by neutron-porosity logs (Asfahani, 2011), as shown in Figure 3. The lithological description

of the traversed layers in the saturated basaltic zone, shown in the right side of Figure 2 was established according to the different mentioned borehole logging results and their statistical treatment (Asfahani, 2011).

Four kinds of basalts have been identified in the study region based on the adapted threshold concepts and the above-mentioned nuclear and electrical logs (Asfahani, 2011). Those basalt types are as follows:

- Hard massive basalt.
- Hard basalt.
- Pyroclastic basalt.
- Alteration basalt products, clay.

3. Nuclear techniques for estimating heat production

Two nuclear techniques are used in this paper to evaluate the radioactive heat production in a basaltic environment (Richardson and Killeen, 1980; Thompson *et al.*, 1996; Bücker and Rybach, 1996; Salem *et al.*, 2005; Asfahani 2018; Asfahani, 2019a, and Asfahani, 2019b). The first one is the natural gamma ray borehole logging technique, and the second is the gamma ray spectrometry applied on basaltic rock samples.

3.1 Natural gamma ray borehole logging technique- Ra and API unit

The natural gamma ray (Ra) log is a continuous measurement of the natural radioactivity radiated from the lithological formations traversed by the logged borehole. This radioactivity is due to the presence of the potassium-40, uranium, and thorium (K40, eU, eTh). The used sensitive detectors were able to count the number of gamma rays per unit of time. The equipment used to record the (Ra) logs is a RG PC-logger system II. The length of the winch is 500 m. The gamma probe dimensions are 2.4 m length and 4.4 cm diameter. The gamma detector is the sodium iodide (Thallium doped) scintillation crystal, with a dead time of 4 micro seconds (Robertson geo-logging, 1993).

It is to mention that the location of the drilled Kodana well of GPS coordinates (E: 3589614, N: 3301961 and Z: 770m) was determined by the author (Asfahani, 2022a).

The gamma-ray intensity was measured by the unit of count per second (cps). The American Petroleum Institute has already adopted the "API" as a gamma ray unit to obtain a standard unit for gamma ray log measurements. One API Gamma ray unit is determined as 1/200 of the difference between the low and high gamma ray radiation values measured in (cps) in the calibrated pit. The calibration relationship between cps and API is written as follows (Lashin, 2005):

$$API = 1/200 * \Delta \text{ (high- low (cps))} \quad (1)$$

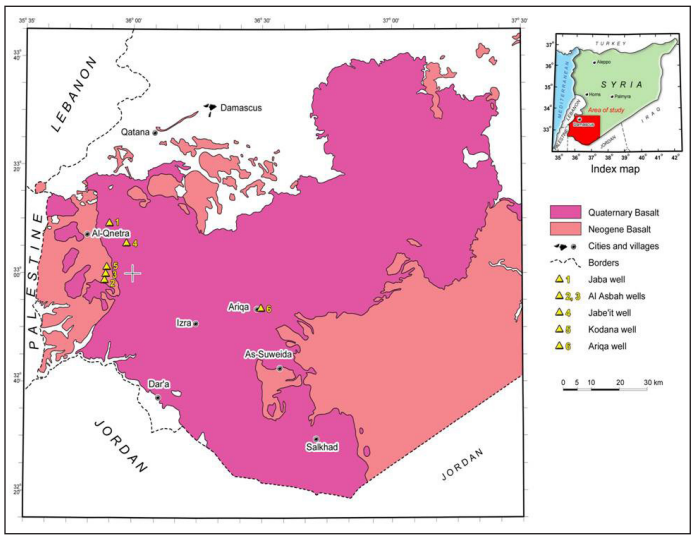

Figure 1. Geology of the study region and the location of the drilled boreholes.

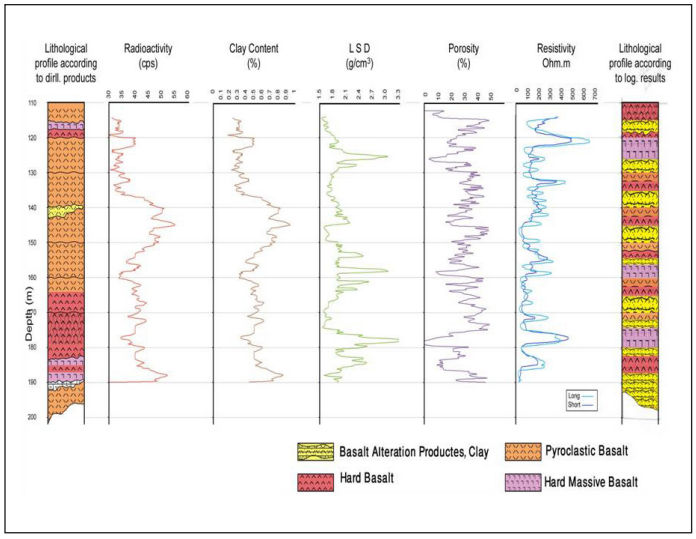

Figure 2. Nuclear and electrical logging records with lithological description of the Kodana borehole.

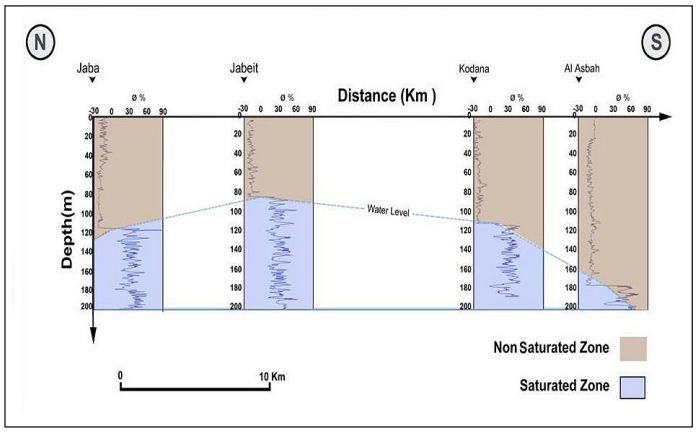

Figure 3. The water level and the interface between saturated and non-saturated zones in the study region, Southern Syria (Asfahani, 2011).

The high measured value in the analyzed Kodana well is 56 cps, the low measured value is 20 cps. Using these numbers in equation (1), 0.18 cps is about 1 API.

3.2 Spectrometric gamma ray technique

The gamma spectrometer consisted of a 12.5% relative efficiency Ge detector, with an energy resolution of 1.8keV at 1.333MeV, coupled to an S-100 spectroscopy system with an 8192 ADC card. The gamma ray measurements were realized in a 10 cm thick lead shield covered internally with a 1 mm thick copper sheet. The calibration of the gamma spectrometer for U, Th, and K analysis was achieved with the use of the standard reference materials RGTh and RGU related to IAEA, which were counted under the same conditions as ore samples (AQCS, 1995). The GaNAAS (Gamma and Neutron Activation Analysis Spectrum) PC program was used to analyze the gamma spectra (Nuclear Analysis Software, 1991). This is an indirect spectrometric gamma counting technique that gives U analysis as eU analysis. The term eU is widely used to indicate an equivalent uranium, and is equal to the true uranium only if the rock sample analyzed is in a radioactive equilibrium state, (Asfahani, 2002). Nineteen rock samples taken from different depths of the Kodana borehole were analyzed using this technique to determine U, Th and K contents of the studied basaltic section. Four basaltic rock samples were used for computing the radioactive heat production (the other fifteen rock samples were not used, being located in the unsaturated basaltic aquifer above 110m).

The evaluation of the radioactive heat production (HP) on the rock samples requires the knowledge of the concentrations of the radioelements (eU, eTh, and K%) (Fernandez *et al.*, 1998) and the density of the rock samples (ρ) (Asfahani, 2019a), where the following empirical equation is used (Rybach, 1976):

$$HP\ (\mu w/m^3) = \rho * Y \qquad (2)$$

Where $Y = (0.0952\ eU + 0.0256\ eTh + 0.0348\ K\%)$

In which, ρ (g/cm^3) in equation (2) is the dry density of the sample rock, eU (ppm), eTh (ppm), and K (%) are the concentrations of uranium, thorium, and potassium respectively.

Equation (2) gives the energy released during alpha, beta, and gamma decay of the radioelements (Rybach, 1976; Rybach, 1976a; and Birch, 1954). The alpha decay of the uranium is the main source of radioactive heat production (Birch, 1954), unlike thorium and potassium that have only a limited contribution.

The natural gamma spectrometry tool (NGS) and the density tool (LTD) can be also used together to estimate the radioactive heat production along the boreholes. The knowledge of the (eU, eTh, K%) and the density (ρ) allows consequently to compute the radioactive heat production from equation (2).

However, the gamma spectrometry borehole logging tool is not always available, while the natural gamma-ray logging tool (Ra) is available and can be used in a huge number of exploration boreholes over the world. The natural gamma ray (Ra) log reflects generally the sum of uranium, thorium, and potassium existed at a given depth in the study borehole, as represented by Y in equation (2).

Bücker and Rybach in 1996 already established an empirical direct linear relationship between the logging (Ra) intensity evaluated in API unit, and the radioactive heat production (HP) (μw/m^3), as follows:

$$HP\ (\mu W/m^3) = 0.0158\ (Ra\ (API) - 0.8) \qquad (3)$$

Equation (3) was established and derived through a collected data set from the research boreholes Sancerre-Couy/F, Soultz/F, BALAZUC-I/F, KTB/D, ODP 834B (Ocean Drilling Program), and three different NAGRA-holes/CH (Bücker and Rybach, 1996). It is applicable only for a radioactivity range of 0 to less than 350 API. It is often suitable to be applied in different sedimentological and geological environments, and gives reasonable results within an error of less than 10% (Bücker and Rybach, 1996). As much as the K/eU and eTh/eU ratios are closer to the mean characteristics values of the continental crust, as much as the error is lower (Bücker and Rybach, 1996).

The radioactive heat production HP is evaluated in the Kodana borehole study, based on equation (3). HP is also evaluated in three additional available boreholes in the study region (Jaba, Jabeit, and Al-Asbah), using a new proposed equation more suitable for characterizing the continental basalt than the one of Bücker and Rybach, 1996.

3.3. Fractal technique and concentration number mode (C-N)

A log-log graph with the concentration-number (C-N) multifractal model is used to determine the straight line segments and the break thresholds points, that we use as vertical boundaries to separate between different anomalous ranges (Afzal *et al.*, 2010; Zuo 2011; Wang *et al.*, 2011, Mohammadi *et al.*, 2013). This technique is applied herein on the measured natural gamma ray logs (Ra), and on the related computed corrected radioactive heat production (CHP) parameters for the Kodana region to distinguish different ranges of Ra and HP anomalies.

The equation describing the concentration-number (C-N) fractal model is as follows:

$$N(\geq \mu) = F\ \mu^{-D} \qquad (4)$$

Where μ is the treated geophysical parameter values, which are in this paper the (Ra) in API unit, and the corrected radioactive heat production (CHP) (μW/m^3). N(≥μ) is the cumulative number of the analyzed geophysical data, which are the cumulative number of the measured natural gamma ray logs (CNRa), and the cumulative number of the computed radioactive heat production (CNCHP), with the geophysical parameter values greater than or equal to μ; D is the scaling exponent or fractal dimension of the distribution of geophysical parameter values and F is a constant.

4. Results and Discussion

Natural gamma ray borehole logging technique was applied on the available four drilled boreholes in the Kodana region (Asfahani, 2011). The cps unit of the natural gamma ray records (Ra) presented for Kodana well, shown in Figure 2 is converted in this paper to API units. Figure 4 shows the variation of Ra along the Kodana borehole.

It is clear from Figure 4 that Ra intensity varies between 4.93 and 9.31 API with an average value of 6.83 API.

The quation (3) of Bücker and Rybach, 1996, presented above, is used to evaluate the radioactive heat production HP along the Kodana studied borehole. Figure 5 shows therefore a representative example on the radioactive heat production variations log (LHP) obtained along the Kodana borehole.

The main and high (LHP) layer is concentrated at depths between 140 and 155m, due to the presence of a basalt alteration products, and clay at this range of depths.

The (LHP) values obtained with the Bücker and Rybach technique (1996) shown in Figure 5 are underestimated in comparison with the literature HP values obtained in similar continental basalt areas particularly in the Northeast of German basin (where the HP for the basaltoides is ranged between 0.1 and 0.7μW/m^3) (Ben Norden and Forster, 2006); Hasterok *et al.*, 2018; and Asfahani, 2019a.

Abady *et al.*, 2004 has already reported the mean radioactive heat production of 0.11 μW/m^3 for the basalt of Eastern desert, Egypt, and compared also with other published data such as 0.80 μW/m^3 for the basalt from Japan, and 0.39 μW/m^3 for the basalt former USSR.

The (LHP) underestimation in this specific case study of Kodana well can be explained by the considerable radioactive difference between the continental rock samples basalt of the study region, and those used for the calibration of Bücker and Rybach technique, 1996. Those authors

declared that as much the K/eU and eTh/eU ratios of the analyzed rock samples are closer to the mean characteristic values of the continental crust, as much the error in evaluating the radioactive heat production is lower (Bücker and Rybach, 1996).

The radioactive heat production (HP) is also computed on four different basaltic rock samples taken from different depths of the Kodana borehole, to get the real and corrected heat production (CHP) of the basaltic layers in the study region. The results of those four rock samples analysis are shown in Table 1. The values of (CHP) for those rock samples

Table 1. Corrected radioactive heat production (CHP) of the basaltic rock samples taken from Kodana borehole.

Number	Depth (m)	eU (ppm)	eTh (ppm)	K%	Density (g/cm^3)	CHP μW/m^3	LHP μW/m^3
1	110	1.48	2.11	0.49	1.55	0.33	0.07
2	115	1.35	3.4	0.55	1.57	0.37	0.076
3	130	1.29	2.45	0.71	1.818	0.38	0.079
4	170	1.75	2.85	0.67	1.6	0.42	0.098

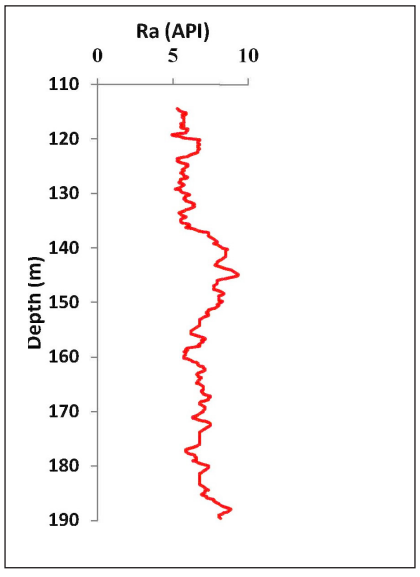

Figure 4. Natural gamma ray log Ra along the Kodana borehole.

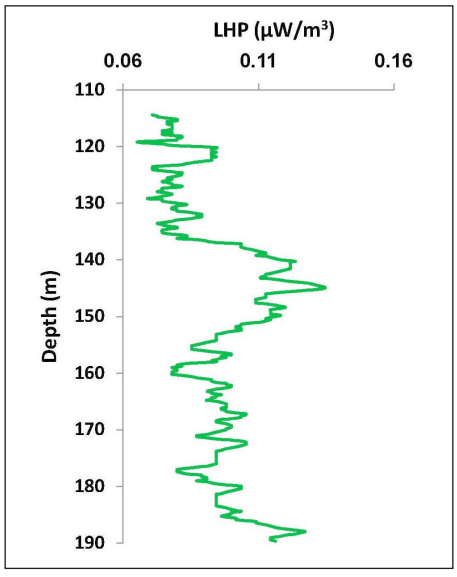

Figure 5. Radioactive heat production log (LHP) along the Kodana borehole.

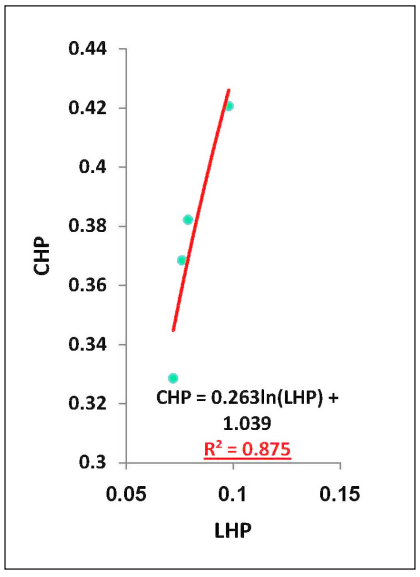

Figure 6. Regression equation between (CHP) and (LHP).

vary between 0.32 and 0.42 μW/m^3, and are in agreements, particularly with the range (HP) values of the basalt of German basin (Ben Norden and Forster, 2006, Abady *et al.*, 2004; Hasterok *et al.*, 2018; and Asfahani, 2019a.

A regression analysis is done between the corrected radioactive heat production values of the rock samples (CHP), and those values computed (LHP) in the Kodana borehole by Bücker and Rybach technique, 1996 at the same depths of rock samples locations, Table 1. The regression line between (CHP) and LHP is shown in Figure 6.

The regression equation between (CHP) and (LHP) has the following form:

$$CHP = 0.26 * \ln (LHP) + 1.039 \quad (5)$$

with a regression coefficient $R^2 = 0.875$.

Since R^2 is high and acceptable, equation (5) is applied therefore to correct and calibrate the measured radioactive heat production (LHP) along Kodana borehole as shown in Figure 7.

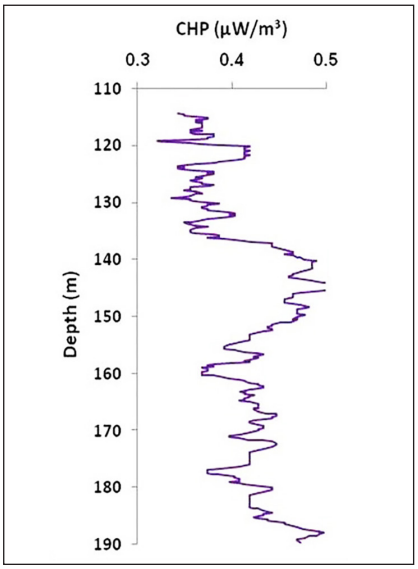

Figure 7. corrected and calibrated (CHP) along Kodana borehole.

Table 2. Statistical characteristics of Ra (API) and CHP (μW/m^3) in the Kodana borehole

	Ra (API)	HP (μW/m^3)
No of measured points	377	377
Min	4.93	0.32
Max	9.31	0.51
Average	6.83	0.42
Standard deviation	0.94	0.041

The corrected (CHP) along the Kodana borehole varies between a minimum of 0.32 and 0.51 μW/m^3 with an average of 0.42μW/m^3 as shown in Table 2. The frequency distributions of both (Ra) and (CHP) shown in Figure 8 (a and b) reflect normal distributions.

The obtained corrected (CHP) values are in close agreement with those of the basalt of the Northeast German basin (Ben Norden and Forster, 2006), Abady *et al.*, 2004; Hasterok *et al.*, 2018, and Asfahani, 2019a.

Based on the corrected radioactive heat production log discussed above, the empirical equation (3) of Bücker and Rybach (1996) must be necessarily modified to be more suitable and applicable in continental basalt environments. The two constants of 0.0158 and 0.8 reported in the equation (3) must be therefore changed and modified to be as 0.037 and -4.35 respectively.

The new established equation has accordingly the following form:

$$HP\ (\mu W/m^3) = 0.037\ (Ra\ (API) - (-4.35)) \quad (6)$$

Figure 9 confirms the excellent agreement between the corrected radioactive heat production results (CHP) discussed above and those (CHP-1) obtained by applying the new proposed modified equation (6). The R^2 regression coefficient

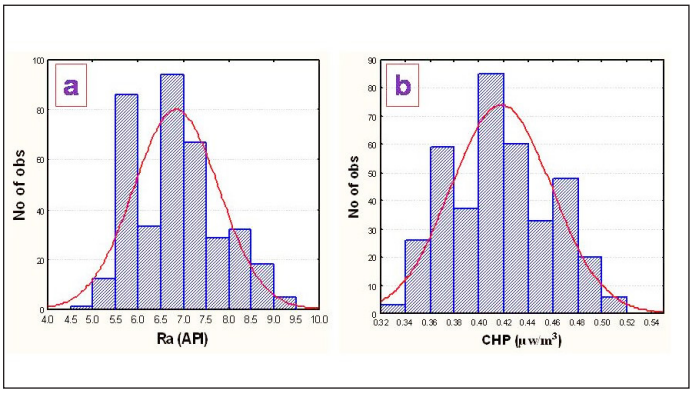

Figure 8. Frequency distribution of a): Radioactivity (Ra) and b): Corrected radioactive heat production (CHP).

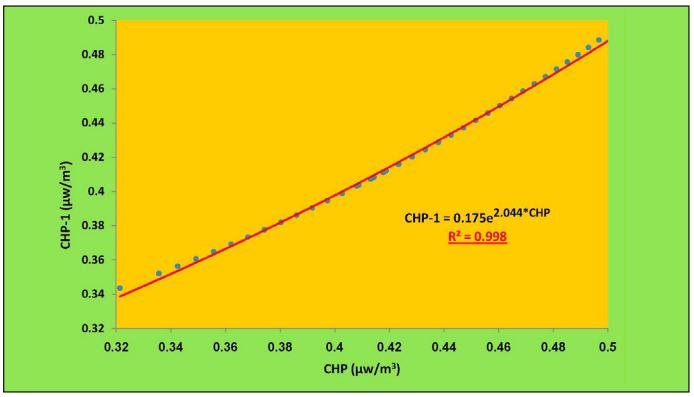

Figure 9. Correlation curve between (CHP) and (CHP-1).

between (CHP) and (CHP-1) is 0.998. The absolute and relative errors between (CHP) and (CHP-1) do not exceed 0.0221 and 6.87% respectively.

With the values of both the (CHP) log and the density log being known at the Kodana borehole, one can easily get the variations of the parameter (Y) included in equation (2) along the Kodana borehole as shown in Figure 10.

The "Y" parameter includes the sum of radioelements (eU, eTh, and K%) that contribute to the heat production. It seems that the vertical resolution of the (Y) is better than that of the Ra log shown in Figure 4. The variations of (Y) log give insights on the basalt deposition and its geological conditions, and show also a successive of poor and rich radioactive contents (eU, eTh, and K%).

Figure 11 shows a positive correlation statistical relationship between (Y) and (CHP) with $R^2 = 0.384$. The low R^2 is due to two factors. The first is that uranium is the main radioactive element

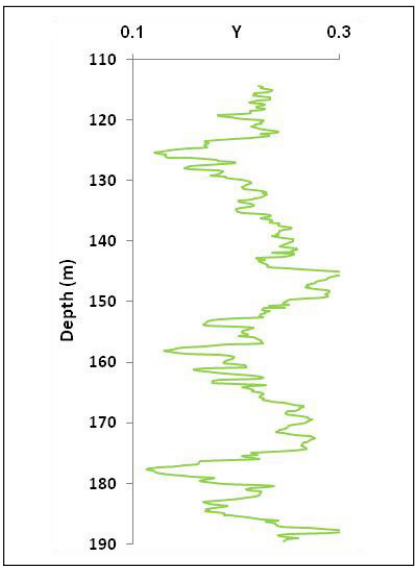

Figure 10. Variation of "Y" along Kodana borehole.

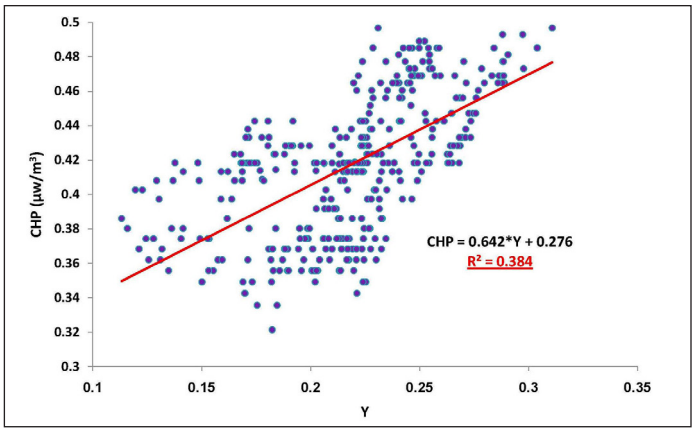

Figure 11. Correlation relationship between (Y) and (CHP).

in producing heat, compared with eTh and K%, which have just a limited role in such a radioactive heat production. The second is the density parameter that relies (Y) and (CHP), and its variations along the Kodana borehole.

Fractal concentration-number (C-N) model and log-log plots are applied to characterize the variations of both Ra (API) and CHP (µW/m^3) parameters related to 377 points measured along the Kodana borehole in the study region.

The log-log graphs show different break points (C1, C2, and C3) that can be used as thresholds and lithological boundaries in the study Kodana borehole. Different lithological populations of (Ra) and (CHP) are consequently differentiated according to those determined break-points. The three C1, C2, and C3 threshold break points are shown on the C-N log-log plot of (Ra) at the locations of 0.823, 0.907, and 0.933 respectively as presented in Figure 12. Those three locations on the log (Ra) indicate a natural gamma ray intensity of 6.65, 8.07, and 8.57 API respectively. The three break points correspond to four straight line segments with different slopes −D, corresponding to different population ranges on the log–log plots of N(≥µ) versus µ (Ra).

The four Ra ranges are as follows: The first range is less than 6.65 API, the second range is between 6.65 and 8.07 API, the third range is between 8.07 and 8.57 API, and the fourth range is bigger than 8.57 API.

The three C1, C2, and C3 threshold break points are shown on the C-N log-log plot of CHP at the locations of -0.451, -0.387, and -0.355 respectively as presented in Figure 13. Those three locations on the log (CHP) indicate a corrected radioactive heat production CHP of 0.354, 0.41, and 0.44 µW/m^3 respectively. The three break points correspond to four straight line segments with different slopes −D,

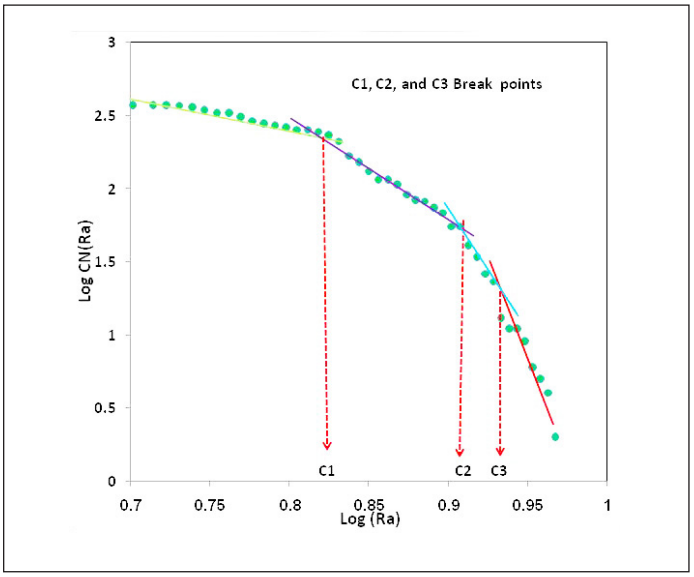

Figure 12. Log-log plot for the Ra (API) parameter in the Kodana borehole.

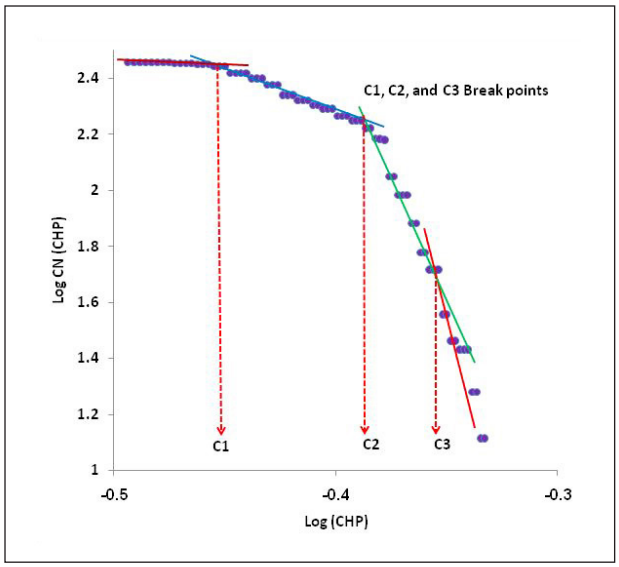

Figure 13. Log-log plot for the computed CHP parameter in the Kodana borehole.

corresponding to different population ranges on the log–log plots of N(≥μ) versus μ (CHP).

The four (CHP) ranges are as follows: The first range is less than 0.354 μW/m^3, the second range is between 0.354 and 0.41 μW/m^3, the third range is between 0.41 and 0.44 μW/m^3, and the fourth range is bigger than 0.44 μW/m^3.

The lithological rock types corresponding to the four ranges of (Ra) and (HP) determined by the fractal technique discussed above are shown in Table 3.

The new corrected radioactive heat production data gathered through benefiting from the available natural gamma ray logging records are important for the geothermal research in the near future in the study region.

5. Verification and validation of the new proposed equation

The new proposed equation 6 for estimating the heat production in basaltic environments is verified and validated through its additional application in other three drilled wells (Jaba, Jabeit, and Al-Asbah) in the study region. The locations of those three wells are shown in Figure 2. The natural gamma rays logs (Ra) in cps for those wells cover only the saturated Neogene basalt aquifer in the study region as shown in Figure 3, and are converted into API unit (Figure 14) as done for Kodana well.

The heat production logs (HP) are computed for those wells, according to the proposed equation 6 as shown in Figure 15.

The main statistical results obtained for Ra and HP for those three wells are presented in Table 4.

Comparable HP results with those discussed above for Kodana well are obtained by applying equation 6.

The range of the heat production obtained in the four studied wells (0.165-0.5 μW/m^3) by using the new proposed equation is in agreement with the one reported (0.1- 0.7μW/m^3) by Ben Norden and Forster, 2006 for the the basaltoides of Northeast of German basin. This attests to the

validity of the new proposed equation 6 for characterizing the heat production (HP) of the continental basalt, by using the natural gamma ray well logging technique.

Table 3. Rock types related to the Ra (API) and CHP (μW/m^3) in the study area.

Ra (API)	**HP (μW/m^3)**	**Rock Type**
< 6.65	< 0.354	Hard massive basalt
6.65-8.07	0.354-0.41	Hard basalt
8.07-8.57	0.41-0.44	Pyroclastic basalt
> 8.57	> 0.44	Alteration basalt products, clay

Table 4. Statistical of Ra and HP in the Jaba, Jabeit, and Al-Asbah wells.

	(Jaba well) **Ra (API)**	(Jaba well) **HP** (μW/m^3)	(Jabeit well) **Ra (API)**	(Jabeit well) **HP** (μW/m^3)	(Al-Asbah well) **Ra (API)**	(Al-Asbah well) **HP** (μW/m^3)
Min	0.123	0.165	1.13	0.20	0.94	0.195
Max	0.31	0.172	2.88	0.27	3.78	0.30
Average	0.229	0.169	1.87	0.23	1.91	0.23

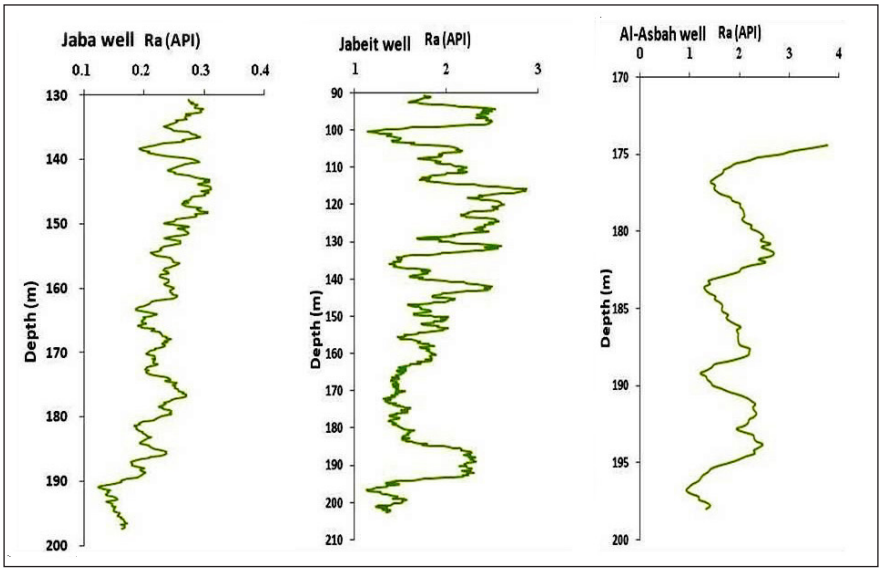

Figure 14. Natural gamma ray logs (Ra) in Jaba, Jabeit, and Al-Asbah wells.

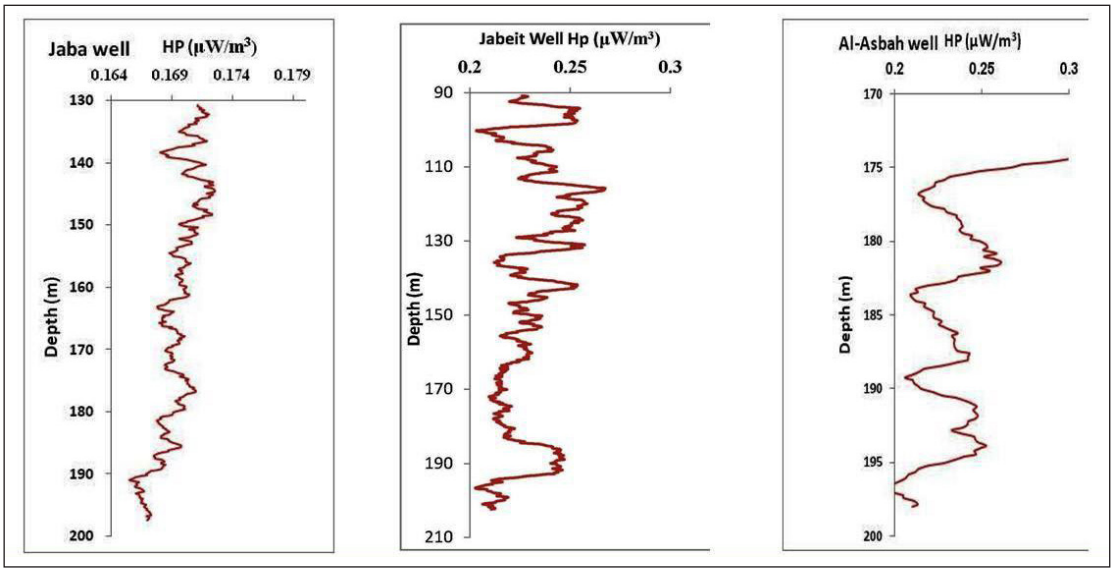

Figure 15. Heat production logs (HP) computed according to equation.6 in Jaba, Jabeit, and Al-Asbah wells.

6. Conclusion

The direct method proposed by Bücker and Rybach (1996) is applied to convert the natural gamma ray logs (Ra) to radioactive heat production logs (LHP). The application of this technique on the (Ra) of Kodana borehole gives underestimated (LHP) values. This underestimation is due to the considerable difference between the radioactive content of the continental basalt (eU, eTh, and K%) related to the study region and that of the basaltic rock samples used for the calibration of the empirical relationship of Bücker and Rybach. The constants of equation (3) of Bücker and Rybach, 1996 are accordingly modified, where a new relationship is established and proposed between natural radioactivity (Ra) log values and radioactive heat production (HP). The new proposed equation is more suitable as demonstrated and proven in this present case study to be applied for characterizing the radioactive heat production in continental basaltic environments. This new equation is also verified and validated on other additional three drilled wells in the study region, where the different HP results obtained through those wells demonstrate a clear consistency between them.

The radioactive heat production values (CHP) obtained through the basalt rock samples are accurately determined, and agree with those obtained in the literature worldwide. The regression analysis done between (LHP) and (CHP) enables us to establish the corrected radioactive heat production (CHP) log along the Kodana borehole, where the high (CHP) values are related to the basalt alteration product and clay. The use of the concentration-number (C-N) fractal model with the log-log graphs allows to distinguish differ-

ent radioactivity and corrected radioactive heat production ranges related to different kinds of basalt. The new (CHP) log data of the Kodana region are required for analyzing and characterizing the temperature distribution modeling and the thermal evolution of the study region.

7. Acknowledgements

The author would like to thank Dr. I. Othman, General Director of Syrian Atomic Energy Commission, for his permission to publish this paper. The two anonymous reviewers are cordially thanked for their professional remarks, suggestions, and critics that considerably improved the final version of this paper. Thanks are due to, the Associated Editor and the Editor-in-Chief of Geofísica Internacional for their assistance during the different process of this paper. My thanks is also to Dr. Mtra. Andrea Rostan, the technical editor of the Geofísica Internacional for the collaboration during the different stages of this paper.

8. Declaration of competing interest

The author declares that he has no known competing financial interests or personal relationships that could have appeared to influence the work reported in this paper.

9. References

Abbady, G.E., El-Arabi, A.M., Abbady, A (2004): Radioactive heat production Rate From Radioactive Elements in Igneous and Metamorphic Rocks in Eastern Desert, Egypt. VII Radiation Physics & Protection Conference, 27-30 November 2004, Ismailia-Egypt.

Afzal, P., Khakzad, A., Moarefvand, P., Rashidnejad Omran, N., Esfandiari, B., FadakarAlghalandis, Y., (2010): Geochemical anomaly separation by multifractal modeling in Kahang (Gor Gor) porphyry system. Central Iran. J Geochem Explor 104:34–46.

AQCS, (1995): Intercomparison runs reference materials. International Atomic Energy Agency, P.44.

Asfahani, J., (2011): Basalt characterization by means of nuclear and electrical well logging techniques. Case study from Southern Syria. Appl. Radiat. Isot. 69, 641–647.

Asfahani, J. (2018): Estimating and mapping radioactive heat production by using aerial spectrometric gamma and fractal modeling techniques in Syrian desert (Area-1), Syria. Appl. Radiat. Isot. 142, 194–202. **https://doi.org/10.1016/j.apradiso.2018.09.004**

Asfahani, J. (2019a): Radioactive heat production of Syrian Territory. Appl. Radiat. Isot 149, 142–151.

Asfahani, J. (2019b): heat production estimation by using natural gamma ray well logging technique in phosphatic Khneifis deposit in Syria. Appl. Radiat. Isot. 145, 209–216. **https://doi.org/10.1016/j.apradiso.2018.11.017**

Asfahani, J., Samuding, K., Mostapa, R., Othman, O (2021): Radioactivity and heat production characterization by natural gamma ray well logging and multi-fractal techniques in banting district, Malaysia. Applied Radiation and Isotopes 167.

Asfahani, J. (2022): Radioactive heat production characterization of Ar-Rassafeh BadyiehArea (Area-2), Syria using aerial gamma ray spectrometric and fractal modeling techniques. Geofísica Internacional 61-1, 20-39. **https://doi.org/10.22201/igeof.00167169p.2022.61.1.2120**

Asfahani, J. (2022a): Vertical electrical sounding technique as an efficient and rapid tool for groundwater investigation in a basaltic environment at Kodana station for the Shami goats. case study from Southern Syria. Paper submitted to Geofisica Internacional.

Black well, D. D., and J. L. Steele, (1989): Thermal conductivity of sedimentary rocks: Measurement and significance, in N. D. Naeser and T. H. McCulloh, eds., Thermal history of sedimentary basins: New York, Springer-Verlag, p. 13– 36.

Ben Norden and Andrea Forster, (2006): Thermal conductivity and radiogenic heat production of sedimentary and magmatic rocks in the Northeast German Basin. American Association of Petroleum Geologists, AAPG Bulletin, v. 90, no. 6, pp. 939–962.

Birch, F., (1954): Heat from radioactivity. In Nuclear Geology; Wiley: New York, NY, USA, pp. 148–174. BOSCH, J.H., 1988.

Bücker, C., Rybach, L., (1996): A simple method to determine heat production from gamma-ray logs. Mar. Pet. Geol. 13, 373e375.

Deming, D., J. A. Nunn, S. Jones, and D. S. Chapman, (1990): Some problems in thermal history studies, in V. N. Nuccio and C. E. Barker, eds., Applications of thermal maturity studies to energy exploration: Rocky Mountain Section, SEPM, p. 61–80.

Fernandez, M., Marzan, I., Correia, A., Ramalho, E., (1998): Heat flow, heat production and lithosphere thermal regime in the Iberian Peninsula. Tectonophysics 291, 29-53.

Hasterok, D., Gard, M., Webb, J. (2018): On the radiogentic heat production of metamorphic, igneous, and sedimentary rocks. Geosciences Frontieres Vol 9, Issue 6. PP. 1777-1794.

Lashin, A. (2005): Reservoir parameter estimation using well logging data and production history of the Kaldarholt geothermal field, S-Iceland geothermal training programme, Orkustofnun, Grensásvegur 9, Number 12 IS-108 Reykjavík, Iceland.

Mohamadi, A., Khakzad, A., Rashidnejad Omran, N., Mahvi, M.R., Moarefvand, p., Afzal, P., (2013): Application of number–size (N–S) fractal model for separation of mineralized zones in Dareh-Ashki gold deposit, Muteh Complex, Central Iran. Arab J Geosci. doi:10.1007/s12517-012-0662-y.

Nuclear Analysis Software, (1991): GANAAS, IAEA, Vienna, IAEA/CMS/3.

Richardson, K.A., Killeen, P.G., (1980): Regional radiogenic heat production mapping by airborne gamma-ray spectrometry. In: Current Research, Part B, Geological Survey of Canada, pp. 227e232. Paper 80e1B.

Robertson geologging Ltd., (1993): Deganway, Conway, Gnedd. LL319 PX.

Rybach, L., (1976): Radioactive heat production in rocks and its relation to other petrophysical parameters. Pure Appl. Geophys. 114, 309-318.

Salem, A., El Sirafy, A., Aref, A., Ismail, A., (2005): Mapping radioactive heat production from airborne spectral gamma-ray data of Gabal Duwi area, Egypt. In: Proceedings World Geothermal Congress, Antalya, Turkey, pp. 24-29.

Thompson, P.H., Judge, A.S., Charbonneau, B.W., Carson, J.M., Thomas, M.D., (1996): Thermal regimes and diamond stability in the Archean slave province, Northwestern Canadian Shield, District of Mackenzie, Northwest Territories. In: Current Research, 96e1E, Geological Survey of Canada, pp. 135e146.

Wang, Q. F., Deng, J., Liu, H., Wang, Y., Sun, X., Wan, L., (2011): Fractal models for estimating local reserves with different mineralization qualities and spatial variations. J. Geochem. Explor. 108, 196–208. doi: 10.1016/j.gexplo.2011.02.008.

Zuo, R., (2011): Decomposing of mixed pattern of arsenic using fractal model in Gangdese belt, Tibet, China. Appl Geochem 26: S271–S273 Davis JC (2002) Statistics and data analysis in geology, 3rd ed. John Wiley & Sons Inc, New York.